The Production and Delivery of Green Hydrogen and Recovered Waste Heat

A Techno-Economic Analysis of a Multi-MW Alkaline and PEM Electrolysis Plant

Master Thesis
Stijn de Haan

Delft University of Technology

TU Delft

The Production and Delivery of Green Hydrogen and Recovered Waste Heat

A Techno-Economic Analysis of a Multi-MW Alkaline and PEM Electrolysis Plant

by

Stijn de Haan

to obtain the degree of Master of Science
at the Delft University of Technology,
to be defended publicly on Thursday August 31, 2023 at 12:00 PM.

Graduation Committee:
Chairman and 1st supervisor: Prof. R.A. (Remco) Verzijlbergh; TPM, TU Delft
2nd supervisor: Prof. M. (Milos) Cvetkovic; EWI, TU Delft
External supervisor: S. (Sander) Aukema; Uniper

Abstract

In this thesis, both a 10 MW Alkaline Electrolyser (AE) and a 10 MW Proton-Exchange Membrane (PEM) electrolyser system are evaluated through a comprehensive techno-economic feasibility study, spanning a 25-year operational lifespan. The systems are designed to serve a dual function, producing green hydrogen at 350 bar for utilisation at a hydrogen refuelling station for heavy-duty trucks, as well as recovering waste heat via a tie-in on the cooling system of the electrolyser to directly supply a medium-temperature district heating network at 70 °C. The latter is achieved by connecting the tie-in to a heat exchanger, resulting in a cost-effective heat recovery without the implementation of an expensive heat pump. Both electrolysis systems are operated at 80 °C and powered by offshore wind power, delivered to the electrolyser system through a virtual PPA.

ERA5 data on the wind speed was employed, which was converted into power data via the wind farm power curve. The wind farm power curve was produced by coupling wind farm power production data to the ERA5 wind speed. This method proved to be effective in simulating the power production of a wind farm, as it included the wind farm wake effects and the global-blockage effect.

The performance of the AE system was simulated through a semi-empirical model for both the polarization and Faraday efficiency curve, while the performance of the PEM electrolyser system was simulated by an empirical approach for the polarization curve and a semi-empirical model for the Faraday efficiency curve. A degradation efficiency method is proposed, which employs a constant degradation factor to describe the decreasing performance over the lifetime of the stack. The degradation efficiency effectively illustrated the heat-producing degradation in electrolyser cells.

The techno-economic aspect of the research involved a detailed analysis of the Levelised Costs of Hydrogen and Heat ($LCoH_2$ and $LCoH_{eat}$). The $LCoH_2$ of green hydrogen from the AE system was 6.08 €/kg, while the $LCoH_{eat}$ of the recovered waste heat was 1.57 €/MWh. For the PEM electrolyser system, the $LCoH_2$ was determined to be 5.59 €/kg, while the associated $LCoH_{eat}$ for the recovered waste heat was 1.55 €/MWh. The profits of selling the recovered waste can be utilised to decrease the $LCoH_2$. When a recovered waste heat-selling price of 50 €/MWh was assumed, the $LCoH_2$ of the AE and PEM electrolyser system decreased by 0.64 €/kg and 0.44 €/kg, respectively.

The sensitivity analysis on the $LCoH_2$ indicated that the PPA price was the most influential factor on the $LCoH_2$, followed by the Capital Expenditures (CAPEX) of the electrolyser system, and the start-of-life stack efficiency. When assessing the $LCoH_{eat}$, the sensitivity analysis revealed that the most impacting parameters on the $LCoH_{eat}$ were the capacity of the installed electrolysis plant, the discount rate and the CAPEX of the heat exchanger.

Nomenclature

Abbreviations

Abbreviation	Definition
AE	Alkaline Electrolyser
atm	Atmospheric pressure
C	Celsius
CAPEX	Capital Expenditures
CHP	Combined Heat and Power
CCS	Carbon Capture and Storage
CO_2	Carbon Dioxide
DECEX	Depreciation Expenditures
ETS	Emissions Trading System
EU	European Union
EV	Electric Vehicle
g	Gram
GHG	Greenhouse Gas
GW	Gigawatt
h	Hour
H_2	Hydrogen
H_2O	Water
HE	Heat Exchanger
HHV	Higher Heating Value
IPCC	Intergovernmental Panel on Climate Change
J	Joule
K	Kelvin
kg	Kilogram
LCoE	Levelised Cost of Energy
$LCoH_2$	Levelised Cost of Hydrogen
$LCoH_{eat}$	Levelised Cost of Heat
LHV	Lower Heating Value
LOWESS	Locally-Weighted Scatterplot Smoothing
MJ	Mega Joule
MW	Megawatt
MWh	Megawatt-Hour
O_2	Oxygen
OPEX	Operational Expenditures
PEM	Proton-Exchange Membrane
PPA	Power Purchase Agreement
RFNBO	Renewable Fuels of Non-Biological Origin
SOEC	Solid Oxide Electrolyser Cell
TSO	Transmission System Operator
yr	Year
W	Watt

Contents

1

Introduction

1.1. Context

According to the recent "Climate Change 2023" released by the Intergovernmental Panel on Climate Change (IPCC), climate change is happening faster than anticipated, primarily because of human activities [IPCC, 2023]. The report points to the pressing effects of climate change, such as increased temperatures, higher sea levels, health problems, and a decline in water and food availability. To counter the effects of climate change, the IPCC advises shifting away from fossil fuels to low-carbon or renewable energy alternatives. Transitioning from fossil fuels to renewable energy sources is pivotal in managing a sustainable trajectory towards a net-zero future. Currently, close to 80% of the global energy demand is met through the use of fossil fuels, but that percentage is declining exponentially [Younas et al., 2022]. Both the COVID-19 pandemic and the invasion of Russia in Ukraine have triggered an additional increase in the share of renewable energy supplying the global energy demand [IEA, 2022b]. Disruptions in the supply of fossil fuels highlighted the benefits of domestic renewable energy production. Additionally, rising fossil fuel prices have improved the competitiveness of renewable energy generation against fossil fuels globally.

However, the intermittent character of wind and solar power results in imbalances between the production and consumption of electricity. Energy storage will act as a vital component in future low-carbon energy systems, aligning the intermittent renewable energy sources with the electricity demand [Sanchez et al., 2018]. Both daily and seasonal variances in intermittent renewable energy output necessitate appropriate energy storage mechanisms. Storing renewable energy through chemical bonds, especially in the form of hydrogen, is considered favourable for long-term storage due to the significant energy density, elemental abundance, and capability for transportation by pipelines [Schmidt et al., 2017]. Since hydrogen does not exist freely in nature and has to be produced, it acts as an energy carrier rather than a renewable energy source.

While the role of hydrogen in energy storage is evident, the applications of hydrogen extend much further in a net-zero future. Historically, hydrogen plays an important role in fuel refining and fertilizer production. However, hydrogen could also replace fossil-based feedstocks in the transport, iron, cement, and steel industries, drastically reducing the Greenhouse Gas (GHG) emissions in these sectors [Wilberforce et al., 2023]. Hydrogen can be derived from a variety of pathways, technologies, and an extensive array of feedstocks that encompass both renewable and non-renewable resources. The use of hydrogen will only reduce GHG emissions in a certain sector if hydrogen is produced using renewable sources. As it stands, 95% of the hydrogen used globally is produced using Steam Methane Reforming (SMR) of natural gas and coal [Calado and Castro, 2021]. This process emits significant amounts of carbon dioxide, which negates the sustainability aspect.

Water electrolysis is commonly acknowledged as an efficient technique for producing green hydrogen, contributing to 4% of the global hydrogen production [IRENA, 2022]. In water electrolysers, renewable electricity is utilized to drive the splitting of water into hydrogen and oxygen, thus converting electrical energy into the chemical energy of hydrogen. At present, the Alkaline Electrolyser (AE) and the Proton-Exchange Membrane (PEM) electrolyser stand out as the two primary electrolysis technologies, both being mature and commercially available. Both the Dutch government and the European Commission recognise the importance of green hydrogen in a low-carbon infrastructure. The European Commission adopted the EU Hydrogen Strategy in 2020, which aims for 40 GW of installed electrolysis capacity in the EU by 2030 and 40 GW of installed electrolyser capacity outside of the EU, while the hydrogen is imported into the EU [European Commission, 2020]. The ambitious Dutch

Hydrogen Roadmap, launched in November 2022, aims for 6 to 8 GW of electrolysis capacity in the Netherlands by 2030 [NWP, 2022]. In recent years, multiple initiatives for 100 MW or larger green hydrogen projects have been announced by Shell, BP and Air Liquide in the Netherlands [ISPT, 2022].

1.2. Motivation

The primary hurdle impeding the commercialisation and market adoption of water electrolysis is the relatively high cost of green hydrogen compared to grey hydrogen produced by SMR of fossil fuels [Wilberforce et al., 2023]. In 2021, the price of grey hydrogen was approximately 1.50 €/kg and the price of green hydrogen ranged between 3 and 11 €/kg [Kovac et al., 2021; LAZARD, 2021; IRENA, 2022]. The cost related to producing hydrogen is generally expressed by the Levelised Cost of Hydrogen ($LCoH_2$), which reflects the average costs for producing a kilogram of hydrogen and indicates the economic viability of a hydrogen-producing installation. The ranges for the $LCoH_2$ as indicated by the IEA [2020] are showcased in Figure 1.1. In the absence of hydrogen policies or subsidies on green hydrogen, a hydrogen consumer will select hydrogen from the most economical production method. Therefore, the costs related to the production of green hydrogen should be reduced.

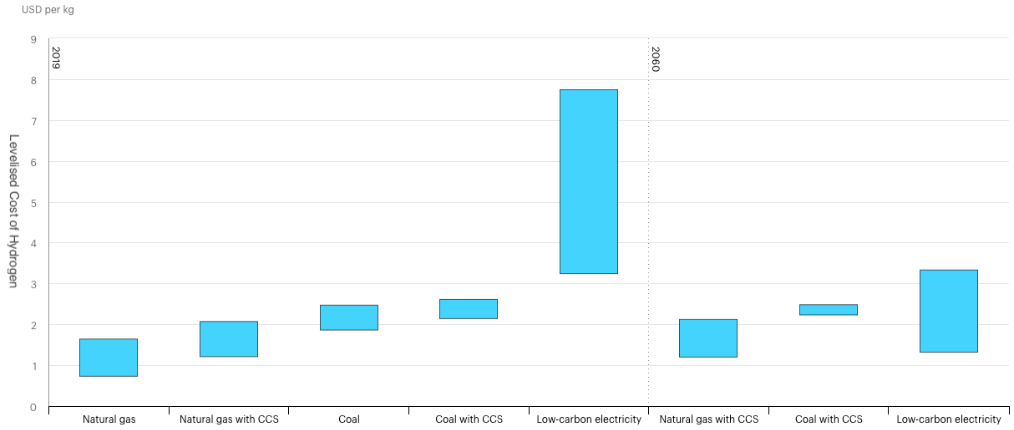

Figure 1.1: The range for the $LCoH_2$ of different hydrogen production feedstocks expressed in \$/kg. Carbon Capture and Storage (CCS) is included for fossil fuels [IEA, 2020].

Modelling an electrolyser is a useful tool for predicting the behaviour of an electrolyser in specific circumstances. Accurately modelling an electrolyser is especially vital when the electrolyser is coupled directly to a renewable source of electricity [Garcia-Valverde et al., 2012]. Renewable energy sources have an intermittent supply of electricity which influences the power delivered to the electrolyser. Modelling electrolysers not only allows for designing an optimal electrolyser system, but also allows for simulating the production of hydrogen. The production of hydrogen can be used to calculate the $LCoH_2$ of an electrolyser system and thus determine the economic feasibility of the electrolysis system. Additionally, when changing any variable in the electrolyser model, its influence on the $LCoH_2$ can be checked.

Both AE and PEM electrolysers typically operate at an efficiency range of 70 to 80%, while the remaining energy is lost as heat in the process [Gambou et al., 2022; IRENA, 2022]. A constant operational temperature of the electrolyser is required for optimal hydrogen production. Therefore, the accumulation of heat necessitates the cooling of electrolysers to maintain a constant operational temperature. This waste heat is generally dissipated into the surroundings. However, with the emergence of larger-scale electrolysers with multi-MW or GW capacities, the amount of generated waste heat becomes significant. In such cases, it could be practical to consider recovering the waste heat of an electrolyser. While a significant focus has been placed on improving the efficiencies of electrolysis in research, the investigation into the utilization of residual heat produced by the process has been understudied. This conclusion was also drawn by Le Coultre [2022] and van der Roest et al. [2023]. In the study by van der Roest et al. [2023], the costs for recovering the waste heat of a PEM electrolyser were calculated. However, almost all research focuses on increasing the temperature of the waste heat by a heat pump or generating electricity by an organic Rankine cycle [Lummen et al., 2019; Villarreal Vives et al., 2023; Hermans, 2021]. However, both a heat pump and an organic Rankine cycle are expensive, decreasing the economic viability of recovering the waste heat. A more straightforward approach might be directly using the recovered waste heat in applications that require heat at a low temperature. The effective recovery and use of waste heat could diminish carbon dioxide emissions, particularly when the heat derived from the electrolyser replaces heat that is produced from natural gas or other fossil-based sources. To assess the costs related to the recovery of waste heat, the Levelised Cost of Heat ($LCoH_{eat}$) can be determined in the same manner as the $LCoH_2$.

1.3. Objective

This thesis aims to gain insight into the parameters influencing the Levelised Cost of Hydrogen ($LCoH_2$) and Levelised Cost of Heat ($LCoH_{eat}$) of both an AE and PEM electrolysis plant, which is powered by offshore wind energy. To this end, a general AE and PEM electrolysis system layout is designed including the recovery of waste heat directly at the temperature at which it is extracted from the electrolyser. When calculating the $LCoH_2$ and $LCoH_{eat}$, the electrolyser should be simulated over the entire lifespan of the system. It is important to employ an electrolyser model that can handle the effects of long-term operation and a fluctuating load from wind power. As the electrolyser system is powered by a wind farm, producing intermittent renewable electricity, power production data of a wind farm is required as input to simulate an electrolyser over its entire lifespan. This type of data is not available over such a period, therefore an approach for obtaining the production of a wind farm is studied in this thesis.

The models for the AE and PEM electrolyser systems could then be employed to simulate a case study. The case study covers a conceptual electrolysis plant in the region of Zuidplas in the Netherlands. For the case study, it is assumed that the electrolysis plant will become operational in 2027. The electrolyser supplies green hydrogen to a refuelling station by a pipeline and delivers the recovered waste heat directly to a district heating network. The application of the electrolyser models to this case will involve numerous assumptions, which will be detailed in subsequent chapters.

The main research question of this thesis is stated as follows.

- To what extent do the levelised cost of hydrogen and the levelised cost of heat for a multi-MW heat-recovering green AE and PEM electrolysis plant depend on the design parameters and boundary conditions of the electrolyser system?

The secondary questions supporting the main research questions are:

1. What is the optimal electrolysis system layout to directly recover waste heat from an electrolyser?
2. How can both a green AE and PEM electrolyser system be most effectively modelled for long-term operation and a fluctuating load?
3. How can the power production of a wind farm be most effectively modelled?
4. What are the levelised cost of hydrogen and heat for a potential electrolyser plant in Zuidplas?

1.4. Uniper

This thesis was carried out at the TU Delft in collaboration with Uniper Benelux. Uniper is an energy company that was split off from E.ON in 2016, inheriting E.ON's fossil fuel-based assets. Next to these assets, Uniper also participates in the energy trading sector. The company oversees Combined Heat and Power (CHP) systems as well as natural gas boilers, which deliver power to the grid and supply heat to district heating including Rotterdam, Den Haag, and Leiden.

Uniper supplied information for the case study in Zuidplas studied in this thesis. Uniper is interested in an electrolyser that recovers waste heat in this area since it already supplies heat to the existing heating network and also governs the heat network.

1.5. Methodology

First, the background theory of all relevant sectors is elaborated in Chapter 2, followed by the model for the AE and PEM electrolyser system in Chapter 3. In Chapter 4, The location analysis of the case study is discussed. The system design of the wind power system, the electrolyser system and the levelised costs system are discussed in Chapter 5. In this chapter, the design and boundary choices are motivated by examples in the literature. Chapter 6, the system design is applied to the model and case study and intermediate results are showcased, followed by the results and sensitivity analysis of the electrolyser systems in Chapter 7. Finally, the models and results of this thesis are discussed in Chapter 8 and a conclusion is drawn in Chapter 9.

2

Theory

This chapter describes all background theory on the physics and chemistry that is required to comprehend the implementation of a green electrolysis plant that recovers waste heat. The theory forms the basis of the next chapters on the electrolyser model and its application to the case study. To this end, the final product of hydrogen will be discussed first in Section 2.1. Next, water electrolysis and electrolysers are discussed in Section 2.2. The production of electricity from wind energy is discussed in Section 2.3. Finally, the economic theory on the Levelised Cost of Hydrogen ($LCoH_2$) and the Levelised Cost of Heat ($LCoH_{eat}$) are discussed in Section 2.4.

2.1. General Information on Hydrogen

Hydrogen (H) is a chemical element and is the first and thus lightest element in the periodic table. Hydrogen is the most abundant element in the universe, but only a tiny fraction of the earth is comprised of hydrogen. Most of the hydrogen on earth exists in molecular forms as water or other organic compounds, since hydrogen readily forms covalent bonds with non-metallic elements. For this reason, hydrogen gas hardly exists in the atmosphere and it needs to be produced by mankind through extraction from molecules that contain hydrogen [Zohuri, 2019].

Under standard conditions, hydrogen is a gas of diatomic molecules bonded together through a covalent bond having the formula H_2, called dihydrogen. In scientific literature and this thesis, the term "hydrogen" generally refers to this gaseous form of diatomic hydrogen molecules. Hydrogen is a very energy-rich molecule, under standard conditions it contains 142 MJ kg^{-1} when using the Higher Heating Value (HHV) compared for example to 44 MJ kg^{-1} for gasoline. On a volume basis, however, hydrogen gas at 1 atm and 25 °C has an energy density of 0.012 MJ L^{-1} compared to the energy density of gasoline of 32 MJ L^{-1} [Kovac et al., 2021; Zohuri, 2019]. Liquid hydrogen has a much higher volumetric energy density of 8 MJ L^{-1} than hydrogen gas, but the condensation point of hydrogen is at -253 °C [Zohuri, 2019].

There are two general possibilities to utilise the chemical energy in hydrogen: Hydrogen can either be burned or used in a fuel cell to generate electricity. When hydrogen is burned in the presence of oxygen gas (O_2) the reaction is as follows:

$$2H_2 + O_2 \rightarrow 2H_2O + \text{heat} \tag{2.1}$$

As one can see in the reaction, water is the only product of the combustion of hydrogen, accompanied by the release of heat. The heating value or heat of combustion is a measure for the amount of heat that is produced by the complete combustion of a hydrocarbon. The heat of combustion can be indicated by the Higher Heating Value (HHV) or the Lower Heating Value (LHV). HHV includes the latent heat of vaporization in the combustion products, whereas LHV does not. The HHV for the combustion of hydrogen is 285.8 kJ mol^{-1} (141.8 MJ kg^{-1}), based on forming liquid water. The LHV of the combustion of hydrogen is only 241.8 kJ mol^{-1} (120.0 MJ kg^{-1}), based on water vapour as a product, where the energy required to vaporize water is not released as heat [Harrison et al., 2010; Dell et al., 2014; Engineering ToolBox, 2003]. In general, the HHV is used when referring to the electrolysis of water [Lettenmeier, 2021]. This convention is also followed in this thesis.

2.2. Electrolysis

Electrolysis is a technique that uses direct electric current to drive a non-spontaneous reaction to produce hydrogen and oxygen by splitting pure water. The technique has been around for many decades, but cheaper alternatives of hydrogen production, like Steam Methane Reforming (SMR) using natural gas, have been the preferred choice for large-scale hydrogen production [Grigoriev et al., 2020; Mori et al., 2013]. This section will showcase a deep dive in all important facades of hydrogen production by electrolysers.

In Section 2.2.1, the thermochemistry and electrochemistry governing the splitting of water into hydrogen and oxygen are discussed. Alkaline Electrolysers (AE) and Proton Exchange Membrane (PEM) electrolysers are the commercially available ones and Solid Oxide Electrolyser Cell (SOEC) is under demonstration at the time of this thesis. The different electrolysis techniques will be discussed in detail in Section 2.2.2. The components of a standard AE and PEM electrolyser system are detailed in Section 2.2.3. In Section 2.2.4, a system for the recovery of waste heat is proposed and previous works on waste heat of electrolysers are explored. Section 2.2.5 delves into the efficiencies related to an electrolyser cell and an electrolyser system. These efficiencies are essential in determining the produced hydrogen and recovered waste heat. Lastly, the regulatory requirements for green hydrogen are described in Section 2.2.6.

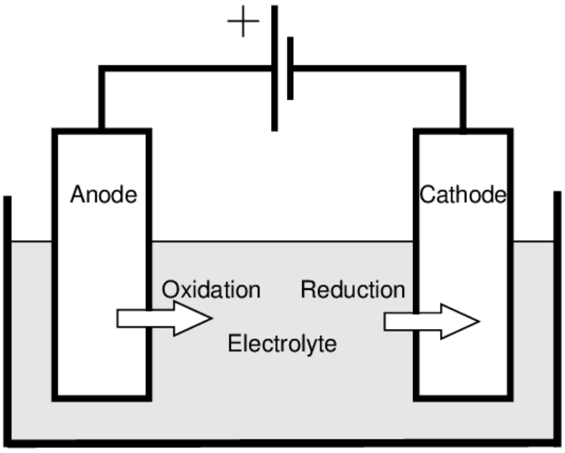

Figure 2.1: Schematic representation of a basic electrolytic cell. The oxidation reaction occurs at the positive anode, while the reduction reaction takes place at the negative cathode.

2.2.1. Thermochemistry and Electrochemistry

An electrolyser, schematically depicted in Figure 2.1, is an electrolytic cell made of two electrodes (a positive anode and a negative cathode) separated by an ion-conducting electrolyte. In the electrolyser, a redox reaction is facilitated which leads to the production the hydrogen. A barrier like a membrane is optional to keep different products from diffusing to the opposite electrode. To initiate the non-spontaneous chemical reaction, an external electrical energy source is connected to the electrodes. The external energy facilitates the required energy input to drive the overall redox reaction by

$$2\mathrm{H_2O} \rightarrow 2\mathrm{H_2} + \mathrm{O_2} \tag{2.2}$$

where H_2 is produced at the cathode and O_2 is produced at the anode. During the reaction, charge equilibrium is maintained through ion transport through the electrolyte. There are multiple ways to achieve this reaction and the selection of materials and operating conditions determine the half-reactions of the electrolyser. The total energy required to drive the reaction in Equation 2.2 is given by the change in enthalpy ΔH by

$$\Delta H = \Delta G + T\Delta S \tag{2.3}$$

where ΔG represents the change in Gibbs free energy, which is the minimal amount of electrical energy needed in this case. The difference between ΔH and ΔG is the entropic term $T\Delta S$. The term $T\Delta S$ represents the thermal irreversibility of the reaction and is equal to heat demand for a reversible process like water electrolysis. Under standard conditions (a cell temperature T_{cell} of 25 °C and a cell pressure p_{cell} of 101.3 Pa), ΔH^0 is 285.8 kJ/mol, ΔG^0 is 237.1 kJ mol^{-1} and $T\Delta S^0$ is 48.7 kJ mol^{-1} [Khater et al., 2011].

The theoretical minimum potential to drive the water-splitting reaction is the reversible cell potential U_{rev}, which is defined from the Gibbs free energy by

$$U_{rev} = \frac{\Delta G}{zF} \tag{2.4}$$

where z is the number of moles of electrons transferred in the water splitting reaction of Equation 2.2 (for water electrolysis z = 2) and F is the Faraday constant which is 96485 C mol^{-1}. Under standard conditions, the reversible or open-circuit potential U^0_{rev} is 1.229 V [Kumar and Himabindu, 2019]. At this voltage, the reaction is endothermic and heat equal to $T\Delta S$ must be absorbed from the surrounding environment. However, when operating a practical electrolyser, heat is always supplied in the form of electricity and not by an external heat source. In that case, the minimum potential to run the reaction is equal to the thermoneutral potential U_{tn}, derived from the change in enthalpy ΔH

$$U_{tn} = \frac{\Delta H}{zF} \tag{2.5}$$

An electrolyser operating at the thermoneutral potential will neither consume nor produce heat and will thus keep the cell at a constant temperature. The thermoneutral potential of an electrolyser under standard conditions U^0_{tn} is 1.482 V [Kumar and Himabindu, 2019]. When an electrolytic cell operates at a cell potential above the thermoneutral potential U_{tn}, the water-splitting reaction becomes exothermic, requiring heat dissipation to maintain isothermal operation [Mori et al., 2013].

The thermoneutral and reversible cell potential depend on the temperature, while the reversible cell potential additionally depends on the pressure of the electrolyser cell. The effect of different cell temperatures on the thermoneutral and reversible cell potential can be seen in Figure 2.2. Below 100 °C (in the liquid state), an increasing temperature decreases the thermoneutral and reversible cell potentials. Additionally, the reversible potential increases slightly with increased cell pressure. The U_{rev} and U_{tn} at operating conditions of 80 °C and 1 bar are respectively 1.184 V and 1.473 V [Ulleberg, 2003]. The U_{rev} at 25 °C and 30 bar is 1.295 V, which is higher than the 1.229 at standard conditions [Khater et al., 2011]. The electrolyser cells operate at a specific temperature and pressure, determined by the manufacturer of the electrolyser. These operating conditions are carefully selected to ensure optimal performance and efficiency of the electrolysis process. In this way, the stack is operated within the design parameters, enabling reliable and consistent hydrogen production.

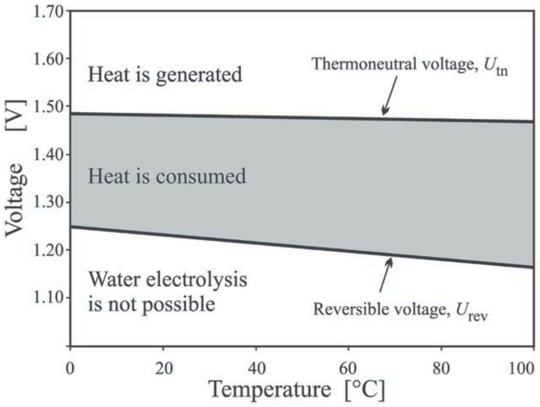

Figure 2.2: The thermoneutral U_{tn} and reversible cell potential U_{rev} of water electrolysis for different operating temperatures at a pressure of 1 bar in the regime of liquid water [Mori et al., 2013].

The Nernst equation can be derived from standard changes in Gibbs free energy and it gives the reversible potential for electrochemical reactions under non-standard conditions

$$U_{rev} = U^0_{rev} - \frac{RT_{cell}}{zF} \ln\left(\frac{[a_{H_2}]^2[a_{O_2}]}{[a_{H_2O}]^2}\right) \tag{2.6}$$

where R is the universal gas constant, which is 8.3145 J mol^{-1} K^{-1}, T_{cell} is the temperature (in K) of the electrolyser cell and a_i is the activity of the different species. For gasses in the dilute limit, the activity of the species can be assumed to be the effective partial pressure of the species. Mann et al. [2000] expressed the Nernst voltage by the following empirical equation which is a function of the operating temperature and pressure of the electrolyser.

$$U_{rev} = U^0_{rev} - 8.50 \cdot 10^{-4}(T_{cell} - 298.15) + 4.3085 \cdot 10^{-5} \cdot T_{cell}[\ln(p_{H_2}) + 0.5\ \ln(p_{O_2})] \tag{2.7}$$

where p_{H_2} and p_{O_2} are respectively the partial pressure of hydrogen at the cathode and oxygen at the anode interface. There is no term for the partial pressure of water in Equation 2.7 as it is assumed that the water product is in pure liquid form and liquids have an activity equal to one [Khater et al., 2011].

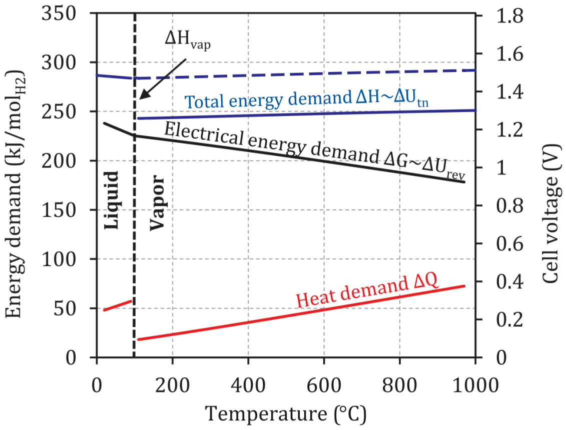

Figure 2.3: The total energy demand (ΔH), electrical energy demand (ΔG) and Heat demand (ΔQ or $T\Delta S$) for different cell temperatures of an electrolyser at 1 bar. Additionally, the change in thermoneutral (U_{tn}) and reversible potential (U_{rev}) is visualised at the right axis [Buttler and Spliethoff, 2018].

Practical electrolysers operate in a voltage regime above the thermoneutral voltage, due to energy losses by reaction kinetics and energy losses by charge transport through electrical leads and the electrolyte. These energy losses impose overpotentials on the cell voltage and therefore, water electrolysis is accompanied by the generation of heat, despite being an endothermic process [Pascuzzi et al., 2016]. The cell potential U_{cell} of an electrolyser cell can be expressed as

$$U_{cell} = U_{rev} + U_{act} + U_{ohm} + U_{con} \tag{2.8}$$

where U_{act} is the result of the activation overpotentials at the cathode and anode, U_{ohm} is the result of the ohmic overpotentials and U_{con} is the result of the condensation overpotentials. The most common representation of electrolyser performance is the polarization (or I-V) curve, which represents the relation between the current density and the cell potential including overpotentials. At zero current, the cell voltage will be equal to the reversible or open-circuit potential.

The reversible cell potential U_{rev} can be determined by the Nernst equation in Equation 2.6. The activation overpotential occurs because of the necessity to allocate potential to initiate charge transfer and account for the kinetic behaviour of the electrolyser. The third term U_{ohm} in Equation 2.8 is related to the ionic and electronic losses due to ohmic resistances in the cell. Most of the ohmic losses result from the ionic resistance in the electrolyte of the cell. The concentration or diffusion overpotential U_{con} is caused by mass transport limitations at the electrode surface and becomes a dominant factor at higher current densities. Models for the terms in the cell potential equation, as presented in Equation 2.8, will be explained in Section 2.2.2 for different electrolysis techniques.

In a lot of electrolyser models in the literature, the concentration overpotential is omitted from the cell potential equation (Equation 2.8). This is because the concentration overpotential becomes more significant at higher current densities and may not be as influential in practical modelling scenarios. Therefore, for simplicity and practical considerations, models often prioritize the inclusion of activation and ohmic overpotentials while neglecting the concentration overpotential U_{con}.

However, electrolyser cells do not have the same performance over their entire lifetime. The performance decreases gradually over time when in operation. This effect is called degradation of the electrolysis cell. The degradation results from the operating conditions and constant exposure to aggressive environments like water and oxygen, but the exact degradation mechanisms in an electrolyser depend on the electrolyser technique. The cell degradation is generally characterized as a progressive increase in the overpotential of the electrolyser cell over time. Therefore, degradation results in lower hydrogen production rates over time, or could even lead to failure of the electrolyser cell after a long time [Suermann et al., 2019].

Figure 2.4 shows an example of a polarization curve of a certain electrolyser cell used by Amores et al. [2017]. It is important to note that the polarization curve of an electrolyser varies depending on factors such as the type of electrolyser, electrode and electrolyte materials, and cell sizing. Each combination of these parameters will result in a unique polarization curve. However, the general behavior of the polarization curve remains consistent, despite the specific differences. Additionally, the fullload point, where the electrolyser operates at maximum capacity, can be chosen rather arbitrarily by electrolyser manufacturers. This operating point represents the load level that the electrolyser is designed to handle for long-term operation. Currently, there is no established industry standard method in specifying the full-load point that must be adhered to by electrolyser manufacturers [Tiktak, 2019]. However, there is a trade-off in specifying the full-load operating point. Choosing a value higher on the polarization curve results in more hydrogen production in an electrolyser cell but will result in less efficient hydrogen production. Nonetheless, opting for a higher load point allows for a smaller electrolyser size, which can positively impact the size and capital expenditures of an electrolyser plant. Finding the optimal balance between efficiency and equipment size is a key consideration in the design and operation of electrolyser systems.

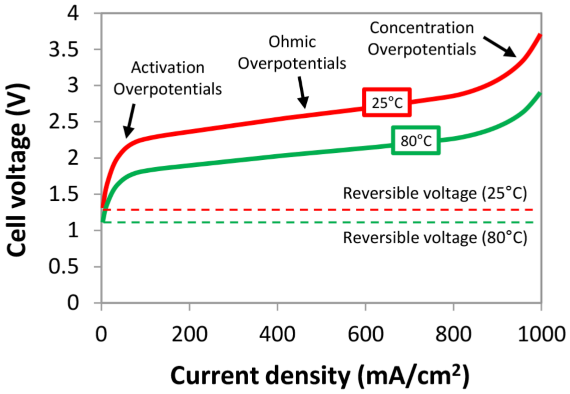

Figure 2.4: Polarization curve of a specific electrolyser cell at 25 and 80 °C, showing the characteristic shape of the polarization curve and the effects of the different overpotentials on the total cell potential [Amores et al., 2017].

The polarization curve is related to the power used in an electrolyser cell as the power of any electrical device is related to the current and voltage of the device. The power used in one electrolyser cell is

$$P_{cell} = U_{cell} I_{cell} \tag{2.9}$$

In literature, the current density i_{cell} is often used instead of the current I_{cell}. The relation between the current I_{cell} and current density i_{cell} of an electrolyser cell is given by

$$i_{cell} = \frac{I_{cell}}{A_{cell}} \tag{2.10}$$

where A_{cell} is the cross-sectional area of the electrolyser cell. When all cells in an electrolyser stack are assumed to be thermodynamically and electrodynamically equal, the power used in one electrolyser stack is

$$P_{stack} = P_{cell} n_{cells} \tag{2.11}$$

where n_{cells} is the number of cells per stack in the electrolyser. The power used by all electrolysers in an electrolyser plant P_{plant} will then subsequently be

$$P_{plant} = P_{stack} N_{stacks} = P_{cell} n_{cells} N_{stacks} \tag{2.12}$$

where N_{stacks} is the number of stacks in the electrolyser factory.

2.2.2. Electrolysis Techniques

This section focuses on the exploration of the three primary electrolysis techniques: Alkaline Electrolysis (AE), Proton Exchange Membrane (PEM) electrolysis, and Solid Oxide Electrolysis (SOEC). These techniques have been widely recognized and studied extensively in the field of electrolysis for hydrogen production. However, the main emphasis for this thesis will be on AE and PEM electrolysis, as the commercial availability of SOEC electrolysers is limited due to its relatively young technology.

Alkaline Electrolyser

Alkaline electrolyser technology is a very mature technology, as it has been used since 1920 and is the current standard for large-scale electrolysis. In Figure 2.5, a schematic of an AE cell is presented, along with the half-reactions occurring at the anode and cathode. In an actual electrolyser, the cells are formed like bipolar plates and a lot of bipolar plates are placed in series to create an electrolyser stack. The electrodes of an AE cell are mostly made out of nickel or cobalt, due to high activity and availability. The liquid electrolyte is mostly potassium hydroxide (KOH) or sodium hydroxide (NaOH) [Gambou et al., 2022]. Both types of electrolytes allow for the conductivity of hydroxide ions (OH^-), which act as the charge carrier in the electrolyte. A membrane, which is called the diaphragm, separates the two electrodes and enables the movement of OH^- from the cathode to the anode. The diaphragm prevents the mixing of the H_2 and O_2 molecules [Gallandat et al., 2017]. However, gas is often still able to permeate through the diaphragm in small amounts. The operating temperature range of alkaline electrolysis is between 40 and 90 °C [Pinsky et al., 2020].

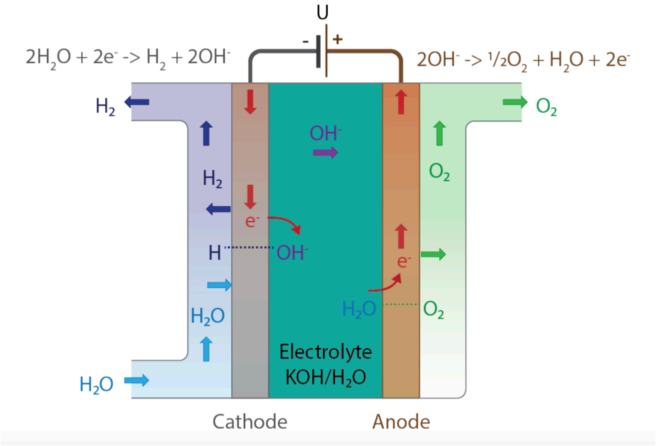

Figure 2.5: A schematic representation of an AE cell, including the half-reactions [Gallandat et al., 2017].

Compared to other electrolyser techniques, AE has the lowest system costs due to its maturity and the use of low-cost materials like cobalt, nickel, or iron electrodes. Moreover, AE cells have high durability, as a result of the stability of the cell. Unfortunately, AE cells operate at a low current density lying between 0.2 and 0.7 $A\,cm^{-2}$, which causes AE to be larger and heavier in comparison to other electrolyser techniques [Gambou et al., 2022]. Additionally, a lower boundary on the operating range is constrained due to the accumulation of gas impurities at lower current densities [Platzer and Sarigul-Klijn, 2020].

Degradation in an AE cell is mostly due to catalyst agglomeration, dissolution and detachment. The degradation mechanism that dominates depends on the type of catalysts of the anode and cathode [Lohmann-Richters et al., 2021].

Proton Exchange Membrane Electrolyser

A Proton exchange membrane (PEM) electrolyser, also known as polymer electrolyte membrane electrolyser, uses a solid polymer electrolyte membrane as opposed to a liquid electrolyte employed in AE. The utilization of PEM electrolysis is gaining significant traction and has recently become commercially available [Gambou et al., 2022]. Figure 2.6 illustrates a schematic overview of a PEM electrolyser cell, depicting its structural configuration along with the corresponding half-reactions involved in the electrochemical processes. As the membrane takes up some H_2O, it allows for H^+ ions to be conducted through the membrane, while effectively restricting the movement of the hydrogen and oxygen gas [Carmo et al., 2013]. Nafion is an example of a polymer membrane commonly used in PEM electrolysis. The temperature range for PEM electrolysis spans from 20 to 100 °C, which is almost similar to the operating temperatures observed for AE [Pinsky et al., 2020].

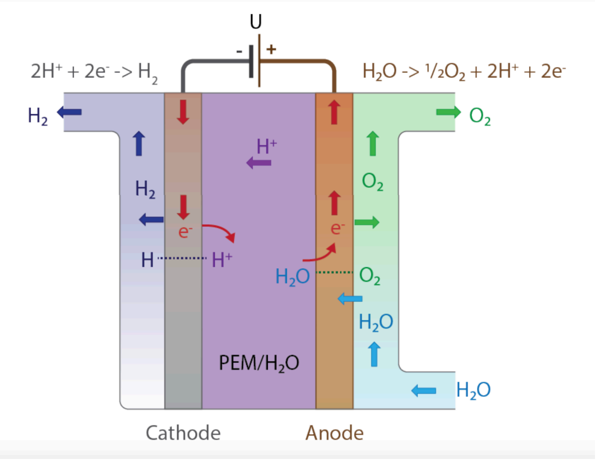

Figure 2.6: A schematic representation of a PEM electrolyser cell, including the half-reactions [Gallandat et al., 2017].

One of the notable advantages of PEM electrolysis over alkaline electrolysis is its lower ionic resistance, enabling PEM electrolysers to operate at higher current densities, typically ranging from 0.6 to 3 A cm^{-2} [Lange et al., 2023; IRENA, 2022]. Higher current densities allow for a more compact electrolyser cell design by reducing the required surface area. Moreover, Hancke et al. [2022] demonstrated that is possible to achieve economically viable PEM systems operating at pressures up to 200 bar. As explained in Section 2.2.1, operating at high pressure reduces the energy requirements for hydrogen compression, resulting in more efficient pressurized hydrogen. Additionally, PEM electrolysers exhibit fast response times as the proton transport across the membrane responds quickly to the power input [Carmo et al., 2013]. Lastly, PEM electrolysers generally have higher partial load efficiencies than AE [Salehmin et al., 2022].

However, the acidic regime of the proton exchange membrane necessitates the use of noble metal catalysts. Platinum is commonly employed as the cathode catalyst, while iridium oxide is utilized at the anode due to their high activity levels [Platzer and Sarigul-Klijn, 2020]. Unfortunately, both materials are very scarce, with iridium being one of the rarest elements in the Earth's crust. Consequently, PEM electrolysers are more expensive compared to AE [Carmo et al., 2013]. Furthermore, the acidic corrosive environment within the PEM cell results in significant degradation. Current research is targeting these disadvantages [JRC, 2021b].

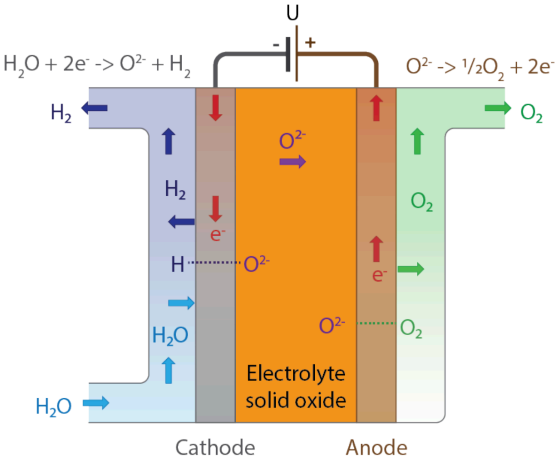

Figure 2.7: A schematic representation of an SOEC, including the half-reactions [Gallandat et al., 2017].

Solid Oxide Electrolyser

In contrast to AE and PEM electrolyser cells, Solid Oxide Electrolyser Cells (SOEC) operate within a higher temperature range of 700 to 1000 °C [Pinsky et al., 2020]. SOEC is a new technology, which is currently in the demonstration phase and not yet commercially available. A schematic of an SOEC cell can be seen in Figure 2.7, accompanied by the respective half-reactions at the anode and cathode. The SOEC is operated with steam instead of water, due to the elevated temperature range. Similar to PEM electrolysis, the electrolyte of SOEC is solid, as it consists of ceramic materials which are conductive for O^{2-} ions [Lange et al., 2023]. The most common electrode materials are nickel-doped zirconia at the cathode and strontium-doped lanthanum manganate at the anode. The current density is typically between AE and PEM electrolysers at around 0.7 A cm^{-2} [Kovac et al., 2021]

SOEC is very promising as the elevated temperatures result in a reduced electricity input requirement that needs to be supplied with electricity, with a larger portion of energy supplied in the form of heat, as is discussed in Section 2.2.1 and can be seen in Figure 2.3 [Grigoriev et al., 2020]. Moreover, the higher temperature levels enhance the reaction kinetics. As a result of these two effects, the efficiency of a SOEC is higher than for AE or PEM electrolysis [Buttler and Spliethoff, 2018]. An SOEC has the potential to further increase efficiency by utilizing medium and high-temperature heat sources, like nuclear reactors, biomass incinerators and solar thermal collectors [Wang et al., 2021]. Additionally, an SOEC has low capital costs as a result of the utilization of non-precious catalyst materials [Lange et al., 2023].

However, it is important to note that SOEC tends to produce less pure hydrogen compared to AE and PEM electrolysers due to residual steam within the system. Additionally, the substantial electrode and ceramic electrolyte degradation is a significant drawback. Degradation leads to lower durability, which needs to be improved before SOEC can become commercially available [Wang et al., 2021].

2.2.3. Electrolyser System

Electrolysers are not standalone devices and rely on additional components and machinery for their operation. This subsection covers these components and how they impact the overall system. System designs for both AE and PEM electrolyser systems vary a lot in the literature. The schematics provided in Figure 2.8 and Figure 2.9 illustrate a general configuration of an AE system and a PEM electrolyser system, respectively. The key difference between the two systems is that the electrolyte is circulated in an AE system, while only water is circulated in the PEM system.

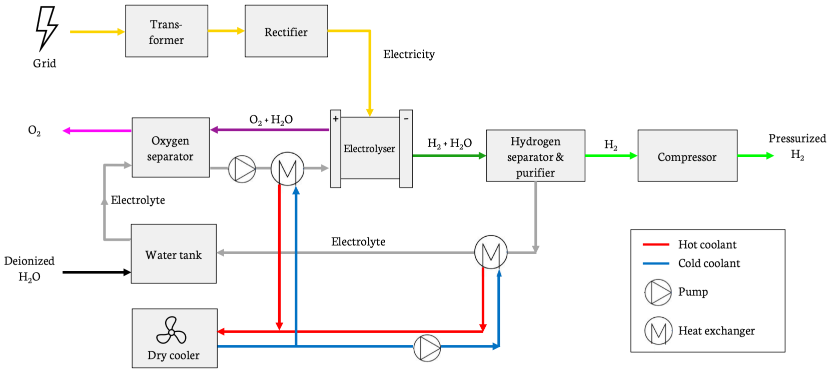

Figure 2.8: A schematic representation of the typical system design of an AE system. The different flows are indicated by different colours. This configuration is for a generic system and might not be representative of all existing AE manufacturers.

Electricity for the system is derived from the grid, where it is initially fed into a transformer. The transformer is responsible for downgrading the high grid voltage to a lower voltage suitable for the electrolyser system. Subsequently, the electricity is transferred to a rectifier. The rectifier changes the Alternating Current (AC) from the grid to Direct Current (DC), which both the AE and PEM electrolyser stacks need. There are some inevitable power losses during these two stages of electrical transformation. The extent of the losses depends on the design and manufacturing quality, and are typically around 5% combined. Following these transformations, the electricity is directed towards the electrolyser stack along with other system components that require electric power for their operation. It is important to note that only the connection between the electricity and the stack is illustrated in **??** and Figure 2.9, for the sake of simplifying the figure.

When the electrolyser is operational, it generates two product streams: a hydrogen flow from the cathode and an oxygen flow from the anode. However, both streams carry residues of the electrolyte in AE or water in PEM, requiring separation by gas-liquid separators. Moreover, water vapour in the hydrogen stream is extracted in a hydrogen purification step to achieve superior levels of purity in the hydrogen product. A hydrogen purity of

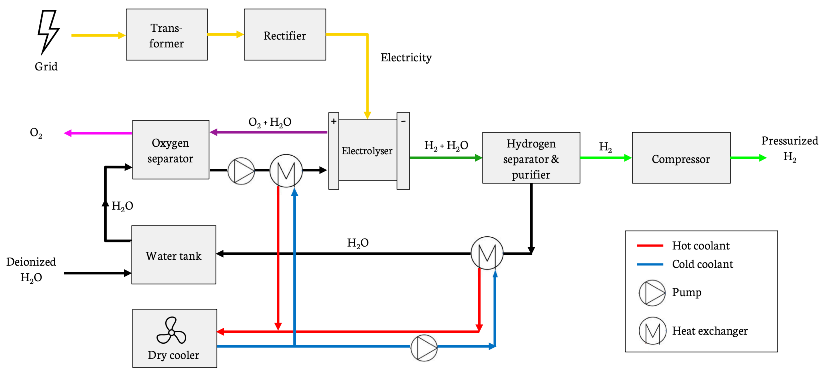

Figure 2.9: A schematic representation of the typical system design of a PEM electrolyser system. The different flows are indicated by different colours. This configuration is for a generic system and might not be representative of all existing PEM electrolyser manufacturers.

98% is enough for use in industry, but an exceptionally high purity of 99.99% is required for the application in fuel cells, which are employed in hydrogen-fueled cars and trucks [Gasunie, 2022].

During the operation of the electrolyser, heat is produced in the electrolyser, as discussed in Section 2.2.1. To maintain a steady operating temperature, it is essential to extract the produced heat from the system. Conventionally, electrolyser systems deploy heat exchangers to facilitate heat extraction from the electrolyser stacks. In heat exchangers, the thermal energy is transferred from the initial liquid to a liquid coolant. In the electrolyser design, the coolant is in turn directed to a dry cooler. The liquid coolant is often deionized water, as it has low costs and a high specific heat capacity [van der Roest et al., 2023]. A dry cooler reduces the temperature of the coolant by forcing an ambient air stream over the coolant, effectively dissipating the excess thermal energy into the surroundings. In both the standard alkaline and PEM systems, heat is extracted in two places corresponding to the oxygen and the hydrogen stream, as can be seen in Figure 2.8 and Figure 2.9.

A compressor is utilized to elevate the output pressure of the produced hydrogen. However, it is important to note that not all electrolyser systems have a compressor. The process of compression is energy-intensive, hence hydrogen is only compressed when the end-use necessitates high-pressure hydrogen. Hydrogen is typically employed at low pressures in industry, whereas high-pressure hydrogen is needed in the transport sector or high-pressure storage. When considering hydrogen as an ideal gas, the power of the compressors P_{comp} (in kW) is

$$P_{comp} = Q_{H_2} \frac{RTZ}{\eta_{compression} M_{H_2}} \frac{N\gamma}{\gamma - 1} \left[\left(\frac{p_o}{p_i} \right)^{\frac{\gamma-1}{N\gamma}} - 1 \right] \tag{2.13}$$

where Q_{H_2} is the flow rate at the inlet of the compressor in kg/s, p_i and p_o are respectively the hydrogen pressure at the inlet and outlet of the compressor, N is the number of compression stages, γ is the isentropic coefficient ($\gamma = 1.4$), η_{com} is the compressor efficiency, M_{H_2} is the molecular mass of hydrogen ($M_H = 2.016$ g mol^{-1}), T_{in} is the temperature at the inlet of the compressor and Z is the compressibility factor ($Z = 1.03$) [Dinh et al., 2023].

Furthermore, pumps are integrated into the system to enable fluid flow and circulation of the electrolyte and water over the electrolyser stack. The term Balance of Plant (BoP) refers to all necessary systems and components essential for the operation of the electrolyser. These components collectively support the functioning of the electrolyser, facilitating the conversion of electrical energy into the production of hydrogen. The compressor is not classified as part of the BoP, since it is not necessary when hydrogen is delivered at low pressures to the end user.

2.2.4. Recovery of Waste Heat

Heat Production in an Electrolyser Stack

Electrolysers operating at the thermoneutral potential neither generate heat nor consume heat. As explained in Section 2.2.1, a practical electrolyser experiences energy losses due to overvoltages. These overvoltages elevate the cell potential above the thermoneutral potential, which can be seen in the example polarization curve depicted in Figure 2.4. Consequently, electrolysis becomes an exothermic process and generates residual heat while producing hydrogen. The fundamental equation for the energy balance over an open system follows the law of conservation of energy and is expressed by

$$\frac{dE}{dt} = \dot{W} + \dot{Q} + \Sigma(\dot{m}_j h_j)_{in} - \Sigma(\dot{m}_i h_i)_{out} \tag{2.14}$$

where $\frac{dE}{dt}$ represents the change of energy in the system, $\dot{W}$ is the energy stream as a result of work that is put in the system, $\dot{Q}$ is the energy stream depicting heat entering or leaving the system, and $\Sigma(\dot{m}_j h_j)_{in}$ and $\Sigma(\dot{m}_i h_i)_{out}$ reflect energy streams as mass flows in and out of the control volume of the system [van den Akker and Mudde, 2023]. For an electrolyser, the amount of heat that is produced in the system, which needs to be removed, can be defined by

$$\dot{Q} = \dot{W} - \frac{dE}{dt} + \Sigma(\dot{m}_j h_j)_{in} - \Sigma(\dot{m}_i h_i)_{out} \tag{2.15}$$

where $\dot{Q}$ in this context can be viewed as the heat that needs to be extracted from the system. When solving this equation under stationary conditions ($\frac{dE}{dt} = 0$) the following expression can be obtained for the heat produced in an electrolyser cell

$$\dot{Q}_{Heat,cell} = (V_{cell} - V_{tn}) I_{cell} \tag{2.16}$$

Therefore, The amount of heat generated by an electrolyser cell can be defined by the difference between the actual cell potential and the thermoneutral potential. When all cells in an electrolyser stack are assumed to be thermodynamically and electrodynamically equal, the heat generated by the stack is defined by

$$\dot{Q}_{Heat,stack} = \dot{Q}_{Heat,cell} \cdot n_{cells} \tag{2.17}$$

It is worth noting that a temperature gradient exists within actual cells, where the inside portion of a cell has a higher temperature compared to the edges of the cell. Moreover, the innermost cells of a stack will have a higher temperature than the cells at the edges of a stack. The temperature difference in a practical cell will influence the local polarization curve of the electrolyser cell, meaning the performance is not uniform over the entire cell or stack. However, the assumption of a constant temperature is commonly used in literature [Hernandez-Gomez et al., 2020].

Regulations on Renewable Waste Heat

Traditionally, the residual heat from electrolysis has been deemed as an unrecoverable waste byproduct. For example, the Planbureau voor Leefomgeving (PBL) in The Netherlands has assigned a value of 0 €/MWh to residual heat from electrolysers [PBL, 2023]. Every electrolyser requires cooling during operation to maintain a constant operational temperature. The excess heat is generally dissipated into the surrounding air of the electrolyser, through a dry cooler. However, with the emergence of larger-scale electrolysers with multi-MW or GW capacities, the amount of generated waste heat becomes significant. In such cases, it would be impractical not to consider utilizing this excess heat, especially in locations where the thermal energy can be used effectively at low temperatures.

If heat can be regarded as waste heat, it can be counted towards the heating target (Article 23 of RED II) and the district heating target (Article 24 of RED II). Article 23 obliges all EU countries to increase the share of renewable energy in the heating and cooling sector by at least 1.3% over the periods 2021 to 2030. According to Article 2 of the RED II, heat is defined as waste heat if the next three requirements are met [European Commission, 2018]:

1. The heat losses are unavoidable, which means the losses can not be recovered for the same process nor reduced through the use of more efficient equipment.
2. Waste heat should be a by-product and not the intended purpose of the system.
3. Waste heat must be used via a district heating network. This implies that the waste heat must be sold on a network for off-site use. A heat network is defined as more than one customer and more than one site.

However, the RED II does not mention heat from power-to-gas processes specifically [JRC, 2021a]. Therefore, it is difficult to determine if the waste heat from electrolysers fulfils the first requirement, as there exist high-efficiency electrolysers at a laboratory scale, suggesting that heat losses may not be entirely avoidable [Baresi, 2021]. Though waste heat from electrolysers does not strictly meet the definition of waste heat as per RED II of the European Union, the generated heat is characterized by exceptionally low CO_2-emissions. This attribute makes the capture and use of waste heat from electrolysers an attractive prospect, contributing to broader sustainability goals.

Previous Works on Waste Heat Recovery of Electrolysers

Although a substantial amount of research has been devoted to optimizing electrolysis efficiencies, the exploration of residual heat utilization from electrolysis remains notably under-studied, a conclusion also drawn by Le Coultre [2022]. The bulk of the knowledge stems from master's theses and a few real projects that integrated or will integrate the recovery of waste heat. However, these projects lack detailed information about the heat recovery. There are additional studies that upgrade the waste heat through a heat pump or Organic Rankine Cycle, but those will not be discussed in this thesis.

In the thesis of Hermans [2021], the recovery of heat from an alkaline electrolyser was modelled by employing pinch analysis. In his research, a case study at the H_2ermes project in the port of Amsterdam was included, where the electrolyser operated at 80 °C and the district heating network demanded a temperature of 70 °C. The thermal efficiency, represented by η_{th}, indicates the ability of an electrolyser to recover the lost heat. A thermal efficiency of 1 indicates complete recovery of the generated waste heat, while a value of 0 implies no waste heat recovery from the electrolyser. Hermans [2021] determined that optimal heat recovery could be achieved by electrolyte cooling using a heat exchanger. He noted that the thermal efficiency ranges from 80% to 95%, depending on the operational load and lifetime of the electrolyser.

In the research by Le Coultre [2022], the heat recovery process from an alkaline electrolyser is modelled using ASPEN plus. This model incorporates separate systems for the electrochemical, thermal and cooling processes. Water is employed as a cooling fluid at an inlet temperature of 15 °C and an outlet temperature of 70 °C. The study concluded that the integration of plate heat exchangers into the electrolyser would be optimal for boosting the overall efficiency of the electrolyser.

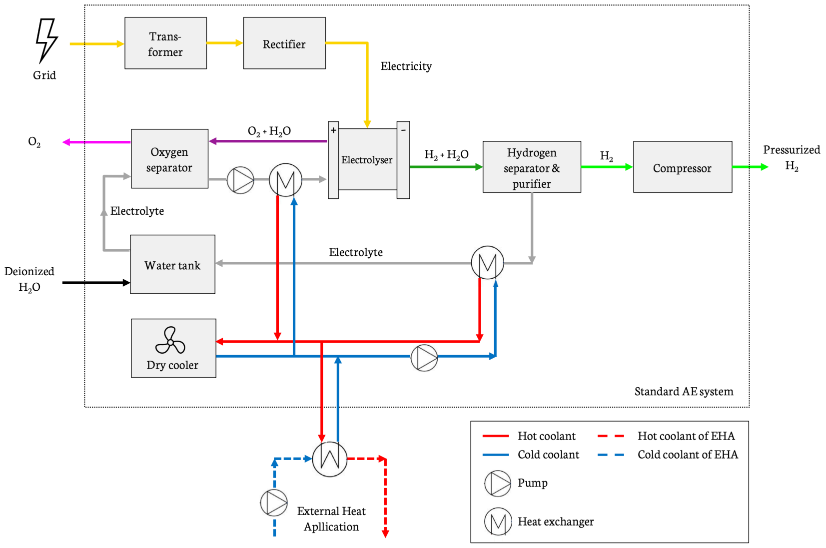

Figure 2.10: A schematic representation of the system design for an AE system that includes the recovery of waste heat. The thin dotted black line encircles the standard AE system of Figure 2.8. It is assumed that the External Heat Application (EHA) uses a liquid coolant to recover the heat.

In his study, Tiktak [2019] established a model for a PEM, which featured a cooling system integrated into the stack. This system consisted of small pores dispersed throughout the electrolyser cells. The main goal was to design and model a state-of-the-art electrolyser and compute how much heat could be effectively recovered. The conclusion drawn by Tiktak [2019] was that over 90% of the heat could be recovered by using the pore cooling system within the stack, without negatively affecting the performance of the electrolyser. However, the result depends on the operating temperature of the electrolyser. For instance, at an operating temperature of 80 °C, the electrolyser achieved a thermal efficiency η_{th} of 0.92. Unlike traditional electrolysers, the electrolyser stack modelled by Tiktak [2019] included an insulation layer. The study discovered that the majority of the heat loss was due to the enthalpy flow of water escaping the system via the O_2 product flow from the anode. Tiktak [2019] observed a substantial reduction in the quantity of water vapour in the O_2 flow, when the anode pressure was increased from 1 to 5 bar, resulting in a decreased heat loss and consequently an increased thermal efficiency. When accounting for the recovery of waste heat, the total stack efficiency was 98%.

In the study by van der Roest et al. [2023], the recovery of waste heat of a PEM electrolyser was modelled and the Levelised Cost of Heat ($LCoH_{eat}$) were calculated. The research examined three different system designs for the utilization of waste heat from the electrolyser, with some designs incorporating a heat pump and other designs not. The waste heat was recovered through a tie-in on the cooling system of the electrolyser, which resulted in a total system efficiency of up to 90%. The $LCoH_{eat}$ were between 8.4 and 36.9 €/MWh for respectively a system without or with a heat pump.

Additionally, some concrete electrolyser projects incorporate the recovery of waste heat. For instance, the project GET H2 Lingen plans to repurpose waste heat for district heating [GET H2, 2021]. In the H-Flex project, a 2 MW electrolyser of KWR in Nieuwegein is being studied for possibilities for the use of residual heat from the electrolyser [KWR, 2023]. In Hamburg, a project is underway to operate a 100 MW electrolyser by 2025, with plans to utilize the waste heat in the district heating network and for the treatment of municipal waste [HHGH, 2021]. The district heating network of Aalborg has outlined plans for the utilisation of waste heat from electrolysers in its 2050 scenario [Yuan et al., 2021]. Stromlückenfuller project involves the use of waste heat from a 200 kW electrolyser in the heating network [IKZ, 2017]. Similarly, Green Hydrogen Esslingen plans to construct a 1MW electrolyser and reuse the heat in a district heating grid [GHE, 2022]. Moreover, the 1 GW electrolyser design by ISPT includes plans for heat recovery for district-heating purposes [ISPT, 2022]. However, specific details regarding the recovery of waste heat or the performance of the recovery of heat are not available.

Electrolyser System for Heat Recovery

The general electrolyser systems for alkaline and PEM of Figure 2.10 and Figure 2.11 can be altered to include heat recovery. The heat in this thesis is recovered by a tie-in on the cooling system system. The heat is recovered from the recirculating cooling network using a heat exchanger. The heat of the electrolyte or water is first extracted to the cooling system, and next the heat is recovered from this cooling system into a system that reuses or redirects the waste heat, which is referred to as the External Heat Application. The resulting electrolyser systems including the recovery of waste heat can be seen in Figure 2.10 for the AE system and in Figure 2.11 for the PEM electrolyser system.

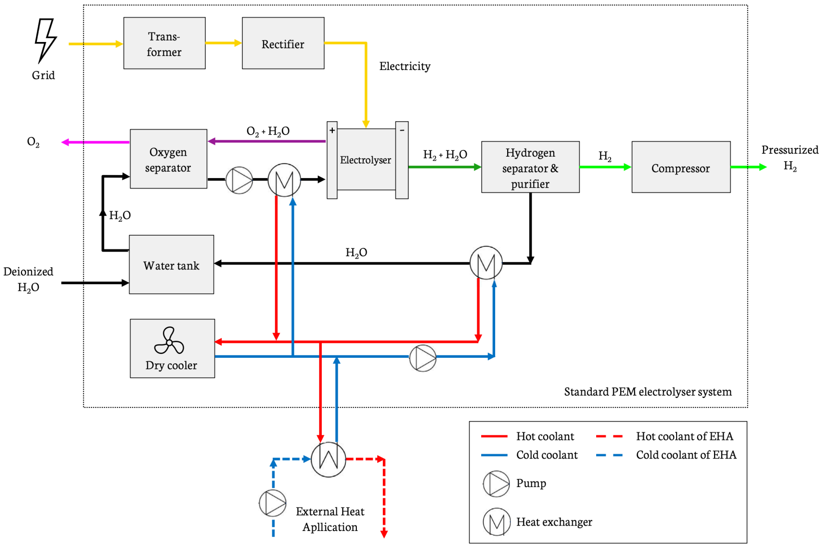

Figure 2.11: A schematic representation of the system design for a PEM electrolyser system that includes the recovery of waste heat. The thin dotted black line encircles the standard PEM electrolyser system of Figure 2.9. It is assumed that the External Heat Application (EHA) uses a liquid coolant to recover the heat.

The decision was made to integrate heat recovery without removing the existing cooling system. Instead, the heat recovery is adapted by a tie-in on the cooling system. The electrolyser can thus either be cooled through external heat consumption or by the dry cooler, when there is no external heat consumption. Choosing for a tie-in instead of replacing the dry cooler makes the system redundant. In this way, hydrogen can still be produced even if there is no heat demand. If the cooling system, including the dry cooler, were removed, the electrolyser could only operate when the heat is recovered and used by a third party or when the heat is stored. Including the dry cooler in the system eliminates this reliance, offering maximum flexibility for both the heat consumer and the hydrogen producer.

In the new electrolyser systems, it is assumed that the waste heat is recovered at a temperature that it can be directly used by a third party, without upgrading the heat. This approach eliminates the need for a costly heat pump, which is used to raise the temperature of the waste heat. For this assumption to hold, the operating temperature of the electrolyser should be substantially higher than the temperature of the waste heat. When the electrolyser is operated at a temperature around 80 or 90 °C, the waste heat can be recovered and directly used at low to medium temperatures of 50 °C to 70 °C. The outlet temperature at a heat exchanger can be selected by controlling the flow rate of the coolant through the heat exchanger. However, the designs of Figure 2.10 for AE and Figure 2.11 for PEM can be easily changed for the integration of a heat pump.

If the design of PEM electrolyser stacks with integrated cooling channels of Tiktak [2019] will be produced, the heat could also be recovered via these cooling channels. These stacks would increase the thermal efficiency as more heat would be removed. However, stacks like this are currently not in development and therefore, these stacks are not integrated into the electrolyser system designs in this thesis.

The only components that are required for the recovery of heat from an AE or PEM electrolyser system are a heat exchanger, a pump and piping for the coolant. The pump is necessary to recirculate the water and to compensate for the pressure difference over the heat exchanger. Additionally, electronics and a monitoring system are required to produce the required temperature at the outlet of the heat exchanger.

2.2.5. Electrolyser and System Efficiency

This section provides an overview of the efficiencies of an electrolyser and an electrolyser plant. The efficiencies will be presented in a bottom-up approach, starting at an individual electrolyser cell and working up to the whole electrolyser system. By examining these efficiencies, insights can be gained into the performance of the electrolysis process and where the efficiency depends on. Furthermore, this section will explain how the efficiencies can be utilized to determine the quantities of hydrogen and heat generated by the electrolyser plant. By understanding the relationship between efficiency and production output, the effectiveness of the electrolysis process can be assessed in terms of hydrogen production and heat utilization. It is important to note that all efficiencies are based on the HHV of hydrogen, as explained in Section 2.1.

The efficiency of a single electrolyser cell can be defined by

$$\eta_{stack} = \eta_{cell} = \eta_f \eta_v \eta_{deg} \tag{2.18}$$

where η_f is the Faraday efficiency, η_v is the voltage efficiency and η_{deg} is the degradation efficiency. The stack efficiency η_{stack} is equal to the cell efficiency when all cells and stacks are assumed to be thermodynamically and electrodynamically equal in an electrolyser.

The Faraday or current efficiency indicates the effectiveness of electron transfer in the system and covers the losses due to electrons being utilised for other reactions than for the electrolysis of water. Therefore, the Faraday efficiency accounts for H_2 diffusion losses and hydrogen losses through the conversion of oxygen contamination [Lettenmeier, 2021]. From the nature of the Faraday efficiency, it is assumed that the losses due to the Faraday efficiency do not contribute to the generation of heat. The Faraday efficiency is defined as the ratio between the actual hydrogen production $\dot{m}_{re,H_2}$ and the theoretical maximum amount of hydrogen production $\dot{m}_{id,H_2}$ in an electrolyser [Hernandez-Gomez et al., 2020].

$$\eta_f = \frac{\dot{m}_{re,H_2}}{\dot{m}_{id,H_2}} \tag{2.19}$$

On the contrary, the voltage efficiency describes the fraction of energy lost through overpotentials and it is defined by the ratio between the thermoneutral potential U_{tn} and the actual cell voltage U_{cell}.

$$\eta_v = \frac{U_{tn}}{U_{cell}} \tag{2.20}$$

The voltage efficiency is not constant over the load applied to an electrolyser cell since the cell potential U_{cell} changes for different current densities, as indicated by the polarization curve.

The degradation of an electrolyser cell reflects the gradual reduction of the cell performance over the operational lifespan of the electrolyser, as explained in Section 2.2.1. In this research, degradation is considered as an efficiency loss that produces heat, further explained in Section 5.2. The degradation efficiency is defined by

$$\eta_{deg} = 1 - t_{life} f_{deg} \tag{2.21}$$

where t_{life} is the time in hours the electrolyser cell has already been operational in its lifetime and f_{deg} is the degradation factor per hour. The degradation efficiency η_{deg} is initially established at 100% when the electrolyser is first put into operation and is subsequently lowered by a constant factor f_{deg} for every hour the electrolyser is operational.

The efficiency of an electrolyser stack η_{stack} is the same as the cell efficiency η_{cell} when the electrolyser cells are thermodynamically and electrodynamically equal.

$$\eta_{stack} = \eta_{cell} = \eta_f \eta_v \eta_{deg} \tag{2.22}$$

The presumption that the electrolyser cells are thermodynamically and electrodynamically equivalent throughout an electrolyser stack, is consistently applied in various sections of this research.

The total efficiency of the electrolyser stack, when actively recovering waste heat can be defined by

$$\eta_{stack,heat} = \eta_{cell,heat} = \eta_{cell} + \eta_{th} \cdot \left(1 - \eta_v \eta_{deg}\right) = \eta_f \eta_v \eta_{deg} + \eta_{th} \cdot \left(1 - \eta_v \eta_{deg}\right) \tag{2.23}$$

where η_{th} is the thermal efficiency, which is discussed in Section 2.2.4. For Equation 2.23, it is important to note that the voltage efficiency and degradation manifest as heat generation. Hence, the Faraday efficiency is not included in the second term, which accounts for the residual heat.

To express the efficiency of the whole electrolyser system, the electricity usage and losses over the supplementary components should be included. The efficiency of the supplementary components η_{suppl} is divided by the efficiency of the BoP η_{BoP} and the efficiency of the compressor η_{comp}.

$$\eta_{suppl} = \eta_{BoP} \eta_{comp} \tag{2.24}$$

The η_{BoP} covers all electricity usage and losses by the components in the BoP, where the biggest contributors are the losses of the transformer and rectifier. The efficiency of the BoP η_{BoP} is chosen from literature. The efficiency of the compressor η_{comp} (note the difference between compression and compressor efficiency) is related to the power of the compressor P_{comp} by

$$\eta_{comp} = 1 - \frac{1000 \cdot P_{comp}}{\eta_{BoP} P_{grid}} \tag{2.25}$$

where P_{grid} is the electricity (in MW) that is delivered to the electrolyser system. The compressor efficiency is assumed to be constant over the load spectrum of the electrolyser, as the compressor uses less power when less hydrogen is produced at a lower load, these reductions cancel each other.

The efficiency of the entire electrolyser system can now be defined as the multiplication of all individual efficiencies.

$$\eta_{syst} = \eta_{suppl} \eta_{stack} = \eta_{BoP} \eta_{comp} \eta_f \eta_v \eta_{deg} \tag{2.26}$$

This can viewed that the incoming electricity is partly consumed by the BoP and the compressor. However, the predominant portion of the electricity is directed towards the electrolyser. The efficiency of the entire electrolyser system, when recovering the waste heat, is defined as the multiplication of all individual efficiencies.

$$\eta_{syst,heat} = \eta_{suppl} \eta_{stack,heat} = \eta_{BoP} \eta_{comp} \left[\eta_f \eta_v \eta_{deg} + \eta_{th} \cdot \left(1 - \eta_v \eta_{deg}\right)\right] \tag{2.27}$$

The electricity used by the pump for the recovery of heat is not incorporated in this equation as it is a very small portion. In the research by Hancke et al. [2022], the pumps in the electrolyser system itself used a total of 0.0025% of the total supplied electricity, while it circulates more water than the pump in the heat recovery system does.

The power that ends up in chemical energy of H_2 molecules and the total amount of waste heat can be determined from the efficiencies. Assuming that a certain power from the grid P_{grid} is supplied to the electrolyser system, the power of the produced H_2 molecules is

$$P_{H_2} = P_{grid} \eta_{syst} = P_{grid} \eta_f \eta_v \eta_{deg} \eta_{BoP} \eta_{comp} \tag{2.28}$$

Assuming a multiplication of all the efficiencies of the electrolyser system. From the power directly used for H_2 production, the mass production flow of hydrogen $\dot{m}_{H_2}$ per hour can be defined by

$$\dot{m}_{H_2} = 3600 \frac{P_{H_2}}{Q_{H_2}} \tag{2.29}$$

where Q_{H_2} represents the chemical energy or HHV of hydrogen, while the factor 3600 is included to account for the change from seconds to hourly production. Determining the produced hydrogen requires the amount of power supplied to the electrolyser system, combined with the total system efficiency at that amount of power supplied to the system. The amount of power is often indicated by the load ratio of the electrolyser, which is a ratio of the supplied power and the full-load power. However, the system efficiency is not constant and fluctuates over the load ratio and lifetime of the stack. The load influences both the Faraday and voltage efficiency, while the lifetime of the stack influences the degradation efficiency. In the next subsections, the approach to modelling the load dependency of the Faraday and voltage efficiency for respectively AE and PEM electrolysers will be discussed.

The thermal power that is recovered from the system can be calculated using

$$P_{heat} = P_{grid}\eta_{suppl}\eta_{th} \cdot \left(1 - \eta_v \eta_{deg}\right) \tag{2.30}$$

which reflects a multiplication of the amount of produced heat and the thermal efficiency η_{th}.

2.2.6. Regulatory Requirements for Green Hydrogen

Hydrogen can be classified into different colours, representing the various production methods and feedstocks used in producing the hydrogen. Hydrogen generated through natural gas and coal is identified as respectively grey and black hydrogen. Both these production methods release significant amounts of CO_2 in the atmosphere. Blue hydrogen is also manufactured through natural gas, but it involves Carbon Capture and Storage (CCS) to sequester the emitted CO_2. Green hydrogen refers to hydrogen produced using renewable energy sources and green electricity, which does not result in GHG emissions. According to Kovac et al. [2021], the price for grey hydrogen was 1.50 € kg^{-1}, blue hydrogen was between 2 and 3 € kg^{-1}, and green hydrogen between 3.50 and 6 € kg^{-1} in 2021.

There are, however, regulatory requirements that must be satisfied before hydrogen can be classified as a green energy source. The European Union (EU) has established comprehensive guidelines on hydrogen that serve as a standard for all nations should adhere to. The Renewable Energy Directive (RED) is the overarching legal framework for the development of renewable energy across all European countries and sectors and was introduced in 2009. The recast RED (named the RED II) came into force in December 2018 as part of the "Clean energy for all Europeans" package. RED II set a target of 32% for the amount of renewable energy in the EUs energy consumption by 2030, but this was increased to 45% in September 2022, as a part of the REPowerEU plan [SolarPower Europe, 2022]. In May 2022, the European Commission launched the consultation on the two long-awaited delegated acts on Article 25(2), 27(3) and 28(5) of RED II. The first delegated act, known as the Green Hydrogen Rules, covers the criteria for fuels to be named a Renewable Fuel of Non-Biological Origin (RFNBO) and the second delegated act, named the Greenhouse Gas Emissions Rules, provides a methodology for the calculation of the life cycle GHG emissions for RFNBOs. RFNBOs are produced from renewable sources and using current techniques generally translate to hydrogen-based fuels, including hydrogen itself [van Thuyne et al., 2022]. The two delegated acts are interrelated and they will ensure that all RFNBOs are produced from renewable electricity. Adhering to the delegated acts is necessary for the fuels to be counted towards the renewable energy target of a Member State. The delegated acts apply regardless if the RFNBO is produced inside or outside the territory of the EU. The final version of the delegated acts was proposed by the European Commission in February 2023 and the European Parliament and Council have two months to accept or reject the delegated acts [European Commission, 2023c].

The first delegated act defines under which conditions hydrogen, hydrogen-based fuels or other energy carriers are considered an RFNBO in RED II. The general principle is that hydrogen produced by electrolysers is considered renewable if the used electricity is produced using renewable sources. The used electricity can be obtained via a renewable installation directly connected to the electrolyser or from the grid. For both scenarios, hydrogen producers are obligated to follow specific criteria to prove that the used electricity is derived from renewable sources.

Electricity for RFNBO is fully renewable for a direct connection between the installation generating renewable electricity if the RFNBO producer provides evidence on two points. Firstly, the installations generating renewable electricity came into operation not earlier than 36 months before the installation that produces the RFNBO, which is an electrolyser in this thesis. Secondly, the renewable electricity generating installation is not connected to the grid or is connected to the grid via a smart metering system.

The criteria for green electricity taken from the grid for RFNBO production are more extensive, as there are four sets of conditions for considering electricity from the grid as fully renewable:

1. RFNBO producers can take electricity from the grid as fully renewable if the electrolyser is in a bidding zone where the average share of renewable electricity exceeded 90% in the previous calendar year and the production of RFNBO does not exceed a maximum number of full-load hours related to the average share of renewable electricity.
2. Electricity from the grid can also be counted as fully renewable when the emission intensity of electricity is lower than 18 $gCO_2eq\ MJ^{-1}$ in the bidding zone of the RFNBO producing installation. The emission intensity of electricity in the Netherlands was 99.9 $gCO_2eq\ MJ^{-1}$ in 2020 [European Commission, 2023a].
3. Electricity taken from the grid can also be counted as fully renewable when electricity is consumed during an imbalance settlement period. The RFNBO producer should demonstrate from the evidence of the national Transmission System Operator (TSO) that electricity-generating installations running on renewable energy sources were dispatched downwards and the RFNBO-producing installation reduced the need for dispatching.
4. When the conditions of cases 1, 2 and 3 are not met, RFNBO producers can count the electricity from the grid as fully renewable if it complies with the conditions on additionality, temporal correlation and geographic correlation.

   (a) The additionality condition is complied with if RFNBO producers generate renewable electricity or have a Power Purchase Agreement (PPA) with renewable electricity producers following two criteria. Firstly, the installation generating renewable electricity came into operation not earlier than 36 months before the RFNBO plant. Secondly, the renewable electricity generating unit has not received financial support in operating or investment aid. However, the additionality condition will not apply until 1 January 2038 for RFNBO installations that came into operation before 1 January 2028.
   (b) Until 31 December 2029, the temporal correlation condition can be considered complied with if the RFNBO is produced during the same calendar month as the production of renewable electricity. From 1 January 2030, this will be changed to the same one-hour period.
   (c) The geographical correlation is considered complied with if the installation generating renewable electricity in the PPA is located in the same bidding zone as the RFNBO-producing unit. Currently, the whole Netherlands is one single bidding zone [TenneT, 2023a].

All of these criteria concentrate on avoiding the diversion of existing renewable energy generation capacity that is already utilized for other purposes. Instead, the criteria incentivise the deployment of new (additional) renewable energy generation capacity [van Thuyne et al., 2022; European Commission, 2023b].

The second delegated act establishes a minimum GHG emission saving threshold of 70% compared with fossil fuels for RFNBOs to be counted towards a Member States' renewable energy targets. The second delegated act also sets out the method for calculating the life cycle GHG emissions of RFNBOs [European Commission, 2023a]. The second act will not be explained in greater detail in this thesis, because the threshold of 70% GHG savings can be readily achieved by an electrolyser powered by electricity from wind energy [de Kleijne et al., 2022].

Next to regulations on the production of RFNBOs, the European Commission also created incentives for hydrogen use, including binding goals for the industry and transport sector in the 'Fit for 55' package in July 2021. Fit for 55 aims to reduce GHG emissions in 2030 by 55% compared to the 1990 levels [Ruttloff et al., 2023]. As part of the Fit for 55, the European Commission proposed a revision of RED II (RED III) including a target of 50% use of RFNBO in the industry sector in 2030 and the share of RFNBO has to be 2.6% in the transport sector by 2030 [Marcu et al., 2021; European Commission, 2023d]. The European Commission also adopted the Hydrogen Strategy in 2020, which sets out a vision for a European hydrogen ecosystem and infrastructure. The Hydrogen Strategy aims for 6 GW of installed renewable hydrogen electrolyser capacity in Europe in 2024 and 40 GW in 2030. Additionally, the Hydrogen Strategy plans for 40 GW of installed renewable hydrogen electrolyser capacity in Europe's neighbourhood with hydrogen export to Europe [European Commission, 2020].

The evolving regulations in the green hydrogen sector highlight the dynamic and recent nature of this field, which continues to undergo significant developments in response to advancements in technology and changing environmental requirements. Therefore, it is crucial to remain up-to-date with the latest regulatory developments in the green hydrogen sector.

2.3. Electricity from Offshore Wind Power

Green electricity is needed at the site of green hydrogen production, as described in Section 2.2.6. In this thesis, intermittent wind energy from the North Sea is considered for green hydrogen production in the Zuidplas region. This section explains the theory behind generating electricity from wind. Additionally, a PPA on wind farms in the North sea is explored.

2.3.1. Wind Turbine Theory

Wind power is an important renewable energy source because wind is non-exhaustive as it is replenished by natural processes at a faster rate than the consumption. Wind power signifies the kinetic power of air when air is moving. The power of wind through a circle of radius R is as follows:

$$P_{wind} = \frac{1}{2}\rho\pi R^2 V_{wind}^3 \tag{2.31}$$

where V_{wind} is the wind speed and ρ is the density of the medium, which is air [Zaaijer et al., 2020]

Wind power is generally harvested using wind turbines. The wind rotates the rotor blades of the wind turbine, which converts the kinetic power of air to rotational power of the blades. The generator in a wind turbine converts the rotational power to electrical power. Wind turbines cannot extract all energy from wind power, otherwise, the wind speed after the turbines would be reduced to zero, which is not possible. Betz's law indicates the maximum power that can be extracted from wind, derived from principles on conservation of mass and momentum. According to Betz's law, the theoretical maximum amount of energy that can be captured by a wind turbine is 16/27 of the total energy available in the wind. In practice, the peak of utility-scale wind turbines peaks at 75-80% of the Betz limit [Niu et al., 2018].

The power coefficient c_P is a standard metric that quantifies the ability of a wind turbine to extract mechanical energy from wind energy. Therefore, the mechanical power generated by a wind turbine can be expressed as:

$$P_{mech} = \frac{1}{2}\rho c_p \pi R^2 V_{wind}^3 = c_p P_{wind} \tag{2.32}$$

In the wind turbine drive train, the mechanical power is subsequently passed on to the gearbox, generator and electrical components. The typical electrical components used to integrate a wind turbine with the public power grid are a back-to-back converter and a transformer. The electrical components facilitate the transfer of electrical power generated by the wind turbine to the grid. Since the power conversion processes are sequential, the overall efficiency of the system can be calculated as the product of the individual drive train efficiencies. The electrical power of a wind turbine is defined by:

$$P_{elec} = \frac{1}{2}\rho \varepsilon \pi R^2 V_{wind}^3 = \varepsilon P_{wind} \tag{2.33}$$

where ε is the total efficiency of the wind turbine and is defined by

$$\varepsilon = \varepsilon_{gear}\varepsilon_{electrical}c_P \tag{2.34}$$

In Equation 2.34, ε_{gear} is the efficiency of the gearbox and ε_{gen} is the efficiency of the generator [Zaaijer et al., 2020]. As one can see, the electricity produced by a wind turbine is the power in the wind of Equation 2.31 multiplied by the total efficiency of the wind turbine ε.

The relationship between the electric output power of a wind turbine and wind speed is depicted by the power curve. The power curve is an important characteristic of a wind turbine and a schematic representation of the typical shape of a power curve for a wind turbine can be seen in Figure 2.12. The cut-in wind speed V_{cut-in} indicates the wind speed the wind turbine switches on. The rated wind speed V_{rated} refers to the wind speed at which the turbine reaches its rated power output. The rated power output is the maximum power output that a wind turbine can generate and is typically based on the design specifications of the turbine. The cut-out wind speed $V_{cut-out}$ shows the wind speed the wind turbine is switched off. The cut-out wind speed of a wind turbine specifies the maximum wind speed at which the turbine is programmed to automatically shut down to prevent damage to the turbine.

The power curve depicted in Figure 2.12 can be divided into four distinct regions by the cut-in, rated and cut-out wind speed. In region I, below the cut-in wind speed, the power output of the turbine is zero since the wind power is too low to generate electrical power. Region II, between the cut-in and rated wind speed is known as partial load region. In this region, the power output of the turbine increases rapidly with increasing wind

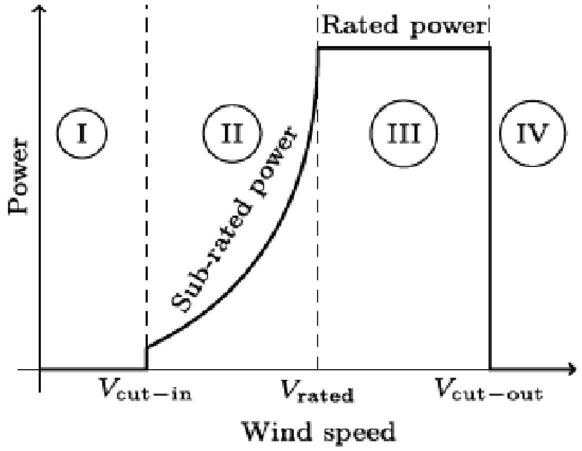

Figure 2.12: An idealized power curve for a wind turbine. The Roman numerals indicate the different regions.

speed until the rated wind speed is attained. The power output of the wind turbine is maximised by maximising the power coefficient c_P. Therefore, the power coefficient is kept constant at the maximum achievable value by keeping the tip speed ratio constant. The power of the wind turbine increases with wind speed until region III or the full-load region is reached at the rated wind speed. In the full-load region, the power output is kept constant by sustaining a constant rotational speed and diminishing the power coefficient by pitching the blades towards the wind. This reduction in blade pitch angle lowers the lift coefficient and thrust on the wind turbine blades, thereby diminishing the power coefficient. Finally, in Region IV, which is situated above the cut-out wind speed, the turbine is deactivated, resulting in zero power output.

The difference between the idealized representation of a power curve in Figure 2.12 and an actual power curve of a single wind turbine is most pronounced in the transition between the partial load region and the full-load region, whereas the transition is more gradual in an actual power curve [Zaaijer et al., 2020]. However, wind turbines in a wind farm can experience lowered wind speeds compared to a single wind turbine. A wind turbine takes up energy from the wind which lowers the energy in the wind after the turbine by decreasing the wind speed and increasing turbulence. The trail left by a wind turbine, where a wind speed deficit arises, is called a wake. The wake effects of upwind wind turbines affect wind turbines that are downwind or further inside a wind farm. Therefore, wind turbines at the outside of a wind farm straight into the wind experience a higher wind speed than wind turbines further down wind in the farm. The power production losses in a wind farm, which are due to wake effects, are referred to as aerodynamic losses. In the study of Baas et al. [2023], the aerodynamic losses of a 4 GW wind farm, consisting of 15 MW wind turbines, were 15%. The research also highlighted that these losses depend on the installed capacity of the wind turbines constituting the wind farm. There is also a secondary effect of a wind farm on the wind flow, known as the ’global-blockage’ phenomenon. The presence of a wind farm creates spatial variations in the modelled pressure field, resulting in forces acting upwind of the wind farm. These forces effectively inform the approaching airflow about the presence of the wind farm as an obstacle. As a result, the wind flow will partially deflect around and/or over the wind farm. According to Baas et al. [2023], the losses experienced by the turbines in the first row because of the global-blockage effect range between 2% and 3%. It is virtually impossible to distinguish the losses due to the blockage effect and the losses due to the aerodynamic effects for downstream wind turbines [Baas et al., 2023].

The capacity factor C_f is an important metric for renewable energy installations. The capacity factor indicates the ratio of actual energy output to the theoretical maximum electrical energy output over a certain period. The theoretical maximum electrical energy output is calculated using the rated power of the installation

$$C_f = \frac{E_{a,t_c}}{P_R t_c} \tag{2.35}$$

where E_{a,t_c} is the actual energy production in time t_c and P_R is the rated power. For wind turbines, the capacity factor depends on the size of the rotor, the rated power and the wind climate [Zaaijer et al., 2020]. According to a report of the IEA [2022a], new offshore wind projects can reach capacity factors of 50%, because of larger turbines and other technology improvements.

2.3.2. Power Purchase Agreement

As described in Section 2.2.6, electricity taken from the grid for the production of hydrogen is considered fully renewable when complying with the additionality condition. This condition postulates that the RFNBO producer has a Power Purchase Agreement (PPA) with a renewable electricity producer for an amount equivalent to at least the electricity that is used for the production of hydrogen.

A PPA is a power contractual arrangement between a (renewable) electricity generator and an electricity off-taker, specifying the terms of the purchase of electricity over a specified period. A PPA is generally a long contract of 10 to 15 years, which provides certainty to both parties regarding the price and volume of electricity supply. PPAs are an essential tool for driving the growth of renewable energy, as they enable project developers to secure stable revenue streams while offering off-takers access to affordable renewable electricity [ENGIE, 2021].

Given the intermittency of wind energy, a PPA generally stipulates that electricity is supplied only when generation occurs. The electricity delivered by the PPA will therefore follow the fluctuations of electricity production by the wind turbine. Therefore, a PPA on 3 MW offshore wind will supply 3 MW when the wind speed is above the rated wind speed and less than 3 MW when the wind speed is below the rated wind speed.

There are multiple types of PPAs. The first type is an on-site PPA, which involves the direct supply of electricity from the electricity generation plant to the consumer without using the public grid. In contrast, off-site PPAs deliver electricity to the consumer via the public grid. The electricity is not delivered to the consumer directly in this case, but the consumer receives the electricity mix from the public grid. This form of PPA creates flexibility as the electricity generation plant does not have to be located close to the consumer. Thirdly, in a virtual PPA, the flow of electricity and the financial flow are decoupled. In a virtual PPA, the produced electricity is sold on the electricity market and the consumer buys exactly the feed-in profile of the produced electricity. The electricity flow is now complemented by a Contract for Difference, in which the PPA partners commit to make additional financial payments equal to the difference between the spot price and the agreed PPA price. A virtual PPA is simple and administratively cheap [Next Kraftwerke, 2021].

In 2022, PPAs for a total of 36.7 GW of renewable power were signed according to research firm BNEF [2023]. Private companies and public institutions signed PPAs for a cumulative amount of 148 GW in renewable power since 2008, predominantly by virtual PPAs in the United States. In 2022, 8.1 GW of renewable energy PPAs was signed in Europe, led by large contracts in Spain and Scandinavia. However, PPAs are becoming increasingly more prevalent in the Netherlands [European Investment Bank, 2022]. There is a lack of available data on the pricing of PPAs on wind energy in the Netherlands. However, LevelTen Energy [2023] indicates that the wind energy PPA price is around 67 €MWh^{-1} in Europe. It should be noted that there has been a significant increase of 47% in PPA prices in Europe from 2021 to 2022, primarily attributed to the armed conflict in Ukraine [DatacenterDynamics, 2023].

2.3.3. Wind farms in the North Sea

At the end of 2022, the Dutch North Sea had seven operational wind farms that collectively had a capacity of 2,460 MW [RVO, 2023b]. The Dutch North Sea is an attractive location for wind energy as there are favourable wind conditions and a shallow water depth. By the Energy Agreement for Sustainable Growth, the Dutch government pledged to construct offshore wind farms with a combined capacity of 4,500 MW by 2023. Furthermore, the National Climate Agreement, revised in 2022, aims to achieve 21 GW of offshore wind farms in the North Sea by 2030. Achieving this goal would provide a capacity equivalent to 16% of the total energy demand in the Netherlands, and it would satisfy 75% of the total electricity consumption of 2022 [Rijksoverheid, 2022]. The locations of these wind farms are identified in the Offshore Wind Energy Roadmap in Figure 2.13 and are part of the Program North Sea. According to the North Sea Energy Outlook report published in 2020, the Netherlands will require a cumulative offshore wind capacity ranging from 38 to 72 GW in the North Sea by 2050. The 38 GW target is based on the expectation that the Netherlands will depend on significant energy imports to meet its energy needs by 2050. On the contrary, the 72 GW scenario is founded on the assumption that the Netherlands will achieve a high degree of self-sufficiency in meeting its energy requirements [RVO, 2023a].

The wind farms Hollandse Kust I and II, Hollandse Kust III and IV, and Hollandse Kust V are scheduled to come into operation by the end of 2023. Hollandse Kust VI and Hollandse Kust VII are expected to become operational in 2026. Ecowende, a partnership between Shell and Eneco, acquired Hollandse Kust VI, which can accommodate a capacity of 756 MW. On the other hand, Hollandse Kust VII, which can accommodate a capacity of 700 MW, was acquired by Oranje Wind Power II, a subsidiary of RWE [Rijksoverheid, 2022]. Both Hollandse Kust VI and VII will not receive financial support in operating or investment aid. There is no information available from Ecowende and Oranje Wind Power II regarding the type of wind turbines that will be employed, but the tenders require the utilization of turbines with a minimum capacity of 14 MW [Overheid.nl, 2022a,b].

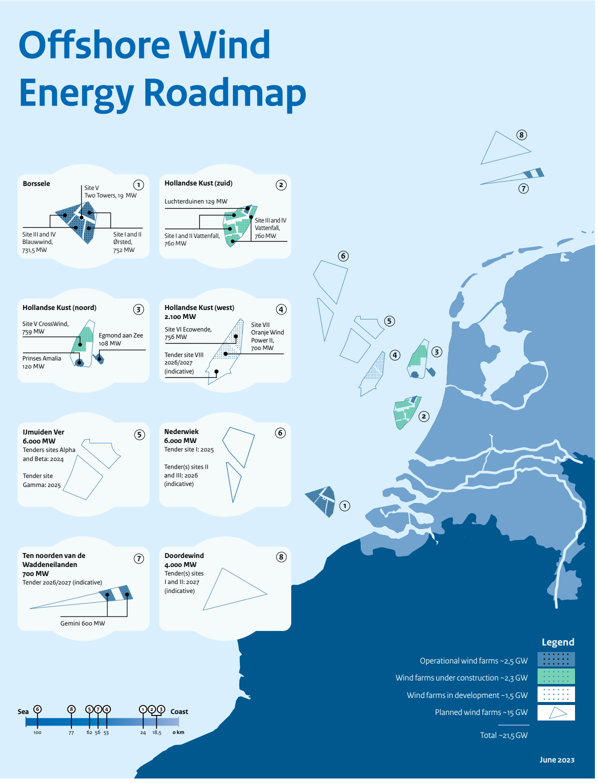

Figure 2.13: An overview of the offshore wind farms in the Dutch part of the North Sea. The figure indicates operational, planned and wind farms under construction or development [Rijksoverheid, 2022].

2.4. Levelised Cost Calculations

The most common metric when discussing the costs of generating energy, whether from fossil-based or renewable sources, is the Levelised Cost of Energy (LCoE) [Dinh et al., 2023]. The LCoE represents the average net present cost of energy production for an installation over its entire lifetime. In this thesis, the electrolyser yields both hydrogen and waste heat, leading to the determination of both the Levelised Cost of Hydrogen (LCoH_2) and the Levelised Cost of Heat (LCoH_{eat}). First, the determination of the LCoH_2 is discussed in Section 2.4.1, followed by the exploration of the LCoH_{eat} in Section 2.4.2.

2.4.1. Levelised Cost of Hydrogen

The Levelised Cost of Hydrogen (LCoH_2) serves as a metric for the average net present cost of hydrogen production throughout the system's lifespan. The calculation applies to all hydrogen-producing systems, allowing for a consistent basis to compare different methods and configurations of hydrogen production. Essentially, the LCoH_2 represents the average cost associated with producing one kilogram of hydrogen. Alternatively, one can consider LCoH_2 as the average minimum price at which the hydrogen produced by the system needs to be sold to counterbalance the total costs. The selling price at this level would make the project break even, equating the project costs with the revenue generated from the sale of hydrogen. The LCoH_2 is expressed in units of euros per kilogram of hydrogen (€/kg).

The expenses associated with producing hydrogen can be categorized into the Capital Expenditures (CAPEX), the Operating Expenses (OPEX) and the Decommissioning Expenditures (DECEX). The CAPEX encompasses costs related to the procurement and installation of the hydrogen production unit. The OPEX covers direct costs related to the operation and maintenance of all system components, which significantly includes the costs of fuel or electricity. The DECEX accounts for the costs involved in decommissioning all installations used in the hydrogen production process.

The LCoH$_2$ is calculated over the whole system lifespan T_{system} using

$$\mathrm{LCoH}_2 = \frac{\sum_0^{T_{ystem}} \frac{CAPEX_{H_2,k}}{(1+r)^k} + \sum_0^{T_{system}} \frac{OPEX_{H_2,k}}{(1+r)^k} + \sum_0^{T_{ystem}} \frac{DECEX_{H_2,k}}{(1+r)^k}}{\sum_0^{T_{ystem}} \frac{m_{H_2,k}}{(1+r)^k}} \tag{2.36}$$

where $CAPEX_k$, $OPEX_k$ and $DECEX_k$ denote the CAPEX, OPEX and DECEX in year k, respectively. The amount of hydrogen produced in year k is indicated by m_{H_2}. The LCoH$_2$ is the ratio of all discounted costs over the lifetime divided by the discounted sum of the hydrogen produced. Hydrogen production is also subject to discounting, as from an economic perspective, a kilogram of hydrogen holds more value at the present day than it will have in 5 years. To discount the costs and the produced hydrogen, a discount factor r is employed. The discount factor accounts for the time value of money, as future cash flows are discounted to a present value. It reflects the financial return and project risk of an investment. The discount factor often represents the Weighted Average Cost of Capital (WACC), which investors or companies expect to earn relative to the risk of investment.

For the electrolyser design in this thesis, the total CAPEX of the system in year k can be subdivided into the CAPEX of the electrolyser system $CAPEX_{elec,k}$, including all the BoP components, and the CAPEX of the compressor $CAPEX_{comp,k}$. Electrolyser systems generally do not include a compressor in literature, and therefore the CAPEX of the compressor is not reflected in the CAPEX of the electrolyser system $CAPEX_{elec}$. In this thesis, a compressor is utilized to raise the pressure of hydrogen so it can be used in heavy-duty trucks. Hence, the total CAPEX $CAPEX_{H_2,k}$ in year k is given by

$$CAPEX_{H_2,k} = CAPEX_{elec,k} + CAPEX_{comp,k} \tag{2.37}$$

For the CAPEX of the electrolyser, a reference value is selected based on literature, which will be discussed in Section 5.2. The term $CAPEX_{elec,k}$ also incorporates the costs for a stack replacement at the end of the stack's lifetime. The costs for the stack replacement are generally expressed as a ratio of the electrolyser system CAPEX. The CAPEX of the compressor can be determined using the power of the compressor P_{comp} of Equation 2.13 and a price per kW installed power from literature. This approach will be discussed in Section 5.2.

The total OPEX in year k for the electrolyser system examined in this thesis can be broken down into the OPEX of the electrolyser system $OPEX_{elec,k}$, the OPEX of the compressor $OPEX_{comp,k}$ and the costs for electricity $OPEX_{PPA,k}$ supplied via a PPA. Thus, the total OPEX of the system in year k is

$$OPEX_{H_2,k} = OPEX_{elec,k} + OPEX_{comp,k} + OPEX_{PPA,k} \tag{2.38}$$

The OPEX of the PPA per year can be calculated by multiplying the PPA price Π_{PPA} by the amount of electricity $E_{PPA,k}$ supplied to the electrolyser plant in year k.

$$OPEX_{PPA,k} = \Pi_{PPA} E_{PPA,k} \tag{2.39}$$

The total DECEX for the system $DECEX_{H_2,k}$ in year k is split into the DECEX of the electrolyser system $DECEX_{elec,k}$ and the DECEX of the compressor $DECEX_{comp,k}$, expressed as

$$DECEX_{H_2,k} = DECEX_{elec,k} + DECEX_{comp,k} \tag{2.40}$$

2.4.2. Levelised Cost of Heat

The Levelised Cost of Heat (LCoH$_{\text{eat}}$) follows the same principles as the LCoH$_2$. For the calculation of the LCoH$_{\text{eat}}$, only the costs associated with the additional system components that are implemented for the recovery of heat are included. Since heat is a byproduct and the electrolyser is not primarily designed to generate heat, the costs for the electricity and electrolyser itself are included under the LCoH$_2$. Therefore, solely the costs for the heat exchanger and the pump are considered in the calculation of the LCoH$_{\text{eat}}$. The costs for the additional piping are omitted from the calculation of the LCoH$_{\text{eat}}$. The LCoH$_{\text{eat}}$ is expressed in units of euros per MWh of heat produced (€/MWh) and is determined by

$$\mathrm{LCoH}_{\mathrm{eat}} = \frac{\sum_0^{T_{system}} \frac{CAPEX_{heat,k}}{(1+r)^k} + \sum_0^{T_{system}} \frac{OPEX_{heat,k}}{(1+r)^k} + \sum_0^{T_{system}} \frac{DECEX_{heat,k}}{(1+r)^k}}{\sum_0^{T_{system}} \frac{E_{heat,k}}{(1+r)^k}} \tag{2.41}$$

where $E_{Heat,k}$ represents the recovered heat in year k.

In this thesis, the CAPEX for the LCoH$_{\text{eat}}$ is calculated as follows

$$CAPEX_{heat,k} = CAPEX_{HE,k} + CAPEX_{pump,k} \tag{2.42}$$

where $CAPEX_{HE,k}$ and $CAPEX_{pump,k}$ denote the CAPEX of the heat exchanger and the pump in year k respectively. The CAPEX of the heat exchanger is calculated by [KWR, 2018]

$$CAPEX_{HE} = 1500 \cdot \sqrt{P_{HE}} \tag{2.43}$$

where P_{HE} is the maximum thermal power that the heat exchanger should be able to handle. An electrolyser generates more heat with an increase in delivered power and also degrades over the years. Hence, the heat exchanger power needs to be calculated at full-load and the end of the electrolyser stacks' lifetime. The calculation for the CAPEX of the pump, based on water pumps, is given by [van der Roest et al., 2023]

$$CAPEX_{pump} = 1150 \cdot Q_{pump}{}^{0.58} \tag{2.44}$$

where the CAPEX of the pump depends on the flow rate Q_{pump} (in m^3/h) through the pump.

In this thesis, the OPEX of the heat recovery system in year k can be split into the OPEX of the heat exchanger $OPEX_{HE,k}$ and the pump $OPEX_{pump,k}$ by

$$OPEX_{heat,k} = OPEX_{HE,k} + OPEX_{pump,k} \tag{2.45}$$

The DECEX for the heat recovery system in year k can be defined by

$$DECEX_{heat,k} = DECEX_{HE,k} + DECEX_{pump,k} \tag{2.46}$$

where $DECEX_{HE,k}$ and $DECEX_{pump,k}$ are respectively the DECEX of the heat exchanger and the pump.

3

Electrolyser Model

This chapter offers a comprehensive overview of the models used for the AE and PEM electrolyser cells. First, the approach for modelling the AE cell is discussed in Section 3.1, followed by the approach for modelling PEM electrolyser cells in Section 3.2. The models form the basis for simulating the production of hydrogen and recovery of waste heat.

3.1. Alkaline Electrolyser Modelling

To model an electrolyser, it is necessary to obtain the voltage efficiency and Faraday efficiency at all applied loads. The polarization curve provides information about the relationship between the applied current density and the corresponding cell voltage, enabling the determination of the voltage efficiency at different loads. This kind of information is protected by electrolyser manufacturers. Consequently, the primary objective of electrolyser modelling is to develop models for the polarization curve and Faraday efficiency. In this thesis, the focus for modelling the electrolysers will be on static semi-empirical and empirical models and the motivation for this choice will be discussed in Section 5.2.

3.1.1. Polarization Curve

There are multiple ways to semi-empirically model an alkaline electrolyser. The best-known semi-empirical model for an AE cell was proposed by Ulleberg [2003] and is founded upon the principles of thermodynamics as well as empirical electrochemical expressions. The polarization curve of the model is described by

$$U_{cell} = U_{rev} + [r_1 + r_2 T_{cell,c}] \cdot i_{cell} + s \cdot \ln\left[\left(t_1 + \frac{t_2}{T_{cell,c}} + \frac{t_3}{T_{cell,c}^2}\right) \cdot i_{cell} + 1\right] \tag{3.1}$$

where $T_{cell,c}$ is the cell temperature in °C. The second term of this equation reflects the ohmic overpotentials characterized by the parameters r_i and the third term reflects the activation overpotentials and is determined by the parameters s and t_i. The polarization curve of the model by Ulleberg [2003] has a temperature dependence through the r_i and t_i coefficients. To incorporate the pressure dependence in a polarization curve, Sanchez et al. [2018] proposed an extended model that builds upon the model by Ulleberg [2003]:

$$U_{cell} = U_{rev} + [(r_1 + d_1) + r_2 T_{cell,c} + d_2 p_{H_2}] \cdot i_{cell} + s \cdot \ln\left[\left(t_1 + \frac{t_2}{T_{cell,c}} + \frac{t_3}{T_{cell,c}^2}\right) \cdot i_{cell} + 1\right] \tag{3.2}$$

where additional parameters d_i are added to the model of Ulleberg [2003] to account for the pressure dependence. The coefficients r_1, r_2, d_1, d_2, s, t_1, t_2 and t_3 are constants that need to be empirically determined for a specific electrolyser. These values are specific to the particular electrolyser system for which they are calibrated. To determine the parameters of the model, experimental data can be collected from an electrolyser operating under different pressure and temperature conditions. The least-squares regression algorithm can then be employed to fit the model to the experimental data and estimate the values of the coefficients [Hernandez-Gomez et al., 2020].

3.1.2. Faraday Efficiency

The model for an AE of Ulleberg [2003] also included a semi-empirical model for the Faraday efficiency of an AE for different temperatures. The Faraday model assumes a linear temperature dependence based on four parameters f_{ij}:

$$\eta_f = \left(\frac{i_{cell}^2}{f_{11} + f_{12} T_{cell,c} + i_{cell}^2} \right) \left(f_{21} + f_{22} T_{cell,c} \right) \tag{3.3}$$

The parameters can again be determined by testing a real AE and using a least-square regression algorithm [Hernandez-Gomez et al., 2020]. Although the Faraday efficiency of an electrolyser depends on pressure, it is important to acknowledge that literature does not present an established model incorporating pressure as a determining factor in the Faraday efficiency.

3.2. PEM Electrolyser Modelling

In contrast to AE modelling, there is currently no established semi-empirical model designed for modelling the polarization curve of a PEM electrolyser. Although the semi-empirical model proposed by Sanchez et al. [2018] for AE could potentially be applied to PEM electrolysers [Hernandez-Gomez et al., 2020], this has not been explored in literature yet. As a result, empirical models are commonly used to describe the polarization curve of PEM electrolysis. In empirical modelling, each term in the equation for cell potential (Equation 2.8) is described using empirical observations, and there are various approaches in literature. In this thesis, the empirical modelling approach by Tiktak [2019] and Falcao and Pinto [2020] is followed. The approach focuses on determining the activation and ohmic overpotentials of the PEM electrolyser while omitting the condensation overpotential. In the research conducted by Hancke et al. [2022], it was determined that the condensation overpotential of a PEM electrolyser cell was only 12.3 mV when the hydrogen pressure was set at 30 bar. This finding supports the decision to omit the contribution of the condensation overpotential in the analysis.

3.2.1. Polarization curve: Activation Overpotential

Firstly, the activation overpotential is related to the additional overpotential required to overcome the activation energy of the electrochemical reactions at the anode and cathode of the electrolyser. The kinetics of the oxygen evolution reaction (OER) at the anode and hydrogen evolution reactions (HER) at the cathode are limited and influenced by various factors like the temperature, pressure and design of the catalysts. The relationship between the current density and the overpotentials can be described by the Butler-Volmer equation, which applies to the half-reactions occurring at each electrode

$$i = i_0 \left[\exp\left(\frac{\alpha z F U_{act}}{RT} \right) - \exp\left(-\frac{(1-\alpha) z F U_{act}}{RT} \right) \right] \tag{3.4}$$

where i_0 is the exchange current density, α is the dimensionless transfer coefficient, and U_{act} is the activation overpotential. For both the electrodes either the first or second exponential will dominate, which reflects the anodic and cathodic overpotential. For oxidation reactions (producing O_2 at the anode) the second term of the Butler-Volmer equation can be neglected and for the reduction reaction (producing H_2 at the cathode) the first term can be neglected [Hernandez-Gomez et al., 2020]. The Tafel equations for the activation overpotentials $U_{act,a}$ and $U_{act,c}$ for both electrodes can now be drawn up

$$U_{act,a} = \frac{RT}{\alpha_a z F} \ln\left(\frac{i}{i_{0,a}} \right) \tag{3.5}$$

$$U_{act,c} = -\frac{RT}{\alpha_c z F} \ln\left(\frac{i}{i_{0,c}} \right) \tag{3.6}$$

The charge transfer coefficients α_a and α_c represent the fraction of electrostatic potential energy affecting respectively the reduction rate at the cathode and the oxidation rate at the anode. Most reactions tend towards symmetry so both coefficients are in literature generally assumed to be equal to 0.5 [Falcao and Pinto, 2020]. The total activation overpotential U_{act} is the sum of the activation potential at the anode and cathode

$$U_{act} = U_{act,a} + (-U_{act}) \tag{3.7}$$

The exchange current densities $i_{0,a}$ and $i_{0,c}$ are also included in Equation 3.5 and Equation 3.6. The value of the overpotential is strongly influenced by the exchange current density, which in turn depends on various factors such as the temperature, type of catalyst and dimensions of the membrane. A specific value for the exchange current density is taken from literature. To model the temperature dependency of the exchange current density, an Arrhenius-type behaviour from Garcia-Valverde et al. [2012] is assumed. The Arrhenius expression can be written for both the OER at the anode and HER at the cathode as

$$i_0 = i_{0,ref} \cdot \exp\left[\frac{E_{act}}{R}\left(\frac{1}{T_{ref}} - \frac{1}{T}\right)\right] \tag{3.8}$$

where an exchange current density $i_{0,ref}$ and temperature T_{ref} from literature are utilised for both the anode and cathode. The activation energy E_{act} is empirically determined for the OER and HER at the reference exchange current density i_0^{ref} and temperature T^{ref}. The activation current density is dominated by the OER at the anode, as the HER is well reversible [Suermann et al., 2019].

3.2.2. Polarization curve: Ohmic Overpotential

Secondly, the ohmic overpotential accounts for the overpotential resulting from the ionic and electronic ohmic resistance in the electrolyser cell. The electronic resistance arises from the electronic bipolar plates and current collectors, while the ionic resistance stems from the resistance to proton transport through the proton exchange membrane, which is typically composed of Nafion in PEM electrolysers.

The ionic conductivity of Nafion σ_m is extensively studied and is often described by the next semi-empirical Arrhenius expression [Falcao and Pinto, 2020]

$$\sigma_m = (0.005139\lambda - 0.00326) \cdot \exp\left[1268 \cdot \left(\frac{1}{303} - \frac{1}{T_{cell}}\right)\right] \tag{3.9}$$

where λ represents the degree of membrane humidification. The degree of humidification can be calculated using

$$\lambda = 0.043 + 17.81a - 39.85a^2 + 36.0a^3 \tag{3.10}$$

where a is the membrane water activity. In PEM water electrolysis the membrane typically operates under nearly full humidification, which results in a water activity a of 1 [Zhang et al., 2012]. The resistance of the membrane R_m can be determined by using the membrane thickness l_m and the area of the electrolyser cell A_{cell}

$$R_m = \frac{l_m}{\sigma_m A_{cell}} \tag{3.11}$$

The electrical resistance of the current collector and bipolar plate is a smaller contributor to the overall resistance, as these components are designed to have a high conductivity [Carmo et al., 2013]. Titanium is a common material used for current collectors and bipolar plates in literature [Ito et al., 2012]. However, the current collectors are porous and the conductivity of the current collectors σ_{cc} also depends on the porosity of the current collectors. In literature, the porosity ε of the current collectors ranges from 0.5 for highly porous current collectors to 0.3 for less porous current collectors [Grigoriev et al., 2009]. A value for the conductivity of the current collectors can be obtained from literature. The resistance of the current collector R_m is expressed by

$$R_{cc} = \frac{l_{cc}}{\sigma_{cc} A_{cell}} \tag{3.12}$$

where l_{cc} is the thickness of the current collector.

The electrical resistance of the bipolar plate is influenced by factors such as the material and the design of the bipolar plate connections within the electrolyser stack. In this thesis, it is assumed that the electrolyser is cooled by the same configuration of cooling channels as in the PEM electrolyser modelled by Tiktak [2019]. The cross-sectional area for electrical conduction in the bipolar plate is taken to be 0.25 times the area of the cell, as a result of the flow distribution and cooling channels. The resistance of the bipolar plate can be calculated by

$$R_{bp} = \frac{l_{bp}}{0.25\sigma_{bp} A_{cell}} \tag{3.13}$$

where l_{bp} is the thickness of the bipolar plate and σ_{bp} is the conductivity of the bipolar plate, which is made of titanium.

Since all the layers in an electrolyser stack are connected in series, the individual ohmic resistances can be summed to get the total ohmic resistance. Consequently, the total ohmic overpotential U_{ohm} becomes

$$U_{ohm} = (R_m + 2R_{cc} + R_{bp})iA_{cell} = \left(\frac{l_m}{\sigma_m} + 2\frac{l_{cc}}{\sigma_{cc}} + 4\frac{l_{bp}}{\sigma_{bp}}\right) \cdot i \tag{3.14}$$

where l is the length, σ is the conductivity and A is the area of the layers. Each electrolyser cell in a stack is equipped with two current collectors, one located at the anode and the other at the cathode. Additionally, a single bipolar plate is responsible for connecting the cathode of one cell to the anode of the adjacent cell. Therefore, each electrolyser cell in the stack requires two current collectors and one bipolar plate, which is shown by a factor 2 in front of the resistance of the current collector.

3.2.3. Faraday Efficiency

The Faraday efficiency of a PEM electrolyser can be modelled using multiple approaches. In the study by Tiktak [2019], a constant Faraday efficiency of 0.99 is assumed. On the other hand, some other authors in literature use an empirical model for the Faraday efficiency that incorporates the current in the electrolyser cell [Yodwong et al., 2020]

$$\eta_f = 0.965 \cdot \exp\left(\frac{0.09}{I_{cell}} - \frac{75.5}{I_{cell}}\right) \tag{3.15}$$

It is important to note that the Faraday efficiency of both approaches is independent of temperature and pressure and is thus specific for electrolysers under certain conditions, but will not be applicable for other conditions. Moreover, Yodwong et al. [2020] proposes a semi-empirical model for the Faraday efficiency that takes into account the hydrogen pressure at the cathode and the current density in the electrolyser cell

$$\eta_f = (a_1 p + a_2) \cdot (i_{cell})^b + c \tag{3.16}$$

where a_1 and a_2 are parameters that account for the pressure of the electrolyser. The parameters can be determined by utilizing experimental data and employing the least-squares regression algorithm [Yodwong et al., 2020]. However, the Faraday efficiency is also linked to other parameters like the operational temperature and the thickness and material of the membrane, which are not included in this semi-empirical model.

4

Case Study: Electrolyser in Zuidplas

In this chapter, the location of the electrolyser plant in the region of Zuidplas in the Netherlands is explored. The possible advantages and disadvantages of an electrolyser in this area are discussed. First, the outline of the area is analysed in Section 4.1 and subsequently the possibilities and motivation for heat and hydrogen production in the region of Zuidplas are expounded in Section 4.2. The description of the region is important for making assumptions when applying the electrolyser models to the case study.

4.1. Location Analysis

Zuidplas is a municipality in the province South-Holland of the Netherlands and depicted on the right-hand side in Figure 4.1. It is situated above Rotterdam, with the municipality of Lansingerland directly to the left of Zuidplas. The region encompassing the cities of Berkel en Rodenrijs, Bleiswijk and Bergschenhoek in Lansingerland is commonly referred to as the B3-Hoek. As illustrated in Figure 4.1, the entire region comprises a mixture of small cities and agricultural farmland. The light and dark grey rectangles depicted in the area represent greenhouses of the horticulture sector. This region is renowned for its extensive cultivation of various vegetables, fruits, and flowers. Moreover, the A12 highway traverses through the municipalities. The areas bordering the A12 house a lot of logistic centres and therefore, the logistical hotspot at this part of the A12 highway is called the 'A12 corridor'. The A12 corridor is indicated by the green rectangles in Figure 4.1 and around Lansingerland, examples of the logistic centres are supermarkets like Albert Heijn, Jumbo, Hoogvliet, Dirk van den Broek, online clothing brands like Zalando alongside numerous other logistic centres. In Zuidplas, examples of logistics centers include transport companies Nedcargo, PostNL, LC Packaging, Doelman Logistics, as well as shops like Dille & Kamille, Lidl, and Intertoys [A12-corridor, 2021]. Both the greenhouse horticulture sector and logistics centres rely on trucks for transportation over both long and short distances. Trucks are used for long-haul transportation to other countries as well as for the distribution of products to supermarkets and shops within nearby cities in the Netherlands.

4.2. Green Hydrogen and Heat Opportunities

4.2.1. Hydrogen

In the Netherlands, several large-scale centralised electrolysers projects are scheduled, like electrolysers by Shell, BP and Uniper at the Maasvlakte near the port of Rotterdam, the H_2ermes project at the port of Amsterdam, and the ELYgator electrolyser by Air Liquide in Terneuzen. These projects are designed to have at least 100 MW of installed electrolyser capacity. The number of plans for new electrolysers is growing exponentially, particularly since the announcement of the national hydrogen network of Hynetwork Services, a subsidiary of Gasunie [Ministerie van Economische Zaken en Klimaat, 2022]. Furthermore, scenarios are developed for electrolysis to take place directly at planned wind farms above Ameland and the Dogger Bank in the North Sea [Rijksoverheid, 2023b]. Instead of transporting electricity, hydrogen will be transported from the wind farm to the shore of the Netherlands. Transporting hydrogen from an offshore wind farm to the shore incurs fewer losses compared to electricity transmission [Wagener, 2023].

However, it is worth noting that hydrogen production by electrolysers can be performed at any location that has access to water and electricity. Currently, the electricity grid in the Netherlands faces congestion issues,

Figure 4.1: Satellite photo of the region above Rotterdam. The municipalities of Zuidplas and Lansingerland are respectively encircled by blue and red. The different parts of the A12 corridor are indicated by the green rectangles. The large white rectangle indicates the outline of Figure 4.2. Edited from Google Earth [2023].

which is lowest in the North of the Netherlands and in South Holland, the province of Zuidplas [TenneT, 2023b]. Moreover, Dutch TSO TenneT and network operators Liander and Stedin are constructing a new high-voltage substation in Zuidplas. The exact location is marked by the orange triangle in Figure 4.2. The substation will be a 150-20 kV substation, which will connect to lower voltage substations or directly to consumers. This substation is expected to be finished in 2025 [TenneT, 2022].

Figure 4.2: Satellite photo of the region Zuidplas. The boundaries of this photo are indicated in Figure 4.1. The orange triangle represents the high voltage substation of TenneT, while the yellow circles indicate the current gas stations in the A12 corridor. Edited from Google Earth [2023].

The potential of green hydrogen within the Zuidplas and B3-hoek regions primarily lies in its application to trucks employed by logistic centres and the greenhouse horticulture sector. Hydrogen is considered the preferred option for making long-distance heavy-duty trucks sustainable. Although battery-powered heavy-duty trucks are technically feasible, they face practical limitations. The required battery capacity would be substantial, resulting in increased weight of the truck, and the charging time would be impractically long [Perez et al., 2021]. For these reasons, it is anticipated that hydrogen fuel cell-powered trucks will be the renewable solution for heavy-duty transportation. Regarding the hydrogen storage method for heavy-duty trucks, it remains uncertain whether the trucks will be loaded with pressurized hydrogen at 350 or 700 bar. However, the goal for heavy-duty trucks is to have hydrogen storage at 350 bar [Kast et al., 2017]. The current standard delivery pressure of hydrogen at hydrogen stations for light-duty vehicles is set at 700 bar, because of tight packaging [Hancke et al., 2022].

The Dutch government set a target for 50 hydrogen stations in the Netherlands by 2025, as outlined by Rijksoverheid [2022]. It is reasonable to anticipate that one of these hydrogen stations will be installed in the Zuidplas region to cater to the heavy-duty trucks operated by logistic centres. The current refuelling stations in the A12 corridor are indicated by yellow dots in Figure 4.2, accompanied by the respective owners of these stations. Notably, some of these gas stations are exclusively designated for truck refuelling purposes.

In addition to the potential application in heavy-duty trucks, green hydrogen can also be effectively utilized by the greenhouse horticulture sector. Currently, the horticulture sector primarily relies on cogeneration units, fueled by natural gas, to provide heat for the greenhouses. However, with the potential inclusion of the agricultural sector in future emissions reduction schemes like the European Emission Trading Scheme (ETS), there is a growing need to explore low-carbon alternatives [Verschuuren, 2022]. By replacing the existing cogeneration units with hydrogen-powered units, the greenhouse horticulture sector can transition to a cleaner and more sustainable energy source.

In this thesis, it will be assumed that the produced hydrogen is delivered to a conceptual hydrogen station in the region Zuidplas. The delivery of green hydrogen will therefore be assumed to be by a direct pipeline from the hydrogen plant to the hydrogen station at 350 bar. However, the case for a delivery pressure of 700 bar will also be examined in the sensitivity analysis. As the produced hydrogen is directly delivered at the hydrogen station, storage of hydrogen at the plant is not considered.

4.2.2. Heat

As explained in Section 2.2.4, the electrolysis of water results in the generation of waste heat due to overvoltages, which increase the cell voltage beyond the thermoneutral voltage U_{tn}. However, most of the projects planned in the Netherlands do not currently address the utilization of this waste heat. The Netherlands aims for 8 GW electrolyser capacity by 2032 [Rijksoverheid, 2023a], which implies that the amount of waste heat is substantial.

In the region of the B3-hoek in Lansingerland, there already exists a heat network. The current heat network is represented by the light red en solid green lines in Figure 4.3. The light red lines indicate the existing pipelines, the dark red lines indicate the planned pipelines and the solid green lines outline the areas that are currently supplied with heat. The green dotted lines in this figure indicate the areas that also seek to be connected to the heat network.

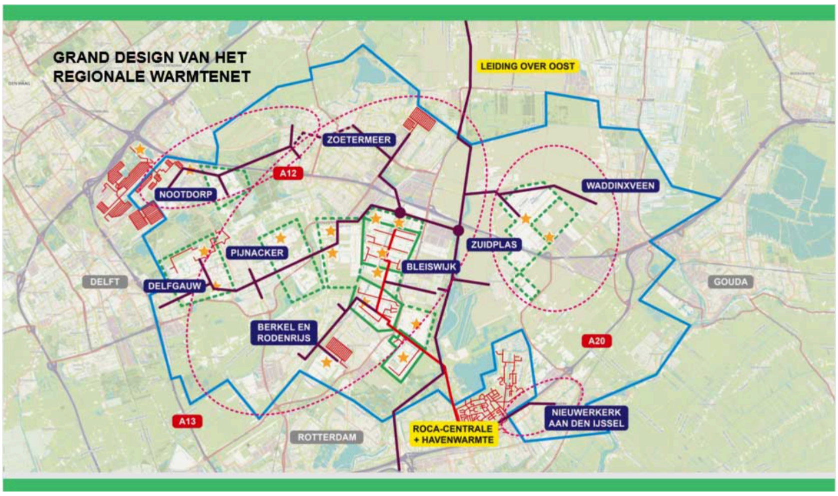

Figure 4.3: Schematic view of the layout of the heat network in Lansingerland and Zuidplas [Warmtenetwerk, 2021].

The current heat network is connected to Uniper's RoCa Combined Heat and Power (CHP) plant. Uniper owns the primary transport line of the heat network, depicted by the thick light red line in Figure 4.3, whereas Eneco owns the distribution grid, represented by the slim light red lines. The heat network supplies heat to horticulturists in the B3-hoek, where the heat is generated by the RoCa plant to match the heat demand. The total heat demand of the 120 connections is approximately 2.2 PJ per year [RVO, 2021]. To supply heat to the network, water is utilized with a feed temperature of 70 °C and a tap temperature of 40 °C. This temperature range allows for the effective transfer of heat to the connected users within the network, ensuring that the required heating demands are met.

However, the heat network in the entire area is set to undergo a thorough redesign. The goal of the redesign is to transform the centralised heat network with a single supplier and a limited number of consumers to a decentralised heat network with multiple heat suppliers and a large consumer base [Warmtenetwerk, 2021]. The planned pipelines, depicted as the dark red lines in Figure 4.3, will connect the entire area, including consumers and producers in Zuidplas, to this decentralised heat network. As part of the redesign, there are plans to incorporate geothermal plants into the heat network. Additionally, there are considerations to connect residual heat from the port of Rotterdam to the heat network. The goal of Eneco is that all supplied heat is CO_2-neutral by 2035. The total heat demand for the whole region connected to the heat network encompasses approximately 1,200 ha of greenhouses and around 110,000 houses. It is assumed that the first additional pipelines will be finished around 2025 [Greenport West-Holland, 2022].

An opportunity arises to connect an electrolyser located in Zuidplas as a heat supplier to the scheduled heat network in the region. The residual heat is a waste stream from a process that uses green electricity and thus has a low carbon footprint. The low carbon footprint aligns with the goal of Eneco for a CO_2-neutral heat network and reducing the reliance on fossil-fuel-based heat generation methods. Moreover, the residual heat can be utilized as a base load in the heat network. Given that the residual heat does not incur a lot of additional operating costs, it can be marketed as a sustainable and cost-effective source of heat in Zuidplas. This integration not only enhances the sustainability of the region but also contributes to the overall energy efficiency by utilizing both the produced green hydrogen and the residual heat of the electrolyser.

Uniper indicated that the inlet temperature and outlet temperature of this district heating network are respectively 70 °C and 40 °C. In this thesis, it will be assumed that these temperatures are constant over the entire year. It will be assumed that the hydrogen production plant is next to the connection of the district heating network, so losses in supplying the heat to the network are omitted.

5

System Design and Boundaries

In this chapter, the system design and system boundaries of the model for determining the Levelised Cost of Hydrogen ($LCoH_2$) and the Levelised Cost of Heat ($LCoH_{eat}$) are discussed. The system design and boundaries review the design properties and input data of the electrolyser and levelised costs model. The assumptions for the system design are motivated in the text by logical reasoning and are generally substantiated by corresponding values in literature.

Noteworthy, assumptions and decisions in modelling the wind and electrolyser systems are discussed in the next chapter. It is important to indicate that the electrolyser system is assumed to be operational from the start of 2027. The influence of certain design parameters and economic parameters on the $LCoH_2$ and $LCoH_{eat}$ will be researched through a sensitivity analysis. Therefore, ranges for the sensitivity analysis are supplied for these parameters.

This chapter is split into three sections. Firstly, the wind power system is described in Section 5.1, which specifies how the power data from a wind farm is produced. The power data is used as input for the electrolyser systems. Next, the design of the electrolyser system is described in Section 5.2. The system design of the electrolyser is used to simulate the amount of hydrogen produced and heat recovered at a certain wind power load. Finally, the levelised costs analysis combines the results and determines the $LCoH_2$ and $LCoH_{eat}$. The economic parameters for the levelised costs model are discussed in Section 5.3.

5.1. Wind Power System

First, the wind power system is examined. The goal of this subsystem is to produce power data that reflects the electricity production of a wind farm. The power data obtained from the wind power system is subsequently utilized as an input for the electrolyser system, which constitutes the next system in this thesis.

The electrolysis plant in Zuidplas is scheduled to be operational at the start of 2027. For the production of green hydrogen, the electrolysis plant should follow the conditions in the delegated acts of RED II of the European Union, discussed in Section 2.2.6. The additionality condition requires the renewable energy installation to not come into operation earlier than 36 months before the electrolysis plant. Therefore, this model will assume that the wind power is generated by the wind farms Hollandse Kust VI and VII (indicated by number 4 in Figure 2.13), which will come into operation in 2026, as discussed in Section 2.3.3. To comply with the temporal correlation condition, the wind generated by Hollandse Kust VI and VII will be directly coupled to the electrolyser via a virtual PPA, which is explained in Section 2.3.2. A virtual PPA is the most optimal, as it is simple and administratively cheap. The geographical correlation is automatically complied with as the Netherlands is considered one single bidding zone.

A technique that is often used to generate the electricity production of a wind turbine is using an idealized power curve like the power curve in Figure 2.12. When using the local wind speed at the wind turbine, the power production of the wind turbine can be determined at that wind speed. Subsequently, the power production of a wind farm can be determined when employing this method for all turbines in the wind farm. However, the power curve for a wind farm differs from the power curve for an individual wind turbine as discussed in Section 2.3.1.

In this thesis, the wind power production data from Baas et al. [2023] will be used as the input data of this model. Baas et al. [2023] analysed the energy production including wake losses for six hypothetical 4 GW wind farms. To this end, one year of actual weather data is simulated for these wind farms using the GPU-Resident

Atmospheric Simulation Platform (GRASP) Large-Eddy Simulation (LES) model. LES can capture essential aspects of wind farm flow by numerically integrating the conservation of mass, momentum, temperature and moisture. LES has been playing a leading role in the field of wind farm flow physics research for quite some time. The LES of Baas et al. [2023] is driven with data from the ERA5 reanalysis dataset from the European Centre for Medium-Range Weather Forecasts (ECMWF). The ERA5 dataset is the fifth generation of atmospheric reanalysis of the global climate covering the period from January 1940 to the present day [Hersbach et al., 2020]. The ERA5 dataset provides hourly estimates of numerous atmospheric, land, and oceanic climate variables with a horizontal resolution of 31 km and is often used for renewable energy resource assessments [ECMWF, 2023]. The ERA5 data is open source and can be downloaded from the Copernicus Climate Change Service (C3S) website using an API.

The dataset provided by Baas et al. [2023] contains various parameters that are the result of the simulations and are related to the power production and wind speed measurements for all individual wind turbines of the six simulated wind farms. These parameters are at 15-minute intervals and include the power production data, the thrustless power production data, the rotor disk-average wind speed, the thrustless rotor disk-average wind speed, and the corresponding time of measurement. The thrustless variables indicate the values that are observed if the modelled wind farm and the wake effects would not be present, so if the wind turbine was a single isolated turbine. The rotor-averaged wind speed represents the average wind speed experienced by the wind turbine rotor.

Baas et al. [2023] simulates the power production for six 4-GW wind farms. In this thesis, the results for scenario 6 will be used, which reflects the layout of the IJmuiden Ver wind farm. The data of Baas et al. [2023] is centred around 52.866 °N and 3.536 °E, corresponding to a location approximately 100 km from the Dutch coast in the planned IJmuiden Ver wind farm, which is indicated by number 5 in Figure 2.13. However, the wind farms of focus of this thesis, Hollandse Kust VI and VII are centred at 52.608 °N and 3.763 °E, approximately 35 km away. Hollandse Kust VI and VII are indicated by number 4 in Figure 2.13. The power data of scenario 5 is based on the NREL IEA 15MW wind turbine [NREL, 2020]. The details of the NREL IEA 15MW wind turbine and wind farm are depicted in Table 5.1. The use of the NREL IEA 15MW wind turbine is in agreement with the plans for Hollandse Kust VI and VII, which mandate the utilization of at least a 14 MW wind turbine, as discussed in Section 2.3.3. The installed wind power density of the power data of IJmuiden Ver is 10.4 MW km^{-2}, which closely approximates the power density of Hollandse Kust VI and VII, mandated at 8.6 MW km^{-2}. However, it is worth noting that the IJmuiden Ver wind farm is situated slightly farther from the Dutch coast compared to the Hollandse Kust VI and VII wind farms. Additionally, IJmuiden Ver is a 4 GW wind farm and Hollandse Kust VI and VII are respectively 700 and 760 MW. The influence of the wake and global-blockage effect on the power production of the wind farm will be overestimated compared to power production by Hollandse Kust VI and VII.

Table 5.1: The technical parameters for the NREL IEA 15MW wind turbine in the wind farm employed by the data from Baas et al. [2023].

Parameter	**Value**
Wind turbine installed capacity	15 MW
Hub height	150 m
Rotor diameter, *D*	240 m
Power density	10.4 MW/km^2
Number of installed turbines	268
Spacing	5.6 *D*

The power data from Baas et al. [2023] is 15-minute interval average data and is only simulated for the year 2015, which does not cover the entire lifetime of the electrolyser being studied in this thesis. As the power data is produced using weather data from the ERA5 dataset, the power production data from Baas et al. [2023] and the wind speed data of ERA5 are correlated to each other. Therefore, the power data will be coupled to ERA5 wind speed data at the same location (52.8659 °N and 3.5364 °E in the IJmuiden Ver wind farm) and time (during 2015) as the power data from Baas et al. [2023]. When combining the ERA5 data and power production data at the same moments in time and plotting a fit to the data, a 'wind farm power curve' can be constructed. This wind farm power curve indicates the power produced by the wind farm at certain ERA5 wind speeds.

When feeding the wind farm power curve with ERA5 wind speed data, the power produced by the wind farm can be obtained at that wind speed. As the ERA5 wind speed is available over a much longer time, the power data can be extended to the lifetime of the electrolyser system. In this way, the simulation of the electrolyser system is not tied to the one year of original power production data supplied by Baas et al. [2023], but used as a benchmark for the behaviour of the wind farm for different ERA5 wind speeds.

As the simulation in this thesis is focused on the Hollandse Kust VI and VII, the ERA5 wind speed at that location (52.608 °N and 3.763 °E) can be used for determining the power production via the wind farm power curve. When using the ERA5 wind speed of the new location, the assumption is inherently made that the wind farm power curve exhibits the same behaviour at both locations. But, as mentioned before, the locations only differ by 35 km. The location of Hollandse Kust VI and VII is closer to the shore, thus it is expected that the average wind speed will be lower, and less power will be produced compared to the original data at the IJmuiden Ver location.

This study assumes that the full power agreed upon in the PPA on Hollandse Kust VII and VII is delivered to the electrolysis plant. Any losses that incur during the transportation of electricity are assumed to be the responsibility of the electricity producer or the Transmission System Operator ($P_{PPA} = P_{grid}$). Furthermore, it is assumed that the PPA covers the entire lifetime of the electrolysis plant, implying a stable PPA price. The starting point of the historical ERA5 wind speed data will be 1993, which will thus be the input of the first year of operation of the electrolysis plant, reflecting 2027. Following this trend, the year 2003 will be assumed to be the wind delivered in 2037, and the year 2016 will reflect the wind delivered in 2050.

The wind farm power curve can be scaled to the amount of power agreed to in the PPA, allowing for the calculation of the electricity supplied to the electrolysis plant. By retrieving ERA5 wind speed data spanning the entire operational lifespan of the electrolyser, it becomes possible to compute the corresponding power output generated by the wind farm. This 'wind farm power curve method' simulates the electricity supplied by the wind farm based on actual wind speed data over the whole lifetime of the electrolyser system, providing more accurate results compared to methods relying on idealized scenarios.

5.2. Electrolyser System

In this section, both the AE and PEM electrolyser system designs for the region Zuidplas are discussed, including the recovery of waste heat. It is then assumed that all components of the electrolyser system use the same fraction of electricity at lower loads. The values of the parameters chosen refer to the base case, whereas differences in the values of the parameters are researched by the sensitivity analysis.

As discussed in Section 4.2, there are numerous distribution centres along the A12 corridor and greenhouse horticulture in the B3-Hoek en Zuidplas. In this thesis, it is assumed that all the hydrogen produced from the starting year of 2027 will be supplied to a hydrogen refuelling station in the area. The delivery is assumed to be facilitated by a direct pipeline operating at 350 bar, which is the pressure used for storage tanks on hydrogen trucks. The delivery of hydrogen is justifiable given the regulatory requirement for the transport sector to use 2.6% of RNFBOs from 2030, as stated in Section 2.2.6. The $LCoH_2$ for delivery at 700 bar will also be evaluated. For the compressors, hydrogen will be viewed as an ideal gas.

In this thesis, it will be assumed that the waste heat will be recovered and supplied to the district heating network, as discussed in Section 4.2. The district heating network is presupposed to have an outlet temperature $T_{DHN,out}$ of 40 °C and an inlet temperature $T_{DHN,in}$ of 70 °C. The coolant, or cooling fluid, is assumed to be deionized water. It is further assumed that the district heating network maintains consistent outlet and inlet temperatures throughout the year. Additionally, it is postulated that the hydrogen production plant is situated directly adjacent to the connection point of the heating network, thereby eliminating any losses in heat supply to the network.

In the delegated acts of the REDII, it is not specified whether the electricity used by the BoP and compressor for the production of green hydrogen should also be derived from green sources or can simply be drawn from the grid. In this thesis, it is assumed that the electricity is indeed green and is also covered by the PPA. Hence, the electricity utilized by the BoP and compressor of the electrolysis plant reduces the electricity used by electrolysers for hydrogen production.

The AE and PEM electrolyser system designs in this study will be based on the electrolyser system designs designed for heat recovery that are discussed in Section 2.2.4. These systems allow for efficient recovery of waste heat, without impeding the production of hydrogen.

The operating temperature for both the alkaline and PEM electrolyser systems is postulated to be 80 °C. The rationale behind this assumption is that the waste heat generated at this temperature can be directly transferred to the district heating network at a temperature of 70 °C. This approach eliminates the necessity for a costly heat pump to upgrade the waste heat to a higher temperature. The selected temperature of 80 °C is at the upper end of the range for operating temperatures for both types of electrolyser systems, as discussed in Section 2.2.2. It is assumed that the internal cooling system recovers the heat at 76 °C, while the input temperature is 73 °C. A small temperature difference of ΔT 3°C will not influence the electrolyser system [van der Roest et al., 2023]. With these parameters, it is feasible to recover heat from the cooling system and supply it to the district heating network at 70 °C. The final designs for the system and process flow for both the alkaline and PEM electrolyser systems are visually depicted in Figure 5.1 and Figure 5.2, respectively. The final system designs are based on the proposed system design for heat recovery in Section 2.2.4.

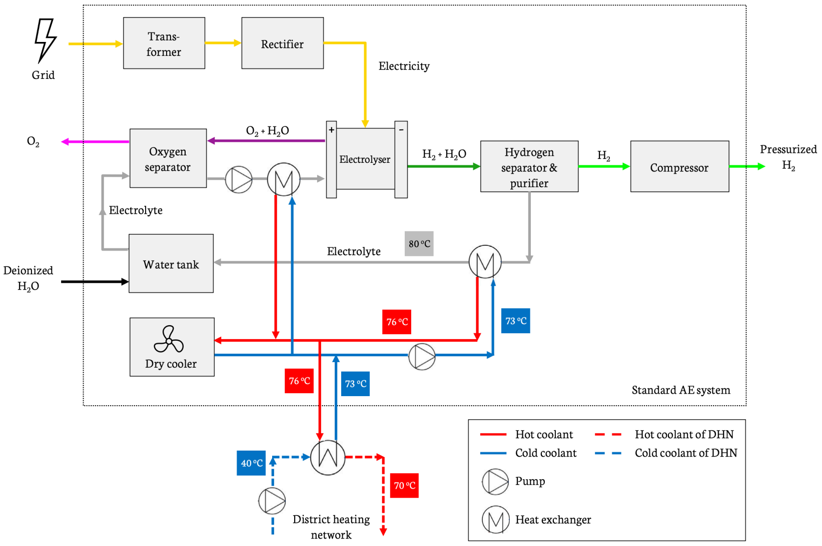

Figure 5.1: A schematic representation of the system design for an AE system that includes the recovery of waste heat, which is supplied to a district heating network. It is assumed that the district heating network uses a liquid coolant that can be heated in a heat exchanger. The differences in the dashed and solid lines are indicated in the legend. The thin dotted black line encircles a general AE system. The expected temperatures of the different pipes transporting coolant are indicated by the temperature in the corresponding boxes.

The operating pressures for the electrolyser stacks are selected to be in line with those used in previous studies. The operating pressures for the alkaline electrolyser are set at 5 bar at the cathode and 1 bar at the anode, following the specifications used by Sanchez et al. [2018]. For the PEM electrolyser, the operating pressures are set at 30 bar for the cathode and 5 bar for the anode. An operating pressure of 30 bar is generally employed in state-of-the-art PEM electrolysers [Hancke et al., 2022]. An elevated pressure at the anode of the PEM electrolyser (5 bar) serves to reduce the water vapour content in the oxygen outlet, thereby enhancing the thermal efficiency, as discussed in Section 2.2.4.

The installed capacity of the electrolysis plant is not subject to any particular constraint. The demand for heat in the district heating network is substantial, and ample space is available to accommodate the plant's area requirements. Furthermore, the newly constructed high-voltage substation provides sufficient capacity for electrical power input. The only concern relates to ensuring an adequate level of hydrogen offtake in the area. For this study, an electrolysis plant with an installed capacity of 10 MW is assumed, where the sensitivity analysis ranges from 5 to 15 MW. The amount of power agreed upon in the PPA is equal to the installed capacity of the plant. This means for a plant of 10 MW, a PPA of 10 MW will be assumed and similarly, for a plant of 15 MW a PPA of 15 MW will be assumed ($P_{PPA,max} = P_{instal}$).

In literature, system lifespans T_{system} for both the alkaline and PEM systems are reported between 20 and 30 years [Buttler and Spliethoff, 2018; IRENA, 2022; Le Coultre, 2022]. However, some sources suggest that the lifetime of PEM systems may be shorter [Gambou et al., 2022]. In this thesis, the system lifespan is assumed to be the median value of 25 years. A sensitivity analysis will further investigate the impacts of varying the system lifespan within the range of 20 to 30 years.

The lifetime of electrolyser stacks differs between alkaline and PEM electrolysers. Alkaline electrolysers, being a more mature technology, tend to have longer stack lifetimes. Literature commonly reports lifetimes of around 80,000 hours for alkaline stacks [Gambou et al., 2022; Grigoriev et al., 2020; Schmidt et al., 2017]. A study by IRENA [2022] projects that the stack lifetime for both PEM and alkaline electrolyser stacks could reach 120,000 hours by 2050. In this thesis, a stack lifetime of 80,000 hours is assumed and the sensitivity analysis investigates the impact of the stack lifetime within a range of 60,000 to 120,000 hours. PEM electrolysers, on the other hand, have shorter stack lifetimes due to the acidic conditions within the PEM cells, which can accelerate degradation [Suermann et al., 2019]. This results in a stack lifetime of approximately 60,000 hours. The sensitivity analysis for PEM electrolysers will examine a range of 40,000 to 100,000 hours [Gambou et al., 2022; Schmidt et al., 2017; Giampieri et al., 2023]. However, advancements in electrolyser technology are anticipated to improve the lifetime of the stacks.

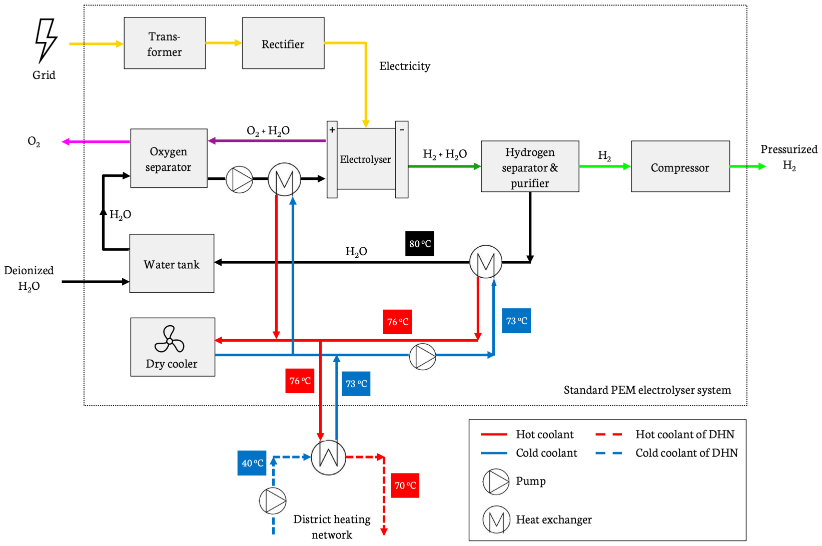

Figure 5.2: A schematic representation of the system design for a PEM electrolyser system that includes the recovery of waste heat, which is supplied to a district heating network. It is assumed that the district heating network uses a liquid coolant that can be heated in a heat exchanger. The differences in the dashed and solid lines are indicated in the legend. The thin dotted black line encircles a general PEM electrolyser system. The expected temperatures of the different pipes transporting coolant are indicated by the temperature in the corresponding boxes.

The literature presents a wide range of values for the stack efficiencies of AE and PEM electrolysers. Stack efficiencies based on the HHV are often reported between 65% and 80% for AE and between 70% and 80% for PEM electrolysers [Gambou et al., 2022; Grigoriev et al., 2020; Carmo et al., 2013; Schmidt et al., 2017; IRENA, 2022]. Some sources indicate a higher stack efficiency for PEM electrolysers, while others suggest a higher stack efficiency for alkaline electrolysers. In this study, the full-load start-of-life stack efficiency $\eta_{stack,SoL,FL}$ is assumed to be 70% for the AE stacks, and 75% for the PEM electrolyser stacks. This difference reflects the electrolysers that the stacks are based upon, as reported by Sanchez et al. [2018] and Tiktak [2019]. Sensitivity analyses are conducted over ranges of 65% to 75% for AE and 70% to 80% for PEM electrolyser stacks.

The active area of the electrolyser cell is generally around 2 to 4 m^2 for AE and 0.15 to 1 m^2 for PEM electrolysers [Lange et al., 2023; IRENA, 2022; Holst et al., 2021]. This disparity is a direct consequence of PEM electrolysers operating at higher current densities, which reduces the required active area. The area of the electrolyser cell in this thesis is set at 3 m^2 for alkaline electrolysers and at 0.5 m^2 for PEM electrolysers.

The load range of alkaline electrolysers is constrained at the lower end of the operating range, primarily due to the lateral diffusion of hydrogen to the anode side when production rates are low. This can lead to the creation of a flammable mixture [Buttler and Spliethoff, 2018]. Literature often assumes a technical limit of 15% for these systems [IRENA, 2022; Gambou et al., 2022], which is also adopted in this thesis. For PEM electrolysers, most manufacturers indicate no technical limit on the minimum load. This is primarily due to the low gas permeability of the membrane, which prevents the formation of flammable mixtures even at very low production rates [Buttler and Spliethoff, 2018]. There are also indications in literature that PEM electrolysers could operate at loads up to a maximum of 160% for brief periods without significantly accelerating degradation [Grigoriev et al., 2020].

The degradation factor for alkaline electrolysers is assumed to be $1.05 \cdot 10^{-4}$ %/h, while for PEM electrolysers it is assumed to be $1.2 \cdot 10^{-4}$ %/h. These values are in line with the degradation goals for 2026 as suggested by JRC [2021b]. It is assumed that the rate of degradation is the same regardless of the load percentage, as long as the electrolyser cell is operational. The sensitivity analysis considers a range from 0.5 to $1.6 \cdot 10^{-4}$ %/h for alkaline electrolysers and from 0.7 to $1.7 \cdot 10^{-4}$ %/h for PEM electrolysers.

The efficiency of the BoP, which encapsulates all systems required for the operation of an electrolysis plant excluding the compressor, is assumed to be 94% as indicated by Hancke et al. [2022]; van der Roest et al. [2023]. The sensitivity analysis investigates a range of this efficiency between 90% and 98%.

The higher thermal efficiency for PEM electrolysis, according to Tiktak [2019], arises from the higher current density leading to a more compact cell design, thereby concentrating the heat and facilitating easier recovery. Consequently, the thermal efficiency for the PEM system is assumed to be 90% in this study, with a sensitivity analysis probing the range from 80% to 95%.

The thermal efficiency of the AE and PEM electrolyser system is set based on the work of Hermans [2021] for the alkaline system and based on van der Roest et al. [2023] and Tiktak [2019] for the PEM system. In the thesis by Hermans [2021], a thermal efficiency between 83 and 93% is observed through pinch analysis, using an alkaline electrolysis system at 80 °C. In this study, a thermal efficiency of 87.5% is assigned to the alkaline system, with the sensitivity analysis exploring a range of 80 to 95%. For the PEM system, Tiktak [2019] noted a thermal efficiency of 92% at 80 °C for a PEM electrolyser, while van der Roest et al. [2023] adopted a more conservative estimate of 80%. Tiktak [2019] argued that PEM electrolysis has higher thermal efficiency than alkaline electrolysis due to its greater current density, leading to a more compact cell design. This results in more concentrated heat, making it easier to recover the heat from the electrolyser. Following this argument, the thermal efficiency of the PEM electrolyser system is set at 90%, with a sensitivity analysis evaluating the range of 80 to 95%.

When considering the compressor, divergent compression efficiencies $\eta_{compression}$ (for Equation 2.13) are reported in literature. Dinh et al. [2023] mentions a compression efficiency of 75%, while Hollingsworth et al. [2019] reports a higher efficiency of 92%. Hollingsworth et al. [2019] argues that the compression efficiency when compressing hydrogen is relatively high as the valve loss power is lower. The compression efficiency will be assumed to be 85% in this thesis. The maximum hydrogen flow rate $Q_{H_2,max}$ is observed under full-load conditions, as this corresponds to the peak hydrogen production. Utilizing Equation 2.13 with the maximum hydrogen flow rate $Q_{H_2,max}$ enables the calculation of the power required by the compressor. The hydrogen flow rate Q_{H_2} can be established without considering the electricity losses to the BoP for the compressor to provide an overestimate of the compressor power, serving as a safety margin. The compressor power depends on the installed plant capacity P_{instal}, given that the hydrogen flow rate at the outlet of the electrolyser depends on the plant size. For an installed plant capacity of 10 MW, the compressor power P_{comp} for the AE system is 404 kW and 217 kW for the PEM system. The power consumed by the compressors is proportional to the load placed on the electrolyser system. The difference in compressor power can be attributed to the fact that the H_2 pressure of the AE stack is 5 bar, while the H_2 output pressure of the PEM electrolyser stack is 30 bar. As a result, the PEM electrolyser system needs less compression, hence more electricity can be directed to the stack when compared to the AE system.

The installed power of the heat exchanger P_{HE} within the district heating loop is contingent upon the maximum amount of heat recovered during the lifetime of the electrolyser stack. The installed power significantly influences the CAPEX related to the heat exchanger. To determine the maximum amount of heat recovered, it is crucial to utilize the degradation efficiency at the end-of-life of the stack, as the most significant heat generation occurs at this stage due to degradation. Furthermore, the voltage efficiency at full-load is chosen since the maximum amount of heat is produced under full-load conditions. The maximum amount of heat that is recovered during the lifetime of the system is given by

$$P_{HE,EoL,fullload} = P_{instal}\eta_{sys}\eta_{th} \cdot \left(1 - \eta_{v,fl}\eta_{deg,EoL}\right) = P_{instal}\eta_{sys}\eta_{th} \cdot \left(1 - \eta_{v,fl}\left[1 - t_{stack}f_{deg}\right]\right) \tag{5.1}$$

which is based on Equation 2.30. However, a safety margin of 5% will be applied to the heat exchanger installed power to account for cases where increased degradation leads to a higher heat output. When considering an installed plant capacity P_{instal} of 10, the resulting heat exchanger installed power is 2,655 kW_{th} for the AE and 2,636 kW_{th} for the PEM electrolyser system.

The maximum flow rate of a pump determines the size of the pump and is thus important for the CAPEX. The maximum flow rate of the pump in the district heating loop depends on the heat production at full-load at the end-of-life of the stacks, as argued for the heat exchanger. The maximum flow rate of the pump $Q_{pump,max}$ in the heat exchanger system can be calculated by

$$Q_{pump,max} = 3600 \cdot \frac{P_{instal}\eta_{sys}\eta_{th} \cdot \left(1 - \eta_{v,fl}\left[1 - t_{stack}f_{deg}\right]\right)}{c_s\rho\left(T_{DHN,in} - T_{DHN,out}\right)} \tag{5.2}$$

where c_s represents the specific heat capacity, which is 4186 J kg^{-1} K^{-1} for water, and ρ is the density of the substance, which is 1,000 kg m^{-3} for water. The numerator corresponds to the amount of heat production per second at end-of-life and full-load. The denominator reflects the amount of joule that can be absorbed by a cubic meter of water being heated from $T_{DHN,out}$ (40 °C) to $T_{DHN,in}$ (70 °C). The factor of 3600 accounts for the conversion from seconds to hours, as $Q_{pump,max}$ is expressed in m^3/h. A safety margin of 5% is added to the max flow rate of the pump. Applying this equation with the safety margin results in a designed flow rate Q_{pump} of 76.11 m^3/h for the pump in the AE system and 75.56 m^3/h for the pump in the PEM electrolyser system. The maximum heat production during the lifetime of the alkaline system is higher than the PEM electrolyser system. This phenomenon will be explained in Section 6.2.

The system design for the PEM electrolyser is more detailed, as additional design parameters are required in the determination of the polarization curve. The current collector is postulated to have a porosity ε of 0.37 which results in a conductivity of the current collector of σ_{cc} = 145 S cm^{-1} [Grigoriev et al., 2009]. Furthermore, the thickness of the current collectors is assumed to be 1 mm, the thickness of the bipolar plates 2 mm and the thickness of the membrane is assumed to be 125 µm [Carmo et al., 2013].

The results of the system design and boundaries are summarised in Table 5.2 and Table 5.3 corresponding to the AE and PEM electrolyser system, respectively. The primary differences between the two systems lie in the operating pressure, start-of-life efficiency, stack lifetime and degradation factor.

Table 5.2: The technical parameters for the AE system. The motivation for the values and ranges are discussed in the text. If the range is left blank, the parameter will not be explored through a sensitivity analysis.

Parameter	**Value**	**Range for Sensitivity Analysis**
Installed plant capacity, P_{instal}	10 MW	5 - 15 MW
Operating temperature, T_{cell}	80 °C	
Operating pressure at cathode, p_{H_2}	5 bar	
Operating pressure at anode, p_{O_2}	1 bar	
System lifespan, T_{system}	25 yr	20 - 30 yr
Stack lifetime, t_{stack}	80,000 h	60,000 - 120,000 h
Full-load start-of-life stack efficiency, $\eta_{cell,SoL,FL}$	70%	65% - 75%
Area of cell, A_{cell}	3 m^2	
Load range	15% - 100%	
Degradation factor, f_{deg}	$1.05 \cdot 10^{-4}$ % h^{-1}	$0.5 \cdot 10^{-4}$ - $1.6 \cdot 10^{-4}$ % h^{-1}
Balance of Plant (BoP) Efficiency, η_{BoP}	94%	90% - 98%
Thermal efficiency at 80 °C, η_{th}	87.5%	80% - 95%
Hydrogen delivery pressure, p_{del}	350 bar	5 - 700 bar
Inlet temperature district heating network, $T_{DHN,in}$	70 °C	
Outlet temperature district heating network, $T_{DHN,out}$	40 °C	
Number of compression stages, N	2	
Compression efficiency, $\eta_{compression}$	85%	
Compressor installed power P_{instal} of 10 MW, P_{comp}	404 kW	
Heat exchanger installed power P_{instal} of 10 MW, P_{HE}	2,655 kW$_{th}$	
Flow rate of pump in heat exchanger system, Q_{pump}	76.11 m^3 h^{-1}	

Table 5.3: The technical parameters for the PEM electrolyser system. The motivation for the values and ranges are discussed in the text. If the range is left blank, the parameter will not be explored through a sensitivity analysis.

Parameter	Value	Range for Sensitivity Analysis
Installed plant capacity, P_{instal}	10 MW	5 - 15 MW
Operating temperature, T_{cell}	80 °C	
Operating pressure at cathode, p_{H_2}	30 bar	
Operating pressure at anode, p_{O_2}	5 bar	
System lifespan, T_{system}	25 yr	20 - 30 yr
Stack lifetime, t_{stack}	60,000 h	40,000 - 100,000 h
Full-load start-of-life stack efficiency, $\eta_{cell,SoL,FL}$	75%	70% - 80%
Area of cell, A_{cell}	0.5 m^2	
Load range	0% - 100%	
Degradation factor, f_{deg}	$1.2 \cdot 10^{-4}$ % h^{-1}	$0.7 \cdot 10^{-4}$ - $1.7 \cdot 10^{-4}$ % h^{-1}
Balance of Plant (BoP) efficiency, η_{BoP}	94%	90% - 98%
Thermal efficiency at 80 °C, η_{th}	90%	80% - 95%
Hydrogen delivery pressure, p_{del}	350 bar	30 - 700 bar
Inlet temperature district heating network, $T_{DHN,in}$	70 °C	
Outlet temperature district heating network, $T_{DHN,out}$	40 °C	
Number of compression stages, N	2	
Compression efficiency, $\eta_{compression}$	85%	
Compressor installed power P_{instal} of 10 MW, $P_{comp,max}$	217 kW	
Heat exchanger installed power for P_{instal} of 10 MW, P_{HE}	2,636 kW_{th}	
Flow rate of pump in heat exchanger system, Q_{pump}	75.56 m^3 h^{-1}	
Membrane thickness, l_m	125 µm	
Current collector thickness, l_{cc}	1 mm	
Bipolar plate thickness, l_{bp}	2 mm	

5.3. Levelised Costs System

This section focuses on determining the economic parameters for the calculation of the $LCoH_2$ and the $LCoH_{eat}$. The system design of the levelised costs model is summarized in Table 5.4.

The electrolyser is scheduled to be operational in 2027, which marks year 1 in the levelised costs framework. As the construction of the electrolysis plant will require some time, it is assumed that 2026 will be used for the construction of the electrolysis plant. Therefore, 2026 marks year 0 in the levelised costs system and is the year that the CAPEX of all the components are assumed to be paid. Starting from year 1 (2027), the plant begins to produce hydrogen and heat. This year will also mark the beginning of the OPEX payments. The DECEX is assumed to occur the year following the lifetime of the electrolyser. In the case of a 25-year electrolyser system, the DECEX would occur in year 26. In literature, the OPEX and DECEX of industrial installations are typically considered as a fraction of the CAPEX.

The calculation of the $LCoH_2$ includes all system components and required feedstocks that to build and operate the electrolysis plant. Conversely, the calculation of the $LCoH_{eat}$ only considers the additional system components necessary to recover the waste heat, as discussed in Section 2.4.2. In this view, only the heat exchanger and the pump are included in the calculation of the $LCoH_{eat}$, as elucidated in Section 2.4.2.

As highlighted in Section 2.4, the discount factor r serves as a vital economic parameter that reflects the investment risk. It accounts for the time value of money and hydrogen or heat produced in Equation 2.36 and Equation 2.41. According to literature, discount rates of 5% to 8% are observed for hydrogen projects [Dinh et al., 2023; van der Roest et al., 2023; Taghizadeh-Hesary et al., 2021]. In this thesis, a discount rate of 6% is selected, with a range of 2% to 10% explored in the sensitivity analysis.

There is a wide range of the CAPEX for AE and PEM electrolyser systems reported in the literature. The electrolyser CAPEX encompasses all costs for constructing the electrolyser system. It includes the purchase, installation, site preparation, and contingency expenses. The CAPEX of an electrolyser system is expressed in the price per installed plant capacity. Values between 500 and 1,000 €/kW are reported for AE systems [Holst et al., 2021; IRENA, 2022; ISPT, 2022; Buttler and Spliethoff, 2018; Glenk and Reichelstein, 2019]. A general downward trend in AE system CAPEX over the last years is recognized by both Glenk and Reichelstein [2019] and IRENA [2022]. In this thesis, an AE CAPEX of 700 €/kW is selected, while the sensitivity analysis looks at a range from 400 to 1,100 €/kW. For PEM electrolyser systems, values reported in literature range between 800 and 1,300 €/kW, with most of them falling around 800 and 900 €/kW[Holst et al., 2021; Tromp et al., 2022; IRENA, 2022; ISPT, 2022; Glenk and Reichelstein, 2019; Giampieri et al., 2023; Hancke et al., 2022]. Glenk and Reichelstein [2019] recognizes a strong decline in the CAPEX of PEM electrolyser systems, as the technology heads toward maturity. A CAPEX of 850 €/kW is selected for PEM electrolyser systems in this thesis, with the sensitivity analysis considering a range between 500 and 1,300 €/kW.

The CAPEX of the electrolyser stacks, for both the AE and PEM electrolyser systems, are postulated to be 35% of the total electrolyser system CAPEX [Tromp et al., 2022; Hancke et al., 2022]. This metric is a key consideration when modelling the CAPEX of the stack replacements at the end of their lifetime. This includes the costs for decommissioning of the old stacks and installing the the new stacks.

The CAPEX of the compressor is a subject of discussion in literature. Dinh et al. [2023] reports a compressor CAPEX of around 1,000 €/kW, while Ozaki et al. [2014] reports a compressor CAPEX of around 11,500 €/kW, and Ulleberg et al. [2010] indicates a compressor CAPEX of around 5,000 €/kW. In the study of Hancke et al. [2022], the compressor CAPEX was set at 3,800 €/kW. As the outlet pressure of 350 bar in this thesis is quite high, the compressor CAPEX is set at 4,500 €/kW. The sensitivity analysis will evaluate the range between 1,500 €/kW and 7,500 €/kW. The compressor power P_{comp}, which is reported in the previous section, can be used to calculate the CAPEX of the compressor. The CAPEX of the compressor for respectively the AE system and PEM system at 10 MW are 2,019,900 € and 978,730 €. The AE system necessitates greater compression for the hydrogen flow, thereby resulting in a higher CAPEX for its compressor as compared to the PEM system. Since the CAPEX of the compressor depends on the compressor power, the CAPEX of the compressor will also vary with installed plant capacity P_{instal}.

The CAPEX of the heat exchanger can be calculated using Equation 2.43 and the installed power P_{HE} of the heat exchanger. However, this value solely accounts for the purchase of the heat exchanger. Therefore, an installation factor of 1.5 is employed to cover the installation, including the tie-in on the cooling system of the electrolyser system. The CAPEX of the heat exchanger depends on the installed plant capacity P_{instal} through the heat exchanger installed power P_{HE}. For a plant capacity of 10 MW, the heat exchanger CAPEX for the AE and PEM systems are respectively 115,940 € and 115,440 €.

Through the use of Equation 2.44 and the flow rate Q_{pump} of the pump, the CAPEX of the pump can be determined. As with the heat exchanger, an installation factor of 1.5 is used. Similar to the CAPEX of the compressor and the heat exchanger, the CAPEX of the pump in the district heating loop will depend on the installed plant capacity P_{instal}. At an installed plant capacity of 10 MW, the CAPEX of the pump for the AE and PEM systems are 21,280 € and 21,170 €, respectively.

The OPEX of both PEM and alkaline electrolyser systems typically falls within the range of 1.5% to 3% of the CAPEX, as reported in several studies [Tromp et al., 2022; Giampieri et al., 2023; Dinh et al., 2023; van der Roest et al., 2023; Hancke et al., 2022]. In this thesis, a value of 2% is selected for the OPEX of both PEM and alkaline electrolysers. The sensitivity analysis will further examine an OPEX range of 1 to 4%. For the compressor, an OPEX value of 3% is utilized in this thesis, as suggested in literature [Dinh et al., 2023; Giampieri et al., 2023]. The OPEX of the compressor will not be considered in the sensitivity analysis due to its relatively minor contribution to the $\mathrm{LCoH_2}$. The OPEX for both the heat exchanger and the pump used in the district heating loop is set to 2%, in accordance with van der Roest et al. [2023].

Internal documents of Uniper suggest an expected cost for a PPA on offshore wind in the North Sea to fall between 60 and 80 €/MWh. This range aligns with the average European PPA price of 67 €/MWh, indicated by LevelTen Energy [2023]. This study will use the median price of 70 €/MWh, assuming constant pricing throughout the lifetime of the electrolyser system. Variations in the PPA price Π_{PPA} are reviewed through a sensitivity analysis. The OPEX for the electricity input for a certain year can be determined by multiplying the total electricity $E_{PPA,k}$ supplied during that year to the plant by the PPA price Π_{PPA}, using Equation 2.39. The sensitivity analysis will examine a broad range from a PPA price of 30 to 150 €/MWh.

The DECEX for both the electrolyser and compressor is assumed to be 2% of the electrolyser and compressor's respective CAPEX, as noted in the study by Dinh et al. [2023]. The DECEX of the heat exchanger and pump in the district heating loop is also assumed to be 2% of their respective CAPEX. The DECEX of all system components are not included in the sensitivity analysis as they are relatively small one-time expenses. Moreover, these expenses occur at the end of the lifetime of the system, resulting in a low present value. Consequently, the influence of DECEX on the $\mathrm{LCoH_2}$ and $\mathrm{LCoH_{eat}}$ will be almost negligible.

Table 5.4: The technical parameters for the levelised costs system. The motivation for the values and ranges is discussed in the text. If the range is left blank, the parameter will not be explored through a sensitivity analysis.

Parameter	**Value**	**Range for Sensitivity Analysis**
Discount Factor, r	6%	2% - 10%
AE system CAPEX, $CAPEX_{AE}$	700 € kW^{-1}	400 - 1,100 € kW^{-1}
PEM system CAPEX, $CAPEX_{PEM}$	850 € kW^{-1}	500 - 1,300 € kW^{-1}
Electrolyser stack CAPEX, $CAPEX_{stack}$	35% of $CAPEX_{elec}$	
Compressor CAPEX,	4,500 € kW^{-1}	1,500 - 7,500 € kW^{-1}
AE heat exchanger CAPEX, $CAPEX_{HE,AE}$	115,940 €	± 50%
PEM heat exchanger CAPEX, $CAPEX_{HE,PEM}$	115,440 €	± 50%
AE heat exchanger pump CAPEX, $CAPEX_{pump,AE}$	21,280 €	± 50%
PEM heat exchanger pump CAPEX, $CAPEX_{pump,PEM}$	21,170 €	± 50%
Electrolyser OPEX, $OPEX_{elec}$	2% of $CAPEX_{elec}$	1% - 4% of $CAPEX_{elec}$
Compressor OPEX, $OPEX_{comp}$	3% of $CAPEX_{comp}$	
PPA price, Π_{PPA}	70 € MWh^{-1}	30 - 150 € MWh^{-1}
Heat exchanger OPEX, $OPEX_{HE}$	2% of $CAPEX_{HE}$	1% - 4% of $CAPEX_{HE}$
Heat exchanger pump OPEX, $OPEX_{pump}$	2% of $CAPEX_{pump}$	1% - 4% of $CAPEX_{pump}$
Electrolyser DECEX, $DECEX_{elec}$	2% of $CAPEX_{elec}$	
Compressor DECEX, $DECEX_{comp}$	2% of $CAPEX_{comp}$	
Heat exchanger DECEX, $DECEX_{HE}$	2% of $CAPEX_{HE}$	
Heat exchanger pump DECEX, $DECEX_{pu}$	2% of $CAPEX_{pump}$	

6

System and Model Application

In this chapter, the system design of the previous chapter is related to the wind power system and electrolyser model, resulting in modelling decisions and assumptions. Intermediate results are presented on the behaviour of the wind farm power curve or electrolyser system which are verified and validated if possible. The analysis is conducted on an hourly basis, encompassing the entire operational lifespan of the electrolyser system. As a result, the model is simulated under steady-state conditions. This implies that a particular state remains constant throughout an hour before transitioning to a different state in the subsequent hour. Modelling the electrolyser under steady-state conditions implies a simplification of the dynamics of the system. The focus of this research is on the overall system performance during a state and not on the detailed dynamic behaviour between states. In this chapter, intermediate results are presented on the behaviour of the wind farm power curve or electrolyser system.

First, the wind power system and determination of the wind farm power curve are discussed in Section 6.1. Next, the model of the AE and PEM electrolyser systems are discussed in Section 6.2. In modelling the electrolyser systems, intermediate results for the efficiency of the electrolyser system are discussed. Lastly, the levelised costs model is discussed shortly in Section 6.3.

6.1. Wind Power System

As explained in Section 5.1, the wind farm power curve will be set up by plotting the ERA5 wind speed data and the power production data for scenario 6 from [Baas et al., 2023] at the same location and time. For this aspect, the ERA5 wind speed data is obtained for 2015 at the same location as the IJmuiden Ver wind farm, which is 52.866 °N and 3.536 °E.

The ERA5 wind speed is obtained on an hourly basis in the u-direction and v-direction, which respectively indicate the eastward and northward component of the wind speed. By supplying the wind speed in 2 directions, both the horizontal wind speed and the direction can be determined. The wind speed in the u-direction and v-direction can be combined to the horizontal wind speed $V_{wind,ERA5}$ by using a simple Pythagoras theorem.

$$V_{wind,ERA5} = \sqrt{V_{u,wind,ERA5}^2 + V_{v,wind,ERA5}^2} \tag{6.1}$$

where $V_{u,wind,ERA5}$ and $V_{v,wind,ERA5}$ represent the ERA5 wind speed in the u- and v-direction respectively.

The thrustless rotor-averaged wind speed and power production data from Baas et al. [2023] are on a 15-minute interval and have to be averaged to match the hourly ERA5 wind speed data. The data is averaged in a way that resulted in the highest correlation between the power production data and the ERA5 wind speed data by using the R-squared as an indicator. The R-squared is a statistical metric that represents the extent to which the variance of a certain parameter can be explained by another parameter. In this case, it indicates how much of the variation in the thrustless rotor-averaged wind speed can be explained by the ERA5 wind speed. The highest R-squared during averaging was 0.981.

The ERA5 wind speed is available at a height of 10 m and 100 m. The ERA5 wind speed data represents the wind conditions in the absence of free flow, thus in the absence of a wind farm. On the other hand, the thrustless rotor disk-average wind speed dataset from [Baas et al., 2023] also represents the wind speed without the presence of a wind farm. As both wind speeds indicate the wind speed of free flow, the correlation can be evaluated when they are plotted for the same time points. For the calculations, the thrustless rotor-averaged wind speed is averaged over the 268 wind turbines in the wind farm. The result for the ERA5 wind speed at 10 m and 100 m is presented in Figure 6.1. The findings indicate that the ERA5 wind speed at a height of 100 m has a stronger correlation with the thrustless wind speed dataset, than the ERA5 wind speed at a height of 10 m. This observation is consistent with expectations, as the thrustless wind speed is rotor-averaged at a hub height of 150 m, making it more aligned with the ERA5 wind speed at a higher elevation. Moreover, the observed correlation between the two datasets displayed some polynomial characteristics, which is consistent with the anticipated non-linear relationship between wind speed and height. Based on these findings, the subsequent discussions and analyses in this thesis will focus on the ERA5 data at a height of 100 m, as it demonstrates a stronger correlation with the thrustless wind speed dataset.

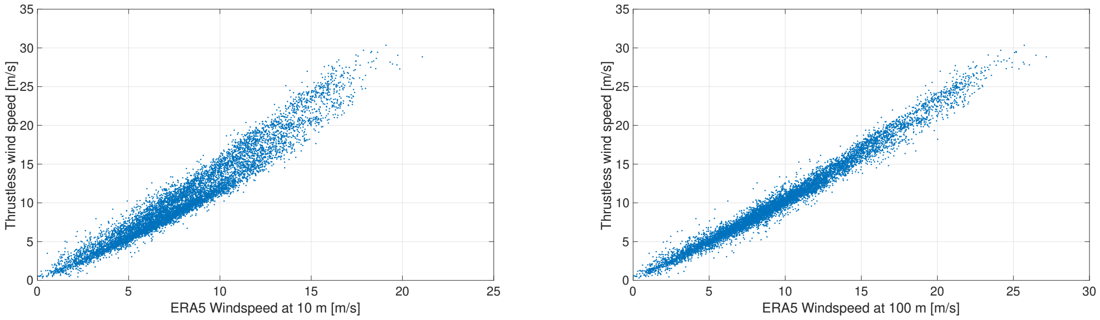

(a) ERA5 wind speed at a height of 10 m

(b) ERA5 wind speed at a height of 100 m

Figure 6.1: Plots of the thrustless disk-average wind speed and the ERA5 wind speed at a height of 10 m and 100 m.

By combining the ERA5 data and power production data at the same moments in time and plotting a fit to the data, a ’wind farm power curve’ can be constructed. The wind farm power curve indicates the power produced by the wind farm at certain ERA5 wind speeds. In this thesis, the wind farm power curve is scaled to the original turbine power of 15 MW. The wind farm power curve takes into account various factors such as wake effects within a wind farm, the global-blockage effect of a wind farm, and the gradual transitions between different production regions of a power curve, as discussed in Section 2.3.1.

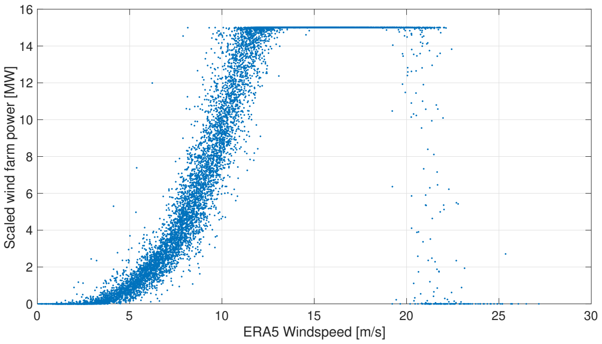

Figure 6.2: The wind farm power production data, scaled to 15 MW, plotted against the ERA5 wind speed at the same time.

The power production data of the wind farm, scaled to the turbine power of 15 MW, is temporally correlated with the ERA5 wind speed data. The resulting plot, illustrating the relationship between the ERA5 wind speed and power production of the wind farm, is presented in Figure 6.2. While the data points exhibit a general trend along a line that reflects the power curve in Figure 2.12, there is a variability or noise present. This misalignment is expected since the ERA5 wind speed data did not perfectly correlate with the thrustless rotor-averaged wind speed from the power data. Notably, around ERA5 wind speeds of 21 m/s, some data points indicate zero power production, while some other data points at the same wind speed indicate maximum power production. These inconsistencies may arise from the averaging process, as the averaging may introduce smoothing effects that remove short-term fluctuations in power generation. Nevertheless, wind speeds surpassing the cut-out wind speed are not common throughout the year, as suggested by the limited number of data points in that range compared to those along the upward trajectory of the wind farm power curve. Therefore, the impact on the total annual power production will be minimal.

The Locally-Weighted Scatterplot Smoothing (LOWESS) function in Python is used to fit a line to the plot, and thus produce a scaled wind farm power curve. The LOWESS function is a non-parametric regression that performs local weighting, meaning that the fit does not adhere to a specific function, but averages local data points. The resulting scaled wind farm power curve is presented in Figure 6.3, plotted alongside the data points. Different LOWESS settings are used for the upward slope (between ERA5 wind speed of 0 and 15 m/s) and the downward slope (between ERA5 wind speed of 15 and 30 m/s) of the wind farm power curve. The LOWESS function uses local points to fit a line and as the upward slope has more data points, the LOWESS function should use more local data points to create a smooth fit. The downward slope does not have a lot of points, as the wind speed does not reach the cut-out wind speed often in the reference year. Therefore, the LOWESS function on the downward slope should use a low amount of data points to create a fit. The 'frac' parameter of LOWESS indicates the fraction of all data points the LOWESS function uses to create the fit and the 'it' parameter reflects the number of residual-based reweightings of the data. The best results are obtained on the upward slope for the settings of frac = 1/11 and it = 5. The best results for the downward slope are obtained using the settings of frac = 1/55 and it = 3.

When comparing the results of Figure 6.3 to the idealised wind turbine power curve of Figure 2.12, the most significant difference is observed in the downward slope of the power curves. In the idealised wind turbine power curve, the power output immediately drops to zero at the cut-out speed. However, the wind farm power output decays more gradually. This difference can be explained by the nature of a wind farm, where different wind turbines can experience different wind speeds. The wind speed can be above the cut-out wind speed for some upwind wind turbines in a wind farm, but will not be above the cut-out wind speed for downwind wind turbines. As the wind speed increases, more wind turbines will reach the cut-out wind speed resulting in a decrease of the average power output of the wind farm.

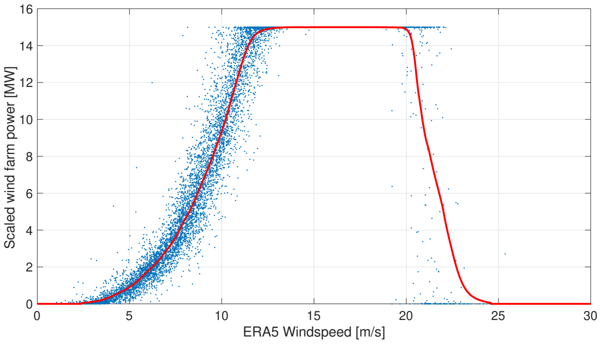

Figure 6.3: The wind farm power curve (in red) for different ERA5 wind speeds in a plot with the data points of the wind farm power, scaled to 15 MW, plotted against the ERA5 wind speed.

The capacity factor of the wind farm can be calculated using Equation 2.35. The capacity factor of the original power data of Baas et al. [2023] is 0.528, which ranks high among wind projects. However, the IEA [2022a] propose that offshore wind projects can reach capacity factors over 50%. Given the use of substantial 15 MW wind turbines, the capacity factor of the original power data seems logical. The wind farm power production for a certain ERA5 wind speed can be calculated through the wind farm power curve. Therefore, the capacity factor can also be calculated starting at the ERA5 wind speed. Applying this method to the same location (IJmuiden Ver) and the same year (2015) results in a capacity factor of 0.528, identical to the original data.

For the determination of the power production for the electrolyser system, the ERA5 wind speed at the centre of Hollandse Kust VI and VII wind farms is used, as discussed in Section 5.1. The coordinates of this location are 52.608 °N and 3.763 °E, approximately 35 km away from the location where the wind power curve is set up. When using the ERA5 wind speed data at Hollandse Kust VI and VII for the same year, the capacity factor falls slightly to 0.518. The wind farms of Hollandse Kust VI and VII are located closer to shore than the IJmuiden Ver wind farm, resulting in a lower average wind speed. This leads to a slight decrease in the capacity factor.

The wind farm power curve allows for the determination of the load delivered to the electrolyser system. It is interesting to view how much load is delivered to the electrolyser during a year. A load duration curve displays the load elements in descending order of magnitude over a certain period. In Figure 6.4, the normalised yearly load duration is depicted for the wind power system using the ERA5 wind speed data. The yearly load duration curve is normalised by averaging the yearly load duration curve over the years in the lifespan of the electrolyser system. Notably, the load duration curve reaches zero at around 8766 hours, which is the average amount of hours during a year when leap years are taken into account. From Figure 6.4 it is evident that there are nearly 2000 full-load hours during a year.

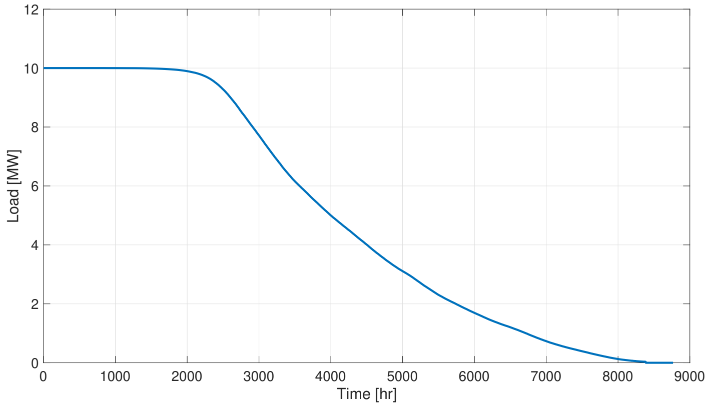

Figure 6.4: The normalised yearly load duration curve of the wind farm for the load delivered to the electrolyser system.

The base case scenario for both the AE and PEM electrolyser systems considers a system lifespan of 25 years, with the sensitivity analysis exploring a range between 20 and 30 years. As detailed in Chapter 5, The ERA5 wind speed data begins in 1993, representing the wind speed in 2027 for the first year of the electrolyser model. Consequently, year 20 and year 30 correspond to the ERA5 wind speed data from 2012 and 2022. Moving forward, the years of ERA5 wind speed data and hydrogen production data will be referenced as year 1, year 2, and so on, to match the timeline of the levelised costs model. The average ERA5 wind speed of year 1 to year 30 is depicted in Figure 6.5, with all years having an average ERA5 wind speed between 8.5 and 10 m/s. The peak ERA5 average wind speed is observed in year 6 at 10.00 m/s, and the lowest in year 18 at 8.51 m/s. Additionally, the mean power output for a 10 MW PPA across all years is determined using the wind farm power curve with all ERA5 data points in those years and is illustrated in red in Figure 6.5. The average power production of a 10 MW PPA varies around 5 MW, which is logical from the capacity factor calculations. As expected, the average power production generally follows the average ERA5 wind speed, as a higher wind speed means more electricity production up to the rated wind speed of the wind turbine.

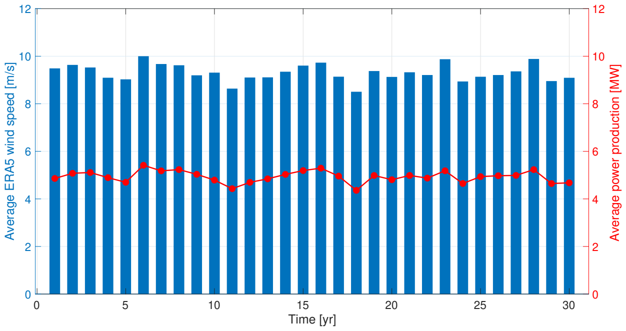

Figure 6.5: A plot of the average horizontal ERA5 wind speed at the Hollandse Kust VI and VII over 30 years. The corresponding average power production in that year is indicated by the points on the red line. The left vertical axis reflects the average ERA5 wind speed, while the right axis reflects the average power production of the wind farm.

6.2. Electrolyser System

In this section, the models for both the AE and PEM electrolyser systems are discussed. Intermediate results for the AE and PEM electrolyser are showcased. The AE and PEM electrolyser systems differ mostly by the input variables of the system design. In modelling, the set-up of the model of the polarization curve and Faraday efficiency differs for the AE and PEM electrolyser stacks, as discussed in Section 3.1 and Section 3.2. The approach of the model for the system performance and simulation of hydrogen and waste heat production is the same for both AE and PEM electrolyser systems.

In this section, first, the model of the electrolyser stacks is discussed, whereafter the model of the system and simulation of the models are discussed. This is followed by figures of the hydrogen and waste heat recovery over the lifetime of the electrolyser.

6.2.1. Model of Electrolyser Stack

The electrolyser facility is modelled by stacks of the same single electrolyser cell. So a single electrolyser cell is modelled and multiplied by the amount of cells to get the installed capacity of the electrolyser facility. To repeat, for modelling the AE and PEM electrolyser stacks, the polarization curve and Faraday efficiency curve are required. The polarization curve is used to determine the voltage efficiency curve by Equation 2.20.

The electrolyser cells of the AE stack will be modelled by the polarization curve of the electrolyser by Sanchez et al. [2018] and the Faraday efficiency by Ulleberg [2003]. To this end, Equation 3.2 and Equation 3.3 are used for the polarization curve and the Faraday efficiency, respectively. The coefficients r_1, r_2, d_1, d_2, s, t_1, t_2 and t_3 for modelling the polarization curve of the alkaline electrolyser are adopted from the alkaline electrolyser of Sanchez et al. [2018]. The coefficients for simulating the Faraday efficiency f_{11}, f_{12}, f_{21} and f_{22} are taken from Ulleberg [2003], and all coefficients are depicted in Table 6.1.

Table 6.1: The coefficients for modelling the polarization curve and the Faraday efficiency of an AE cell. The values for the coefficients are taken from the studies by Sanchez et al. [2018] and Ulleberg [2003].

Coefficient	**Value**
r_1	$4.45153 \cdot 10^{-5}$ Ω m^2
r_2	$6.88874 \cdot 10^{-9}$ Ω m^2 °C^{-1}
d_1	$-3.12996 \cdot 10^{-6}$ Ω m^2
d_2	$4.47137 \cdot 10^{-7}$ Ω m^2 bar^{-1}
s	0.33824 V
t_1	-0.01539 m^2 A^{-1}
t_2	2.00181 m^2 °C A^{-1}
t_3	15.24178 m^2 °C^2 A^{-1}
f_{11}	478645.74 A^2 m^{-4}
f_{12}	-2953.15 A^2 m^{-4} °C^{-1}
f_{21}	1.03960
f_{22}	-0.00104 °C^{-1}

As discussed in Section 3.2, the stacks of the PEM electrolyser will be modelled by the empirical equations for the polarization curve, and using the model of Yodwong et al. [2020] for the Faraday efficiency. For the set-up of the polarization curve, the Nernst potential, and activation and ohmic overpotential are implemented in the formula for the cell potential (Equation 2.8).

For the determination of the Tafel equations of Equation 3.5 and Equation 3.6, values for the charge transfer coefficients, exchange current density, reference temperature, and activation energy are taken from literature. The charge transfer coefficients of the anode α_a and cathode α_c of PEM electrolyser cells are assumed to be equal to 0.5, as the reaction tends to symmetry [Falcao and Pinto, 2020; Dale et al., 2008]. The exchange current density of the anode $i_{0,a}$ is generally much lower than the exchange current density of the cathode $i_{0,c}$ [Falcao and Pinto, 2020; Garcia-Valverde et al., 2012]. In literature, values for the anode are reported between $1 \cdot 10^{-6}$ to $1 \cdot 10^{-9}$ and between $1.5 \cdot 10^{-1}$ and $2 \cdot 10^{-3}$ for the cathode [Falcao and Pinto, 2020; Carmo et al., 2013]. The values depend on the electrolyser design and operating conditions, like temperature and pressure. As the empirical equations do not depend on the pressure, the values for the exchange current density are chosen from literature based on a PEM electrolyser operated around 30 bar. In this thesis, the reference exchange current density of the anode $i_{0,a,ref}$ and cathode $i_{0,c,ref}$ are set to $1.0 \cdot 10^{-7}$ A cm^{-2} and $1.0 \cdot 10^{-3}$ A cm^{-2}, based on Tijani et al. [2018] and Abdin et al. [2015]. Following these studies, the reference temperature for both the anode $T_{a,ref}$ and cathode $T_{c,ref}$ is set at 318 K. For the activation energy of the OER at the anode $E_{act,a}$, a value of 65 kJ/mol is set, following the results of Suermann et al. [2018]. The activation energy of the HER at the cathode is set at 40 kJ/mol, based on the study of Siracusano et al. [2015].

For the model of Yodwong et al. [2020] for the Faraday efficiency (Equation 3.16), values for the coefficients a_1, a_2, b and c are mentioned in the corresponding study. However, when plotting these values, the resulting Faraday curve differs from the one in the study of Yodwong et al. [2020]. Therefore, the coefficients were recalculated based on the data from Yodwong et al. [2020]. This resulted in a value for a_1 of -0.6778 A m^{-2} bar^{-1}, a value for a_2 of -0.3342 A m^{-2}, a value for b of -1, and a value for c of 1. The values for all parameters are depicted in Table 6.2.

Table 6.2: The coefficients for modelling the polarization curve and the Faraday efficiency of a PEM electrolyser. The determination of the values is explained in the text.

Coefficient	**Value**
α_a	0.5
α_c	0.5
$i_{0,a,ref}$	$1.0 \cdot 10^{-7}$ A cm^{-2}
$i_{0,c,ref}$	$1.0 \cdot 10^{-3}$ A cm^{-2}
$T_{a,ref}$	318 K
$T_{c,ref}$	318 K
$E_{act,a}$	65 kJ mol^{-1}
$E_{act,c}$	30,000 J mol^{-1}
a_1	-0.6778 A m^{-2} bar^{-1}
a_2	-0.3342 A m^{-2}
b	-1
c	1

The resulting polarization curves for the AE and PEM electrolyser cells are depicted in Figure 6.6. The polarization curves have the same shape but the cell potential of the AE cell is going up much faster at increasing current density. This is in agreement with what is expected as the operational current density of PEM electrolyser cells is around 2 to 3 A/cm^2, while the operational current density of an AE cell is around 0.2 to 0.7 A/cm^2 [Hancke et al., 2022]. The cell potential at a current density of 0 A/cm^2 is characterized by the reversible cell potential U_{rev}. The polarization curve of the AE cell starts at a higher cell potential (around 1.2 V) than the polarization curve of the PEM electrolyser cell (around 1.25 V). This is a direct result of the dependency of the Nernst equation (Equation 2.6 and Equation 2.7) on the operating pressure. So, the dependency of the polarization curve on the operating pressure is shown through the Nernst potential. An increase in the operating pressure will increase the Nernst potential and a decrease in the operating pressure will decrease the Nernst potential.

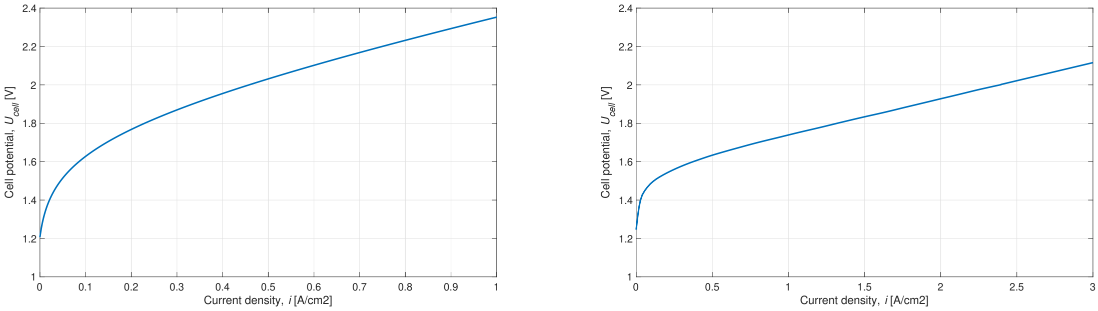

(a) The polarization curve of the AE cell, which is modelled by employing the semi-empirical model by Sanchez et al. [2018].

(b) The polarization curve of the PEM electrolyser cell, which is modelled using the empirical approach by Falcao and Pinto [2020].

Figure 6.6: The polarization curves for the AE and PEM electrolyser cells.

The voltage efficiency and Faraday efficiency of the AE and PEM electrolyser cells are depicted in Figure 6.7. In both figures, the voltage efficiency surpasses 1 at low current densities. At low current densities, until around 0.05 A/cm^2, the polarization curve is below the thermoneutral potential (which is 1.473 V at 80 °C). For those current densities, the production of heat due to the overvoltages is not enough to supply the energy needed for supplying the entropic term $T\Delta S$. Therefore, heat is extracted from the environment at these low current densities. Since the voltage efficiency is a direct representation of the relation between the cell potential and the thermoneutral potential U_{tn}, the voltage efficiency is higher than 1. The Faraday efficiency of the AE cell in Figure 6.7a is generally lower than the Faraday efficiency of the PEM electrolyser cell in Figure 6.7b. At higher current densities, for example, at 1 A/cm^2, the Faraday efficiency of the PEM electrolyser is very close to 1 while the Faraday efficiency of the AE is around 0.95. Both observations are a direct result of more gas crossover in the AE cell, as discussed in Section 2.2.2. Gas crossover is viewed as a loss of current as the electrons are not used for hydrogen that ends up in the product stream.

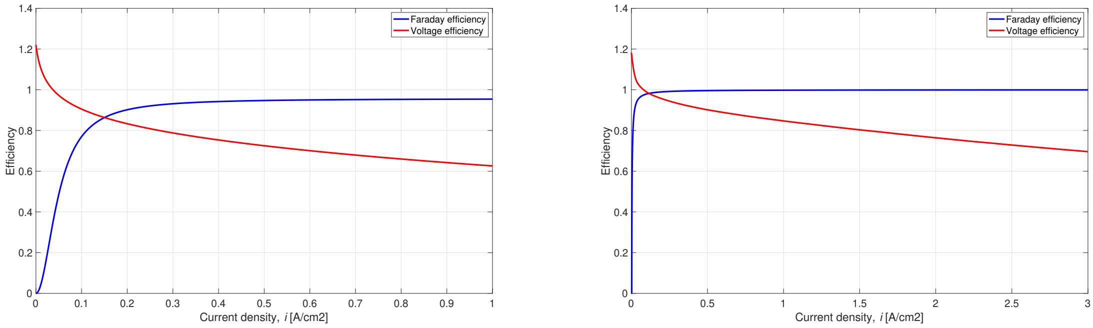

(a) AE cell **(b)** PEM electrolyser cell

Figure 6.7: The voltage and Faraday efficiency curves of the AE and PEM electrolyser cells, plotted over different current density ranges.

As explained in Section 2.2.1, the full-load point of the electrolyser can be chosen arbitrarily by an electrolyser manufacturer. The polarization curve is related to the power that is used by the electrolyser, as power is the current multiplied by the cell voltage. These parameters are displayed on the axis of the polarization curve. Choosing a high full-load point results in a higher power density and more hydrogen production per electrolyser cell, thus a more compact electrolyser design. However, as the voltage increases, the voltage efficiency will decrease and thus a higher electricity use per kg of hydrogen is attained. There currently is no established or industry-standard method for specifying the full-load point of an electrolyser.

In this thesis, the full-load point is determined by setting the electrolyser stack efficiency at the start of life equal to a literature-backed full-load start-of-life stack efficiency $\eta_{stack,SoL}$, as discussed in Section 5.2.

$$\eta_{cell,SoL} = \eta_f \eta_v \eta_{deg} = \eta_f \eta_v \tag{6.2}$$

As the degradation efficiency is 1 at the start of life, it can be omitted from the equation. By plotting the full-load start-of-life stack efficiency $\eta_{stack,SoL}$ for a range of current densities, the current density at the projected $\eta_{stack,SoL,FL}$ can be determined. The value at this current density reflects the current density at full-load i_{FL}. By using the polarization curve, the corresponding full-load cell potential $U_{cell,FL}$ at the full-load current density can be determined.

In Figure 6.8, the start-of-life stack efficiency $\eta_{stack,SoL}$ is plotted next to its building blocks, the Faraday and voltage efficiency. Additionally, the horizontal black lines indicate the selected start-of-life full-load stack efficiencies $\eta_{stack,SoL,FL}$, as drafted in the system design as 0.7 and 0.75 for the AE and PEM electrolyser stack respectively. The full-load current density i_{FL} of the AE cell is 0.442 A/cm^2 when examining the second intersection of the start-of-life stack efficiency with the full-load start-of-life stack efficiency. Utilising the same approach, the full-load current density i_{FL} of the PEM cell is 2.181 A/cm^2. These values agree with the current densities reported in literature. Using the full-load current density i_{FL} in the plots for the polarization curves of Figure 6.6, the full-load cell potential $U_{cell,FL}$ for the AE and PEM electrolyser stack is determined at 1.99 V and 1.96 V. The full-load potential of the AE stack is higher since the start-of-life full-load cell efficiency for the AE stack is set lower than for the PEM electrolyser stack.

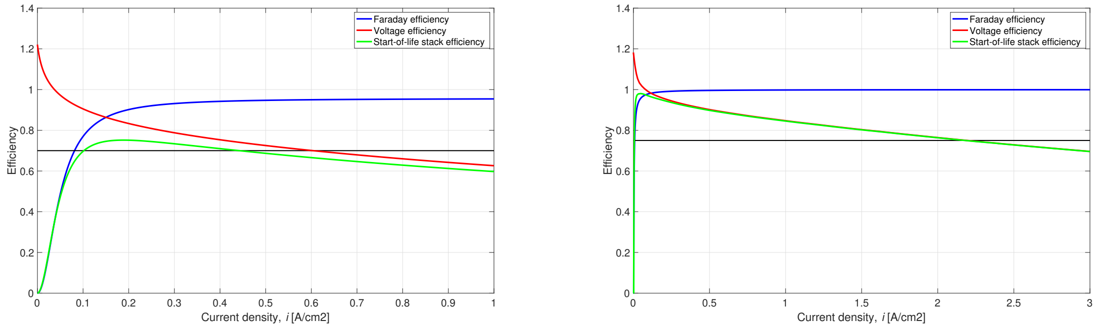

(a) AE cell

(b) PEM electrolyser cell

Figure 6.8: The Faraday, voltage efficiency and start-of-life stack efficiency curves for both the AE and PEM electrolyser cells. The horizontal black lines indicate the selected start-of-life full-load stack efficiencies $\eta_{stack,SoL,FL}$, which are used to determine the full-load point of the electrolyser.

The power used at full-load by a single electrolyser cell can be determined by using Equation 2.9 and Equation 2.10. Based on the full-load point and the area of the cell A_{cell}, the full-load power of respectively a single AE and a PEM electrolyser cell are determined to be 26.4 and 21.4 kW for the base case system design. The partial load curve can be derived by relating the full-load power point to partial load points. The partial load curve indicates the electrolyser efficiency for all load ratios over the electrolyser. A load ratio of 1 indicates full-load, while a load ratio of 0.2 indicates an applied power over the electrolyser of 20% of the full-load power. The partial load curves are important for the simulation of the stacks for different amounts of electricity produced, given the intermittent electricity generation of the wind farm. The start-of-life partial load curves for the AE and PEM electrolyser cells are depicted in Figure 6.9. As one can see, the start-of-life cell efficiency $\eta_{cell,SoL}$ of the PEM electrolyser is higher at all load ratios. This result agrees with literature, where a higher partial load curve is mentioned as an advantage of a PEM electrolyser cell over an AE cell [Salehmin et al., 2022].

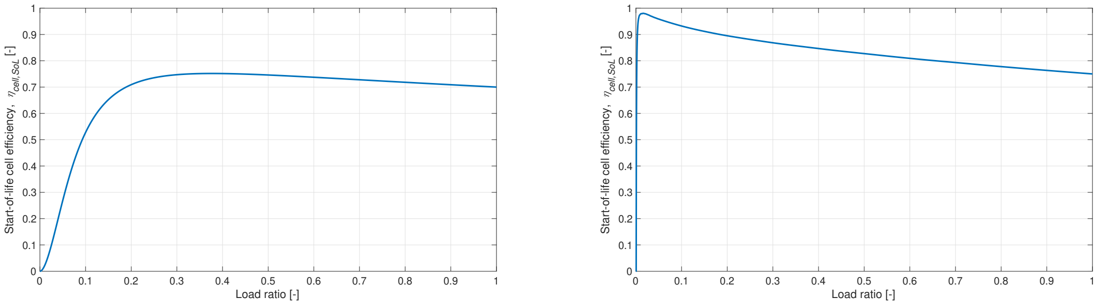

(a) AE cell

(b) PEM electrolyser cell

Figure 6.9: The partial load curves of the AE and PEM electrolyser cells, which result from determining the full-load point.

Up till now, degradation has not been included in the analysis. Degradation is normally viewed as an increase of the overvoltage of the polarization curve for every hour the electrolyser cell is operational. If the degradation is modelled following this approach, the polarization curve and the full-load point have to be determined for every time point the electrolyser is operational. To save computational power, the polarization curve is expected to stay constant and the degradation efficiency η_{deg} is introduced. The degradation efficiency decreases at a constant rate for every hour the electrolyser is switched on. The degradation efficiency decreases the production of hydrogen, while it results in an increase of heat production through Equation 2.30. As a result from Equation 2.18, the partial load curve of the electrolyser cell reduces according to the number of hours the electrolyser cell is operational. The partial load curves of the AE and PEM electrolyser cell at the end-of-life are depicted in Figure 6.10, accompanied by the start-of-life partial load curves. The partial load at the end-of-life is calculated using the stack lifetime t_{stack} while the difference between the start-of-life and end-of-life partial load curves is the result of the degradation efficiency η_{deg}. The degradation efficiency of the AE cell at the end-of-life is 91.6%, which results in an end-of-life full-load cell efficiency of 64.1%. Accordingly, the degradation efficiency of the PEM electrolyser cell at the end-of-life is 92.8%, which results in an end-of-life full-load cell efficiency of 69.6%.

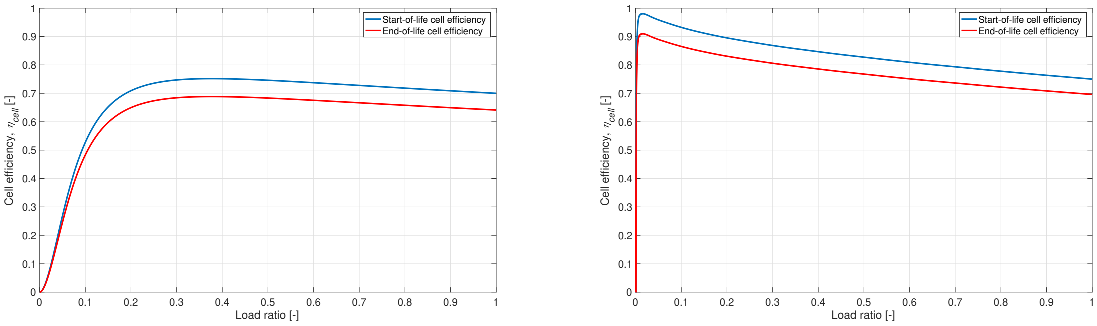

(a) AE cell

(b) PEM electrolyser cell

Figure 6.10: The start-of-life and end-of-life cell efficiency curves for the AE and PEM electrolyser cells. The end-of-life cell efficiency curves are determined by implementing the maximum amount of degradation.

Next, the recovery of waste heat can be incorporated into the electrolyser cell efficiency by adding the term for the recovery of heat, as in Equation 2.23. It is important to note that the thermal efficiency η_{th} of a PEM electrolyser cell is assumed to be 0.9, while the thermal efficiency of an AE cell is assumed to be 0.875. The electrolyser efficiency depends on the number of hours the electrolyser cell has been operational to that point. Both the start-of-life $\eta_{cell,heat,SoL}$ and end-of-life cell efficiency $\eta_{cell,heat,EoL}$ with heat recovery for the AE and PEM electrolyser cell are shown in Figure 6.11. For comparative purposes, the efficiencies of the cells without heat recovery are also presented in this figure.

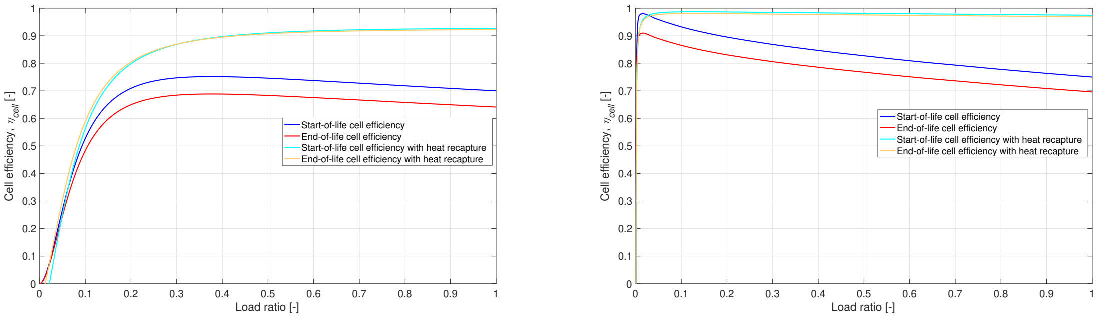

(a) AE cell

(b) PEM electrolyser cell

Figure 6.11: The start-of-life and end-of-life cell efficiency curves for the AE and PEM electrolyser cells with and without waste heat recovery.

For the AE cell-cell in Figure 6.11a, three things stand out. Firstly, the start-of-life and end-of-life cell efficiency peaks at full-load. This is a logical result as the Faraday efficiency of the AE cell increases over the whole load ratio, which can be seen in Figure 6.7a. Losses from the Faraday efficiency are not recovered, while losses from the voltage efficiency are recovered for 87.5% in the form of heat. The increase in the Faraday efficiency exceeds 12.5% of the losses following the descending voltage efficiency. Secondly, the start-of-life heat-recovery cell efficiency is higher than the end-of-life heat-recovery cell efficiency at high load ratios, but the opposite is true for lower load ratios. Because of the way the equations for heat recovery are set up, the start-of-life heat-recovery cell efficiency and end-of-life heat-recovery cell efficiency are equal when the Faraday efficiency equals the thermal efficiency (which is around a load ratio of 0.316). This can be explained by rewriting Equation 2.23 to

$$\eta_{cell,heat} = \eta_f \eta_v \eta_{deg} + \eta_{th} \cdot \left(1 - \eta_v \eta_{deg}\right) = \eta_{th} + \eta_v \eta_{deg} \left(\eta_f - \eta_{th}\right) \tag{6.3}$$

Now, it is easy to see that the heat-recovery cell efficiency at the start-of-life and end-of-life are equal when the Faraday efficiency is equal to the thermal efficiency. When the Faraday efficiency is higher than the thermal efficiency, the start-of-life heat-recovery cell efficiency will be higher than the end-of-life heat-recovery cell efficiency. The opposite is true if the Faraday efficiency is lower than the thermal efficiency. Thirdly, the heat-recovery cell efficiency is lower than the general cell efficiency at very low load ratios, around 0.03. This is the result of the voltage efficiency being greater than 1. As a result, the reaction needs extra heat, so heat is used instead of generated, lowering the overall cell efficiency when including heat ’recovery’. As is discussed in Section 5.2, the load range of the AE cell is set from 0.15 to 1, so this phenomenon does not have to be accounted for because the cell is switched off at these specific load ratios.

The last two points are the same for the heat-recovery efficiencies of PEM electrolyser cells, but the Faraday efficiency increases so fast at a low load ratio that these phenomena are hardly visible in Figure 6.11b. To address the first point, the start-of-life and end-of-life heat-recovery cell efficiency for the PEM electrolyser cell peaks around a load ratio of 0.2. Above that load ratio, the start-of-life and end-of-life heat recovery cell efficiency decreases gradually until full-load. As depicted in Figure 6.7b, the Faraday efficiency of the PEM electrolyser cell remains almost constant beyond 0.5 A/cm^2. Therefore, above a load ratio of 0.2, the only change in the cell efficiency is due to the decrease in voltage efficiency. Consequently, the heat-recovery cell efficiency decreases, but more slowly compared to the cell efficiency without heat recovery since a large part of the losses are recovered in heat.

Generally speaking, the cell efficiency increases when taking into account the recovery of heat. The degree of the increase depends on the load ratio. For the AE cell, the maximum heat-recovery cell efficiency for start-of-life and end-of-life are 92.7% and 92.2%, respectively. These results indicate an increase of 22.7% and 28.1% compared to the cell efficiency without heat recovery, respectively. Accordingly, the maximum heat recovery cell efficiency for start-of-life and end-of-life are 98.7% and 98.1% for a PEM cell. These results indicate an increase of 22.4% and 27.3% compared to the cell efficiency without heat recovery, respectively.

6.2.2. Model of Electrolyser System

The model of the electrolyser stack forms the basis of the model of the electrolyser system. For the model of the electrolyser system, the electricity usage of the BoP and the compressor is added to the stack efficiency. The electricity usage of the BoP and compressor is modelled as a loss through the BoP efficiency η_{BoP} and compressor efficiency η_{comp}. The resulting system efficiency for heat recovery and without heat recovery is given by Equation 2.26 and Equation 2.27. Both the BoP efficiency η_{BoP} and compressor efficiency η_{comp} are viewed as a constant efficiency over the load ratio. This means that they use the same ratio of power at all load ratios. The resulting figures for the start-of-life and end-of-life electrolyser system efficiency with and without heat recovery are depicted in Figure 6.12. It is important to note that the start-of-life and end-of-life efficiencies indicate the start and end of the lifetime of the stack, not of the system lifespan. The general shapes of the curves of the system efficiencies align closely to the shapes in Figure 6.11, but the curves are shifted downward to account for the supplementary equipment of the electrolyser system. The full-load start-of-life and end-of-life system efficiencies of the AE system, without heat recovery, are 63.0% and 57.7%. The increased full-load heat-recovery start-of-life and end-of-life system efficiencies of the AE system are 83.4% and 83.0%, respectively. This means an increase of the full-load cell efficiency of respectively 20.4% and 25.3% when recovering waste heat. Accordingly, The full-load (no heat recovery) start-of-life and end-of-life system efficiencies of the PEM electrolyser system were 69.0% and 64.0%, respectively. The full-load heat-recovery start-of-life and end-of-life system efficiencies of the PEM electrolyser system are 89.6% and 89.1%, respectively, indicating an increase of 20.6% and 25.1%. The increase in system efficiency is more pronounced at the end-of-life since more heat is produced, which was previously lost in the systems without heat recovery.

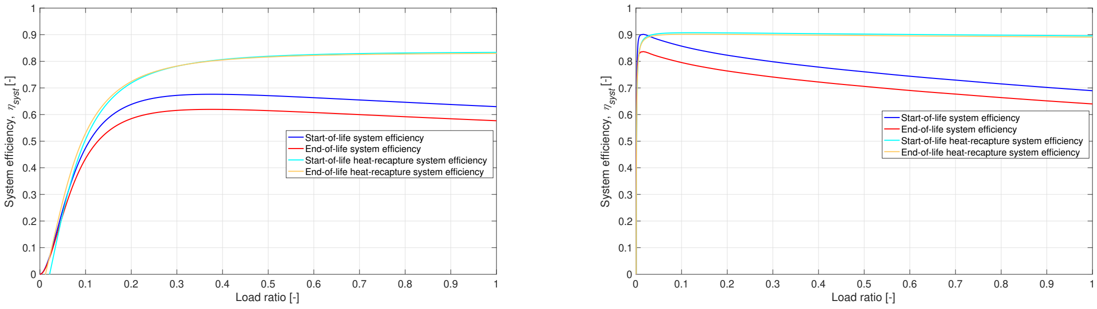

(a) AE system

(b) PEM electrolyser system

Figure 6.12: The start-of-life and end-of-life system efficiency curves for the AE and PEM electrolyser systems with and without waste heat recovery.

Using the system efficiency and the power supplied by the PPA, the power that is directly used for hydrogen production (which ends up as chemical energy in hydrogen molecules) is given by

$$P_{H_2} = P_{PPA}\eta_{suppl}\eta_{stack} = P_{grid}\eta_f\eta_v\eta_{deg}\eta_{BoP}\eta_{comp} \tag{6.4}$$

which is based on Equation 2.28, but used for the power P_{PPA} that is produced and delivered to the grid according to the PPA. Next, the mass production flow of hydrogen per hour $\dot{m}_{H_2}$ can be determined using Equation 2.29.

Accordingly, the amount of heat that is recovered from the system at a certain power delivered to the electrolyser P_{PPA} is calculated by

$$P_{heat} = P_{PPA}\eta_{suppl}\eta_{th} \cdot \left(1 - \eta_v\eta_{deg}\right) \tag{6.5}$$

Using the mentioned formulas, the hydrogen production and heat production over the entire lifetime of the electrolyser system can be simulated. These results are the basis for the levelised cost analyses. The hydrogen production and heat recovery at the start-of-life and at the end-of-life at all PPA powers P_{PPA} are depicted in Figure 6.13. One can see in these figures that the maximum amount of hydrogen is produced at the start-of-life, while the maximum amount of heat is produced at the end-of-life. These results are very logical because of the degradation of the electrolyser stack. The highest production of hydrogen for the AE and PEM systems are 159.8 kg/h and 175.6 kg/h, respectively. These values are close to the maximum hydrogen production of 181.3 kg/h in the study by Villarreal Vives et al. [2023] on the LCoH$_2$ of a 10 MW PEM electrolyser system. The 'dip' in the production of hydrogen and heat of the AE system at low PPA powers P_{PPA} from 0 to around 0.5 MW in Figure 6.13a is a result of the slowly rising system efficiency in Figure 6.12a, which leads back to the slowly rising Faraday efficiency in Figure 6.7a. When comparing Figure 6.13a and Figure 6.13b, the hydrogen production at full-load is higher for the PEM electrolyser system than the AE system, at both start-of-life and end-of-life. This is the result of the full-load start-of-life cell efficiency $\eta_{cell,SoL,FL}$ being set higher for the PEM electrolyser at 75% compared to 70% for the AE electrolyser cell. The full-load heat recovery of the AE and PEM electrolyser systems are almost identical. While the AE system produces more heat, the thermal efficiency η_{th} of the PEM system is higher, which balance each other out. The full-load end-of-life heat production of the AE system is 2.53 MW, which equals the end-of-life increase of the full-load system efficiency of 25.3%. The same holds for the PEM electrolyser system at 2.51 MW and 25.1%.

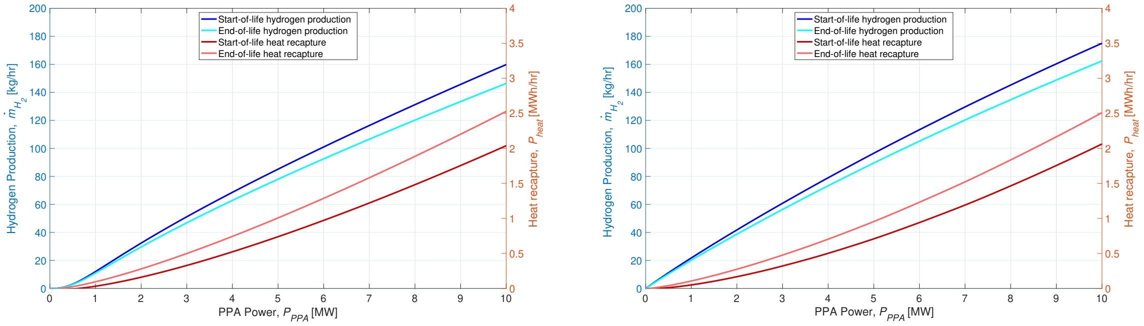

(a) AE system **(b)** PEM electrolyser system

Figure 6.13: The start-of-life and end-of-life hydrogen production and heat recovery of the AE and PEM electrolyser systems as a function of the electricity via the PPA P_{PPA} supplied to the electrolyser. The left vertical axis reflects the hydrogen production, while the right axis reflects the recovered heat.

6.3. Levelised Costs System

The levelised costs system covers the calculation of the LCoH$_2$ and LCoH$_{\text{eat}}$. This economic model is set up in an interactive Excel document, employing Equation 2.36 and Equation 2.41. The hydrogen production and heat production per year are calculated using the electrolyser model and loaded into the levelised costs model. Additionally, the economic parameters for the electrolyser system of Table 5.4 are used as input. The results of the levelised costs model are discussed in the next chapter. The results of the levelised costs model for the LCoH$_2$ and LCoH$_{\text{eat}}$, including sensitivity analysis, can be used to determine the economic feasibility of the project.

7

Results

This chapter presents the results obtained from the model presented in the previous chapter, which is applied to the case study in the Zuidplas region. The results of the hydrogen and heat production are based on the values selected in the system design in Chapter 5. The values of the LCoH$_2$ and LCoH$_{eat}$, calculated from the system design, are referred to as the base case. The sensitivity analysis shows the effect of deviations of the base case on the corresponding LCoH$_2$ and LCoH$_{eat}$. In this way, the sensitivity analysis indicates the influence of a certain parameter on the LCoH$_2$ and LCoH$_{eat}$.

The results on the total hydrogen production and heat recovery are presented in Section 7.1. Subsequently, the results for the LCoH$_2$ and LCoH$_{eat}$ are presented in Section 7.2 and Section 7.3.

7.1. Hydrogen Production and Heat Recovery

This section covers the production of hydrogen and heat recovery, using the ERA5 wind speed data as input. The average ERA5 wind speed over all the years is depicted in Figure 6.5.

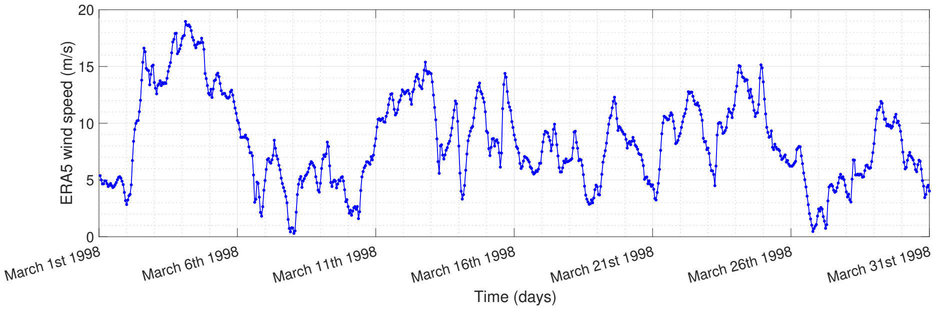

(a) Time series of the ERA5 wind speed data

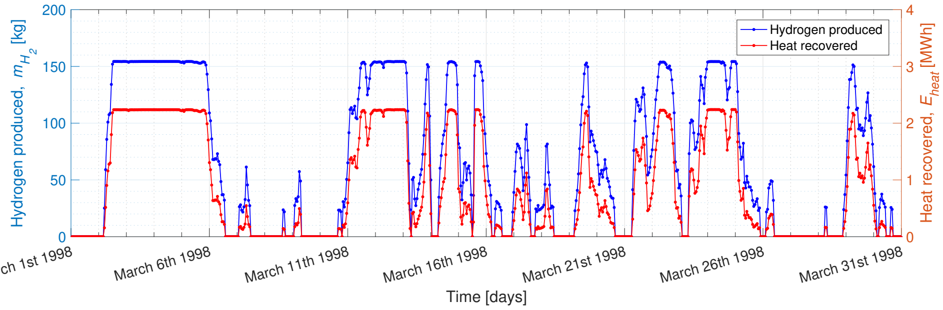

(b) Time series of the hydrogen production and heat recovery of the AE system

Figure 7.1: A part of the time series of the ERA5 wind speed data and the corresponding hydrogen production and heat recovery of the AE system during March 1998. Every dot indicates the wind speed at an hour, and the hydrogen production and heat recovery during that hour.

For a clearer understanding of the time series of the data used in this thesis, a certain month of the time series is depicted in Figure 7.1. In this figure, both the ERA5 wind speed and the corresponding hydrogen production and heat recovery of the AE system are showcased. The most significant variation in ERA5 wind speed between two consecutive time points is roughly 3 m/s, observed around March 23rd. As one can see, the hydrogen production and heat recovery mostly follow the ERA5 wind speed. In the period around the fourth of March 1998, the ERA5 wind speed changed slightly. However, since the wind speed is above the rated wind speed of the wind farm power curve, the hydrogen production and heat recovery remained constant and at full-load. The full-load hydrogen production at this point is between the start-of-life and end-of-life full-load hydrogen production of Figure 6.13a since some degradation of the electrolyser cells has occurred.

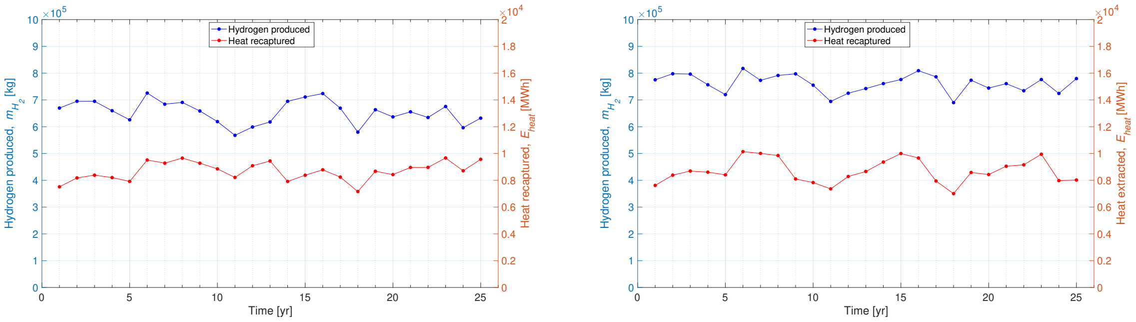

(a) AE system

(b) PEM electrolyser system

Figure 7.2: The hydrogen produced and waste heat recovered during the total system lifespan $_{system}$ of the AE and PEM electrolyser system. The values for the hydrogen production and heat recovery of the AE and PEM systems can be directly compared as the figures are aligned and have the same axes. The left vertical axis reflects the hydrogen production, while the right axis reflects the recovered waste heat.

The amount of green hydrogen produced and delivered to a hydrogen refuelling station over the system lifespan using the electrolyser system is depicted in Figure 7.2 for both the AE and PEM electrolyser system. Moreover, the heat that is recovered in the same years is plotted in the figures. It is important to mention that the same amount of power is supplied to both the simulation of the AE and PEM electrolyser systems, as it is based on the same ERA5 wind speed data. As one can see, the hydrogen production of the PEM electrolyser system is higher than the production of the AE system in the same year. This is logical as the hydrogen production over the PPA power P_{PPA} of Figure 6.13 is higher for the PEM electrolyser system than for the AE system since the overall system efficiency is higher.

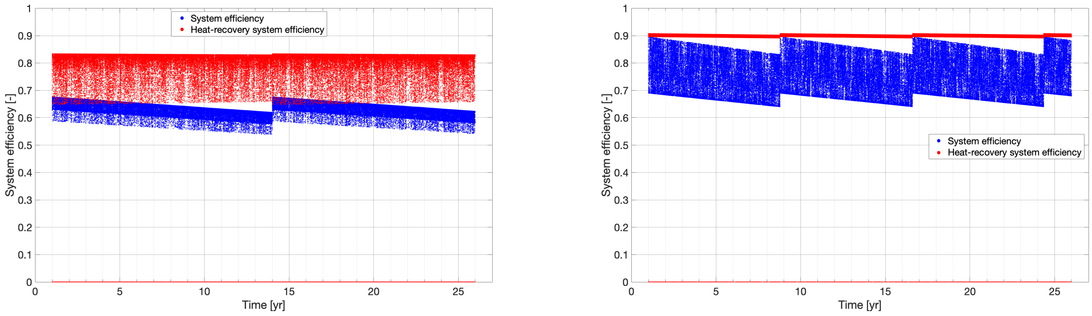

(a) AE system

(b) PEM electrolyser system

Figure 7.3: The system efficiencies of the AE and PEM electrolyser systems including and excluding the waste heat recovery. Stack replacements can be identified by the abrupt changes in system efficiency.

The amount of recovered waste heat is comparable for the AE and PEM electrolyser system, which was also a result of Figure 6.13. In this figure, the stack replacements can be identified, as the hydrogen production increases and the heat recovery decreases in the year of a stack replacement. For example, in year 16 of the PEM electrolyser of Figure 7.2b, the hydrogen production increases compared to the previous year, while the heat recovery decreases. The same holds for year 14 of the AE electrolyser. The stack replacements can be identified when plotting the system efficiency of the electrolyser system over the whole lifespan of the system. In Figure 7.3, the system efficiency including and excluding heat-recovery are depicted during the lifespan of the

AE and PEM electrolyser system, a data point for every hour during the system's lifespan of 25 years. When the data points are close together they can resemble an area. The system efficiencies in Figure 7.3 reflect the range of system efficiencies of Figure 6.12 that are allowed by the load flexibility of the AE and PEM system. This reasoning explains why the range of the heat-recovery system efficiency of the PEM electrolyser system is so narrow. The linear degradation of the system efficiency over time due to the cell degradation is nicely visible. For the time on the x-axis, the year between 1 and 2 is seen as year 1. Accordingly, the year between 25 and 26 is perceived as year 25. Therefore, the graphs start at year 1 and end at year 26. The stack replacements are indicated by the abrupt shifts in system efficiency. For the AE, there is 1 stack replacement at the beginning of year 14, while there are 3 stack replacements for the PEM electrolyser, namely in years 8, 16 and 24. The PEM electrolyser has more stack replacements because the stack lifetime is lower and the load flexibility is higher. The AE electrolyser is switched off for loads below 15% of the installed capacity, which decreases the number of operational hours.

7.2. Levelised Cost of Hydrogen

In this section, the results for the LCoH$_2$ are presented and discussed. The LCoH$_2$ is calculated using Equation 2.36 based on the data and system design as discussed in this thesis. The LCoH$_2$ of the base case for the AE electrolyser system is 6.08 €/kg. The LCoH$_2$ for the base case of the PEM electrolyser system is 5.59 €/kg. The breakdown and contributions to the LCoH$_2$ are indicated in Figure 7.4. The total discounted expenditures for the PEM electrolyser system are higher compared to the AE system, as the CAPEX of PEM is higher. However, more hydrogen is produced during the lifespan of the PEM electrolyser and as a result, the LCoH$_2$ is lower. For both the AE and PEM electrolyser systems, the electricity used by the electrolyser is by far the largest contributing factor. The percentage of direct electricity use to the total LCoH$_2$ is lower for PEM as the CAPEX of PEM is a higher contributing factor. The electricity used by the BoP and compressor is also a reasonable contributor to the LCoH$_2$. The total contribution of the electricity to the LCoH$_2$ is respectively 75.8% and 71.5% for the AE and PEM electrolyser system. The electricity is delivered via a PPA, so the PPA price Π_{PPA} is expected to influence the LCoH$_2$ a lot in the sensitivity analysis. Regarding the compressor, the installed capacity of the compressor of the AE system is larger as more compression is required, and thus are both the CAPEX and electricity use of the compressor higher in the AE system. The remaining costs consist of the electrolyser system DECEX, the compressor DECEX and the compressor OPEX. All the contributions to the LCoH$_2$ of these expenditures are very low.

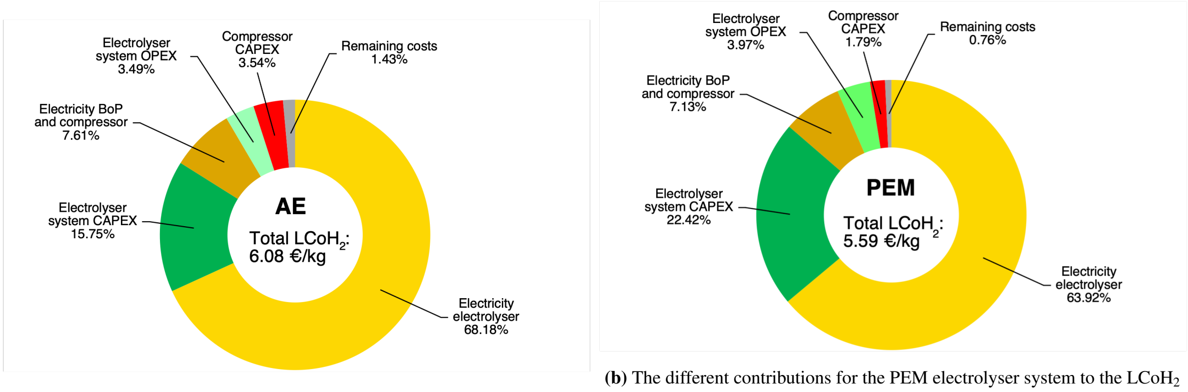

(a) The different contributions for the AE system to the LCoH$_2$ of 6.08 €/kg.

(b) The different contributions for the PEM electrolyser system to the LCoH$_2$ of 5.59 €/kg.

Figure 7.4: The contributions of different expenses to the LCoH$_2$ of the AE and PEM electrolyser systems. The contributions sum to 1 in both figures.

7.2.1. System Design Parameters

The sensitivity analysis of the LCoH$_2$ performed on the design parameters of the electrolyser is discussed first, followed by the sensitivity analysis on the economic design parameters. The sensitivity analysis on the system design parameters of the AE and PEM electrolyser system are depicted in Figure 7.5 and Figure 7.6, respectively. As one can see in the figure is that the installed plant capacity P_{instal} does not influence the LCoH$_2$. This is logical because both the production of hydrogen and the CAPEX and OPEX of the electrolyser system depend linearly on the installed plant capacity. An increase in the installed plant capacity raises hydrogen production and costs by the same ratio. This result verifies the system as it shows that the CAPEX and OPEX of the electrolyser depend linearly on the installed plant capacity. In practice, the CAPEX and of the electrolyser system would depend non-linearly on the installed plant capacity, due to economies of scale. Therefore, an increase in the installed capacity would decrease the LCoH$_2$.

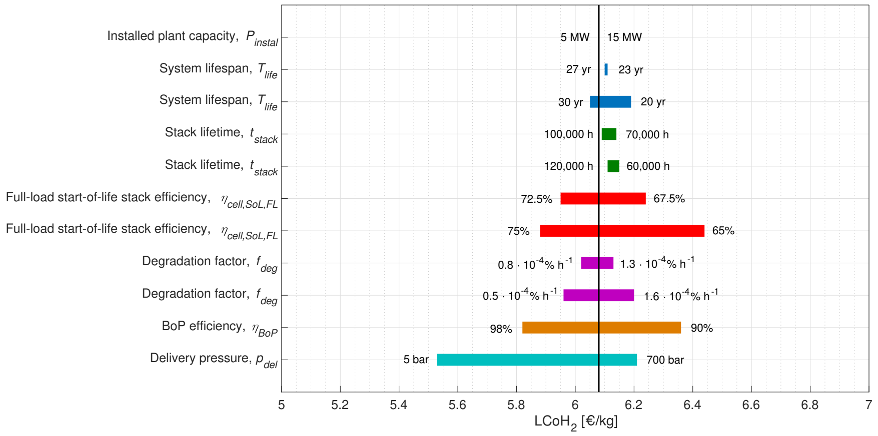

Figure 7.5: The sensitivity analysis for the LCoH$_2$ on the system design parameters of the AE system. The black vertical line indicates the LCoH$_2$ of the base case, which is 6.08 €/kg for the AE system.

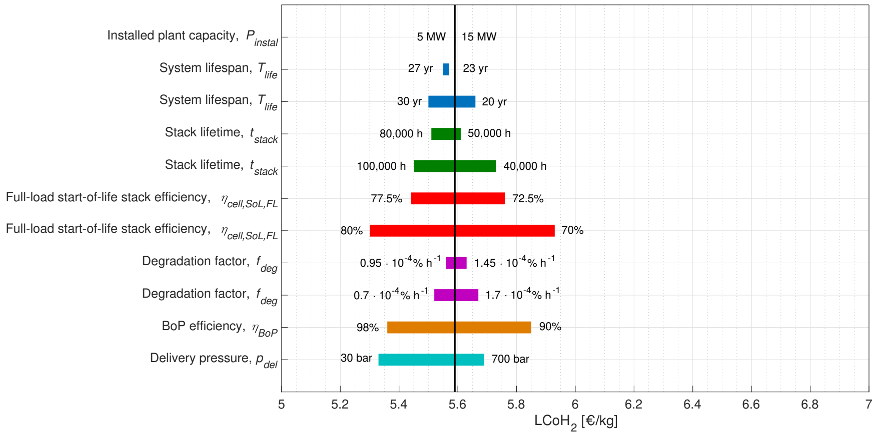

Figure 7.6: The sensitivity analysis for the LCoH$_2$ on the system design parameters of the PEM electrolyser system. The black vertical line indicates the LCoH$_2$ of the base case, which is 5.59 €/kg for the PEM electrolyser system.

The system lifespan T_{system} and stack lifetime t_{stack} have fluctuating effects on the LCoH$_2$, which can be explained by the stack replacements. In general, a longer system lifespan would decrease the LCoH$_2$ and a shorter system lifespan would increase the LCoH$_2$. The opposite happens in the results of the sensitivity analysis of the AE system for a lifespan of 27 years. An additional stack replacement in year 26 increases the LCoH$_2$. The same happens at a lifespan of 23 years of the PEM electrolyser system, which omits the stack replacement in year 24. As a result, the LCoH$_2$ is lower for a system lifespan of 23 years compared to the base case of 25 years.

The stack lifetime t_{stack} has a larger influence on the PEM electrolyser system compared to the AE system. The PEM electrolyser has more stack replacements during the system lifespan and is, therefore, more dependent on fluctuations in the stack lifetime. A longer lifetime will decrease the amount of stack replacements, thus lowering the LCoH$_2$. For the AE system, one can see that an increase or decrease of the stack lifetime increases the LCoH$_2$, both can be explained when analysing the stack replacements. The AE system has only one stack replacement in year 14 and would have a second stack replacement in year 26. A decrease in the stack lifetime would result in the second stack replacement occurring within the system lifespan of 25 years. An increase in the stack lifetime would mean that the first stack replacement would happen later. Therefore, the first stack would degrade further by the same degradation factor, thus producing less hydrogen compared to a new stack. The lower hydrogen production numbers of hydrogen increase the $LCoH_2$.

The full-load start-of-life stack efficiency $\eta_{cell,SoL,FL}$ has a big influence on the $LCoH_2$ for both the AE and PEM electrolyser system. The full-load start-of-life stack efficiency determines the operating point as explained in Section 6.2. Therefore, the full-load start-of-life stack efficiency does not only influence the full-load point but also the partial load. An increase in the stack efficiency results in more hydrogen production, thus a lower $LCoH_2$. Notably, the full-load start-of-life stack efficiency of 70% of the PEM electrolyser can be compared to the base case full-load start-of-life stack efficiency of the AE system, which is also 70%. One can see that the $LCoH_2$ is lower for the PEM electrolyser, resulting from the higher partial load curve and better load flexibility.

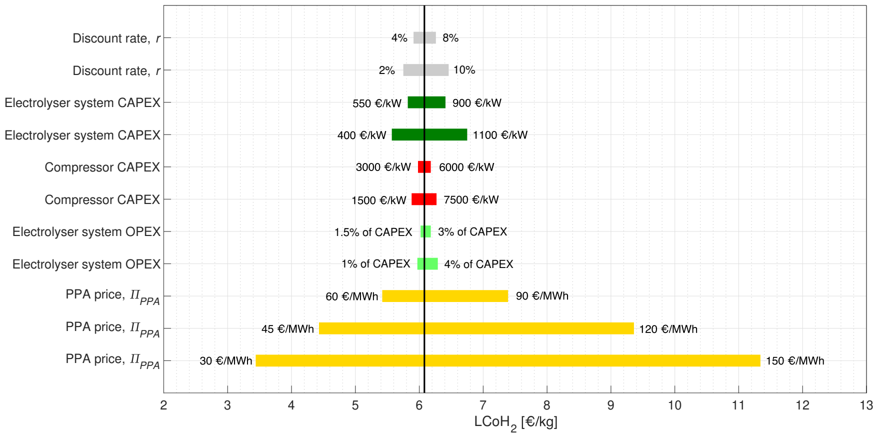

Figure 7.7: The sensitivity analysis for the $LCoH_2$ on the economic design parameters of the AE system. The black vertical line indicates the $LCoH_2$ of the base case, which is 6.08 €/kg for the AE system.

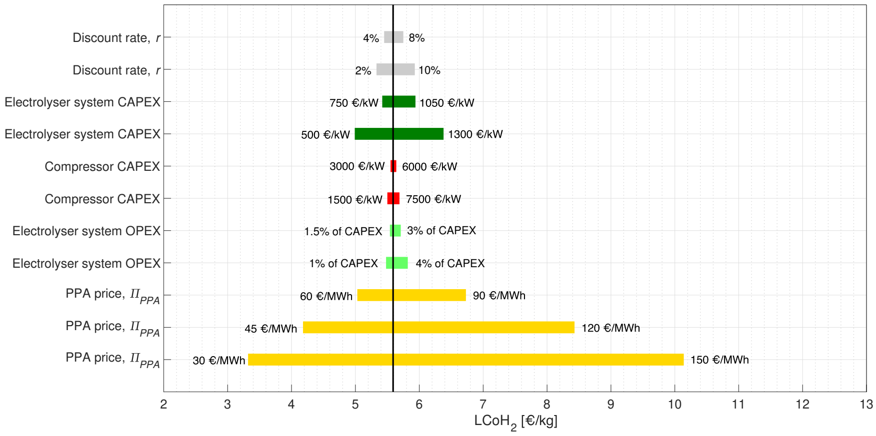

Figure 7.8: The sensitivity analysis for the $LCoH_2$ on the economic design parameters of the PEM electrolyser system. The black vertical line indicates the $LCoH_2$ of the base case, which is 5.59 €/kg for the PEM electrolyser system.

The degradation factor f_{deg} has a small effect on the $LCoH_2$. A higher degradation factor decreases the amount of hydrogen produced by the electrolyser system, which increases the $LCoH_2$. The BoP efficiency η_{BoP} influences the $LCoH_2$ by relatively much. An increase in the BoP efficiency would mean more electricity is directed to the electrolyser cells, which would increase the hydrogen production, which in turn would decrease the $LCoH_2$. The delivery pressure of hydrogen p_{del} influences the $LCoH_2$ by all sorts of effects. The expenses for the compressor influence the $LCoH_2$, but the compressor size also influences the amount of electricity that is used by the electrolyser cells. The results of 5 bar for the AE system and 30 bar for the PEM system reflect the system designs where the compressor is not present. Therefore, the sensitivity analysis on the delivery pressure of hydrogen shows the influence of the compressor on the $LCoH_2$.

7.2.2. Economic Design Parameters

The economic parameters for the AE and PEM electrolyser systems are explored in a sensitivity analysis, as outlined in Section 5.3. The results for the AE system are shown in Figure 7.7, while the findings for the PEM system are illustrated in Figure 7.8. It is important to note that the LCoH$_2$ on the x-axis of these figures have a much wider range compared to the sensitivity analysis on the design parameters. This will not directly indicate that the economic design parameters have more influence on the LCoH$_2$, as the ranges of the sensitivity analysis differ.

The discount rate r has a relatively limited effect on the LCoH$_2$ of both the AE and PEM systems. The largest contributor to the LCoH$_2$ was the costs of electricity. As both the expenses for the electricity and the hydrogen production are discounted at the same discount rate, the influence of the discount rate on the LCoH$_2$ is limited. However, compared to the system design parameters, the influence of the discount rate is substantial.

The electrolyser system CAPEX has a relatively large impact on the LCoH$_2$. This was expected from the results of the contributions to the LCoH$_2$. A system CAPEX of 400 €/kW and 500 €/kW of an AE and PEM electrolyser system would decrease the LCoH$_2$ to 5.57 €/kg and 4.99 €/kg, respectively. However, the compressor CAPEX and electrolyser system OPEX have a relatively limited effect on the LCoH$_2$.

The largest changes in the sensitivity analyses on the LCoH$_2$ are due to the PPA price Π_{PPA}. The PPA price directly affects the electrolyser OPEX by the electricity expenses. For an AE, a PPA price of 30 €/MWh and 150 €/MWh results respectively in an LCoH$_2$ of 3.44 €/kg and 11.34 €/kg. Accordingly, a PPA price of 30 €/MWh and 150 €/MWh for the PEM electrolyser system results in an LCoH$_2$ of 3.32 €/kg and 10.14 €/kg, respectively.

7.3. Levelised Cost of Heat

In this section, the LCoH$_{eat}$ findings are detailed and explored. Utilizing Equation 2.41 and reflecting the data and system design covered in this thesis, the LCoH$_2$ of the base case of the AE system stands at 1.57 €/MWh. The corresponding value for the PEM electrolyser system is 1.55 €/MWh. The breakdown and contributions of different kinds are displayed in Figure 7.9. The LCoH$_{eat}$ only reflects expenses related to the heat exchanger and pump, as those are the only additional components needed to recover the waste heat from a standard AE and PEM electrolyser system.

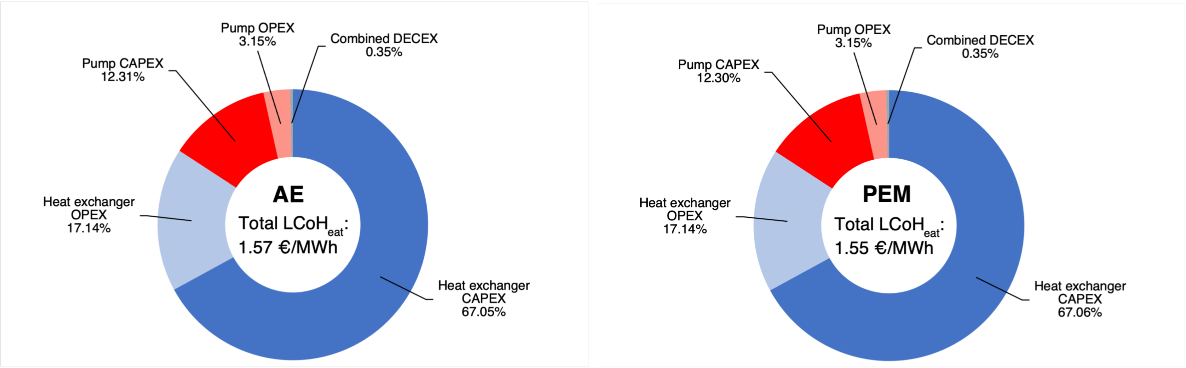

(a) The different contributions for the AE system to the LCoH$_2$ of 1.57 €/MWh.

(b) The different contributions for the PEM electrolyser system to the LCoH$_{eat}$ of 1.55 €/MWh.

Figure 7.9: The contributions of different expenses to the LCoH$_{eat}$ of the AE and PEM electrolyser systems. The contributions sum to 1 in both figures.

The initial system design of an AE and PEM electrolyser can be altered for heat recovery using the same approach consisting of a heat exchanger and a pump. Moreover, the maximum amount of heat recovery at end-of-life in both the AE and PEM electrolyser systems is almost equal, resulting in approximately the same costs related to the heat exchanger and pump. Additionally, the average heat production over the lifetime is almost equal, which results in the LCoH$_{eat}$ and cost distribution being almost equal.

As one can see, the CAPEX of the heat exchanger is the largest contributing factor to the LCoH$_{eat}$, followed by the OPEX of the heat exchanger. The total expenses related to the heat exchanger constitute 84.4% of the LCoH$_{eat}$ in both the AE and PEM electrolyser system, while the pump accounts for the remaining 15.6% of the LCoH$_{eat}$.

7.3.1. System Design Parameters

The sensitivity analysis for the $\mathrm{LCoH_{eat}}$ on the design parameters evaluates the same ranges as for $\mathrm{LCoH_2}$, with the addition of the thermal efficiency η_{th}. The sensitivity analysis on the system design parameters of the AE and PEM electrolyser system are depicted in Figure 7.10 and Figure 7.11, respectively.

As opposed to the $\mathrm{LCoH_2}$, the $\mathrm{LCoH_{eat}}$ demonstrates a considerable dependency on the installed plant capacity P_{instal}, as an increase in the installed plant capacity $\mathrm{LCoH_{eat}}$ lowers the $\mathrm{LCoH_{eat}}$. The heat production grows linearly with the increased installed plant capacity. However, both the CAPEX of the heat exchanger and the pump depend non-linearly on the installed plant capacity P_{instal}. The heat exchanger's power P_{HE} is calculated using Equation 5.1. Subsequently, the CAPEX of the heat exchanger is calculated by Equation 2.43, which depends on the square root of the power of the heat exchanger P_{HE}. The CAPEX of the pump, calculated byEquation 5.2, shows an approximate square root dependency on the pump flow rate Q_{pump}. Since the CAPEX of these components does not increase linearly, the costs per recovered MWh of heat reduce as the installed plant capacity increases. This kind of dependency of the $\mathrm{LCoH_{eat}}$ is reasonable, as doubling the capacity of components does not generally mean that the costs for the materials or the installation and monitoring labour hours also double.

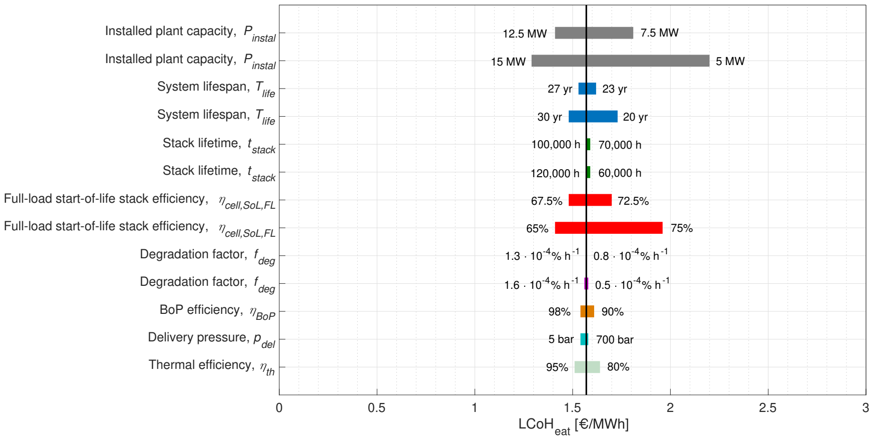

Figure 7.10: The sensitivity analysis for the $\mathrm{LCoH_{eat}}$ on the system design parameters of the AE system. The black vertical line indicates the $\mathrm{LCoH_{eat}}$ of the base case, which is 1.57 €/kg for the AE system.

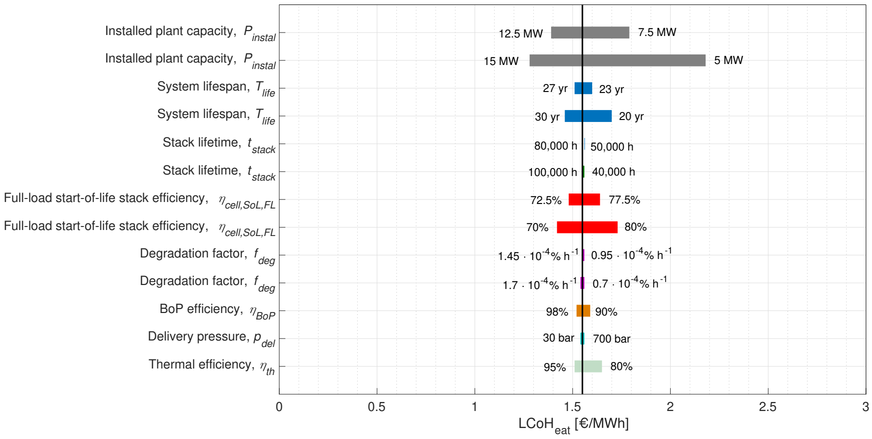

Figure 7.11: The sensitivity analysis for the $\mathrm{LCoH_{eat}}$ on the system design parameters of the PEM electrolyser system. The black vertical line indicates the $\mathrm{LCoH_{eat}}$ of the base case, which is 1.55 €/kg for the PEM electrolyser system.

The system lifespan T_{system} has relatively the same influence on the $\mathrm{LCoH_{eat}}$ as on the $\mathrm{LCoH_2}$ since an increase in the system lifespan produces more heat and thus decreases the $\mathrm{LCoH_{eat}}$. However, the results for the

LCoH$_{\text{eat}}$ do not depend on stack replacements, as the expenses for the stack replacements are included in the calculations for the LCoH$_2$.

Both the stack lifetime t_{stack} and degradation factor f_{deg} have a really small effect on the LCoH$_{\text{eat}}$. However, the effects are changed for the LCoH$_{\text{eat}}$ compared to the LCoH$_2$, as more degradation leads to more waste heat production and thus heat recovery. Therefore, a longer lifetime and a higher degradation factor lower the LCoH$_{\text{eat}}$.

A lower full-load start-of-life stack efficiency $\eta_{cell,SoL,FL}$ increases the production of heat. These results might propose to decrease the full-load start-of-life stack efficiency. However, the LCoH$_2$ rises when decreasing the full-load start-of-life stack efficiency. The primary objective of the system should be to maximise hydrogen production, given that hydrogen holds a higher value per MWh compared to waste heat at 70 °C. After reaching optimal hydrogen production levels, the focus can then turn to optimizing the recovery of waste heat.

The small changes in the delivery pressure p_{del} result from the diversion of electricity from the compressor to the electrolyser. More electricity used by the electrolyser increases the heat production, which in turn decreases the LCoH$_{\text{eat}}$. The effect of the thermal efficiency on LCoH$_{\text{eat}}$ is minimal. An increase in thermal efficiency means more heat recovery, which lowers the LCoH$_{\text{eat}}$.

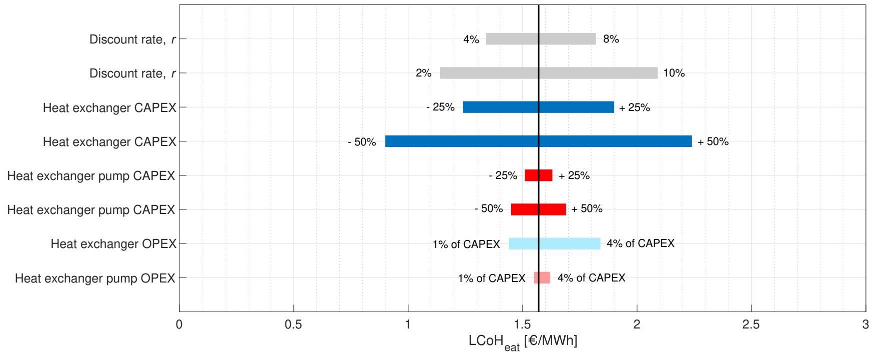

Figure 7.12: The sensitivity analysis for the LCoH$_{\text{eat}}$ on the economic design parameters of the AE system. The black vertical line indicates the LCoH$_{\text{eat}}$ of the base case, which is 1.57 €/kg for the AE system.

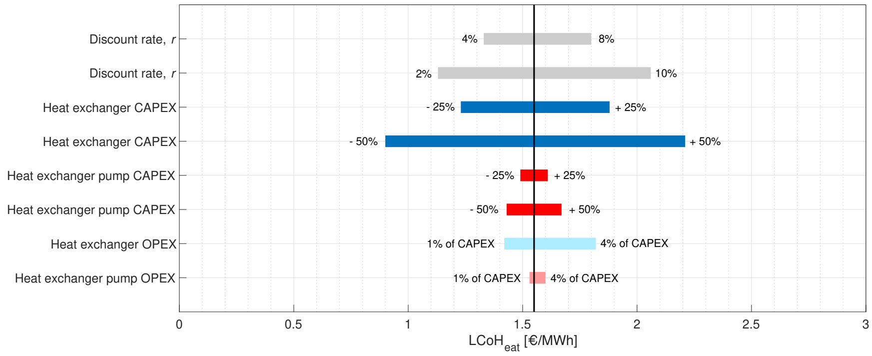

Figure 7.13: The sensitivity analysis for the LCoH$_{\text{eat}}$ on the economic design parameters of the PEM electrolyser system. The black vertical line indicates the LCoH$_{\text{eat}}$ of the base case, which is 1.55 €/kg for the PEM electrolyser system.

7.3.2. Economic Design Parameters

The sensitivity analysis of the economic design parameters on the AE and PEM electrolyser systems are illustrated in Figure 7.12 and Figure 7.13, respectively. The only expenses related to the LCoH$_{\text{eat}}$ are the heat exchanger and pump. The discount rate influences the LCoH$_{\text{eat}}$ relatively heavily for both the AE and PEM electrolyser systems. The influence is more than the influence discount rate had on the LCoH$_2$. This is logical as the calculation of the LCoH$_{\text{eat}}$ lacks a high OPEX like the electricity costs in the LCoH$_2$. Therefore, the CAPEX of the heat exchanger and pump dominates the expenses. Resultingly, mostly the heat production E_{heat} is discounted, while the CAPEX is not influenced by discounting as these expenses occur in year 0. A lower discount rate will lower the LCoH_{eat}, as the production of heat is discounted less, which results in more heat generation used in the calculation of the LCoH_{eat}.

The heat exchanger CAPEX influences the LCoH_{eat} a lot, as is expected from the results on the distribution of costs in Figure 7.9. When halving the heat exchanger CAPEX, the LCoH_{eat} also approximately halves. The influence of the changes in pump CAPEX is are too a lesser extent than the changes due to the heat exchanger CAPEX. Changes in the CAPEX of the heat exchanger and pump also influence the OPEX, since the OPEX is expressed as a percentage of the CAPEX. Changes in the percentages of the OPEX increase the LCoH_{eat} for a serious amount, but less than changes in their corresponding CAPEX.

8

Discussion

The discussion of this thesis is divided into multiple sections. The first section focuses on the results and the sensitivity analysis of the $LCoH_2$ and $LCoH_{eat}$ of the AE and PEM electrolyser systems in Section 8.1. The strengths and limitations of the approach and model employed in this thesis are discussed in Section 8.2. Lastly, Section 8.3 discusses the opportunities and threats for an electrolyser system in the Zuidplas region.

8.1. Putting the Levelised Cost of Hydrogen and Heat into Perspective

In this study, the $LCoH_2$ was 6.08 €/kg for the AE system and 5.59 €/kg for the PEM electrolyser system. These values were produced using wind farm power production data and wind speed data as input for a simulation of a semi-empirical electrolyser model that represents an AE or PEM electrolyser system. In literature, the values for the $LCoH_2$ of green hydrogen range from 3 approximately to 11 €/kg [Hancke et al., 2022; Pagani et al., 2022; IRENA, 2022; Christensen, 2020; Proost, 2019; LAZARD, 2021; Dinh et al., 2023]. The IEA [2020] indicates a range between 3.2 and 7.7 €/kg for hydrogen produced by renewable energy sources. The differences in the $LCoH_2$ in literature can be attributed to the assumptions on the electricity price (which depends on the renewable energy source), the amount of full-load hours, and the selected electrolyser technique, which influences the CAPEX of the system.

The variations in the $LCoH_2$ across different studies can primarily be ascribed to the specific assumptions on the electricity price. For example, Hancke et al. [2022] calculated an $LCoH_2$ of 9.71€/kg for hydrogen delivery at 700 bar for a PEM electrolyser system, assuming an electricity price of 120 €/MWh. Assuming a PPA price of 120 €/MWh in the model of this thesis, the $LCoH_2$ would be 9.36 €/kg and 8.43 €/kg for the AE and PEM electrolyser system, respectively. However, most literature seems to be optimistic about the future electricity prices in the calculation for the $LCoH_2$, which results in lower values for the $LCoH_2$ compared to this thesis. ORE Catapult [2020], for instance, predicts values of 35 €/MWh for electricity produced by offshore wind farms in Europe.

The quantity of full-load hours significantly impacts the $LCoH_2$ in literature, as it directly correlates with hydrogen production. In this thesis, however, the operating hours and full-load hours depend on the availability of wind energy, so it is not a changeable input parameter. To conclude, the values for the $LCoH_2$ in this thesis fall around the middle of ranges in the existing literature.

The $LCoH_2$ for green hydrogen production in Europe is expected to drop to levels below 2.5 €/kg in 2030 and below 2 €/kg in 2050 [Janssen et al., 2022; Calado and Castro, 2021]. Green electricity produced offshore at the offshore wind farms may even result in an $LCoH_2$ around 1.50 €/kg [Bechmann et al., 2023; Wagener, 2023]. However, waste heat from electrolysis cannot be effectively used when the electrolyser is located offshore [Tiktak, 2019].

The $LCoH_2$ of green hydrogen can also be compared to the $LCoH_2$ of other hydrogen production methods. Kovac et al. [2021] indicated that the price of grey and black hydrogen is around 1.50 €/kg, while the price of blue hydrogen was between 2 and 3 €/kg. The study by IRENA [2022] concluded that the cost of renewable electricity is so influential on the $LCoH_2$, that the production of green hydrogen is more expensive than blue hydrogen, regardless of the price of the electrolyser. As widely concluded in literature, the $LCoH_2$ of green hydrogen through electrolysis needs some serious cost reductions through cheaper materials or technological advancements, before it can compete with other forms of hydrogen production [Calado and Castro, 2021].

It is important to note that the values for the LCoH_2 in this thesis do not reflect the price that the hydrogen will be sold for at the refuelling station. Some costs at the refuelling station are not taken into account in the analysis. The costs for the storage of hydrogen at the refuelling station are not included, which can be substantial. As a refuelling station would already have storage facilities, storage is not included in this research. Since the electrolyser system is directly linked to the refuelling station, it would not be practical to maintain a separate storage facility. Based on the size of the storage facility compared to the installed capacity of the electrolyser, the increase of the LCoH_2 when implementing storage can range from 0.50 to 2.00 €/kg [Giampieri et al., 2023]. Additionally, the expenses for the pipeline connection and profit margins are not included in this thesis.

The LCoH_{eat} in this thesis was 1.57 €/kg and 1.55 €/MWh for the AE system and PEM electrolyser system, respectively. The study of van der Roest et al. [2023] quantifies the LCoH_{eat} at 8.4 €/MWh for the recovery of waste heat from a PEM electrolyser, that delivers waste heat to the heat buffer of a district heating network. This study described an LCoH_{eat} of 36.9 €/MWh for a system that upgrades the recovered waste heat using a heat pump. The increase in the LCoH_{eat} in the study of van der Roest et al. [2023] is the result of the inclusion of costs related to system components for the recovery of heat. The combination of a pipe for the delivery of the heat and electronics to control the system is assumed to account for approximately 65% of the total costs related to the recovery of waste heat.

The LCoH_{eat} of recovery of waste heat of an electrolyser can be compared to the LCoH_{eat} of other heat production methods. The heat from a heat pump produced from tap water has an LCoH_{eat} of approximately 60 €/MWh, assuming an electricity price of 83 €/MWh is assumed [van der Roest et al., 2023]. The waste heat from industry has an LCoH_{eat} of approximately 8 €/MWh. When a heat pump is added to the waste heat of industry, the LCoH_{eat} of waste heat from industry increases to 40 €/MWh [PBL, 2019]. The heat generated by a geothermal source, which includes a heat pump, has an LCoH_{eat} of around 60 €/MWh [CE Delft, 2018].

The outcome of the sensitivity analysis on LCoH_2 and LCoH_{eat} indicates that economic parameters typically exert more influence than system design parameters. This seems reasonable, as there are fewer economic parameters influencing the costs, compared to numerous parameters impacting the production of hydrogen and heat. However, the sensitivity only accounts for changes in one parameter at a time. In practice, technological advancements will most likely affect multiple design parameters simultaneously. As a result, the effect on the LCoH_2 and LCoH_2 is compounded by the different influences of these multiple parameters. For example, an increase in the stack lifetime will probably coincide with a reduction in the degradation factor.

The LCoH_2 and LCoH_{eat} in this thesis are linked since they are set up for the same installation. Therefore, the profits of selling the recovered waste heat can be utilised to lower the LCoH_2. In this approach, the profit in a given year is the amount of heat produced multiplied by the difference between the heat selling price and the LCoH_{eat}. The profit is discounted like all factors in the calculation of the LCoH_2. The modified formula for calculating the $\text{LCoH}_{2,\text{heat}}$ is

$$\text{LCoH}_{2,\text{heat}} = \frac{\sum_0^{T_{system}} \frac{CAPEX_{H_2,k}}{(1+r)^k} + \sum_0^{T_{system}} \frac{OPEX_{H_2,k}}{(1+r)^k} + \sum_0^{T_{system}} \frac{DECEX_{H_2,k}}{(1+r)^k} + \sum_0^{T_{system}} \frac{E_{heat,k}(\Pi_{heat} - \text{LCoH}_{\text{eat}})}{(1+r)^k}}{\sum_0^{T_{system}} \frac{m_{H_2,k}}{(1+r)^k}} \tag{8.1}$$

where Π_{heat} denotes the selling price of the recovered heat. The recovered waste heat selling price Π_{heat} is set from 10 €/MWh to 70 €/MWh. The results for both the AE and PEM electrolyser system are depicted in Figure 8.1 and Figure 8.2. The $\text{LCoH}_{2,\text{heat}}$ of the AE system was 5.97 €/kg and 5.18 €/kg for a waste heat selling price of 10 €/MWh and 70 €/MWh, respectively. The $\text{LCoH}_{2,\text{heat}}$ of the PEM system was 5.50 €/kg and 4.82 €/kg for respectively a waste heat selling price of 10 €/MWh and 70 €/MWh. At a waste heat selling price of 50 €/MWh, the profits from the sale of heat will decrease the LCoH_2 of the AE and PEM system by 0.64 €/kg and 0.44 €/kg, respectively. The decrease in LCoH_2 of the PEM system is less compared to the reduction in the AE system because more hydrogen is produced in the PEM system.

Economies of scale are not included in the calculation of the CAPEX of the electrolyser system and compressor. This is because in the literature there are no CAPEX values that depend on the installed capacity of an electrolyser system. However, elaborate studies on the pricing of an electrolyser system indicated that the CAPEX of the electrolyser system does depend on its installed capacity [ISPT, 2022; IRENA, 2022; Herings, 2021]. The studies indicate that certain system components depend non-linearly on the installed capacity of the electrolyser system. As a result, the CAPEX per MW for an increasing installed capacity becomes lower. This would lead to a decrease in the LCoH_2 when the installed capacity increases.

The LCoH_2 could potentially be reduced if entities like the European Union, Dutch Government, or another governmental organisation would provide subsidies for the generation of green hydrogen.

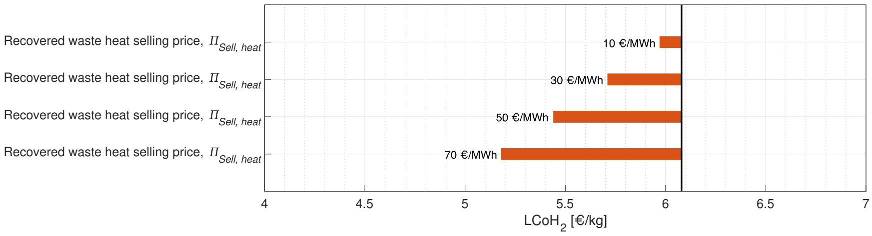

Figure 8.1: The $LCoH_{2,heat}$ of the AE system when selling the recovered heat at Π_{heat}. The black vertical line indicates the $LCoH_2$ of the base case, which is 6.08 €/kg for the AE system.

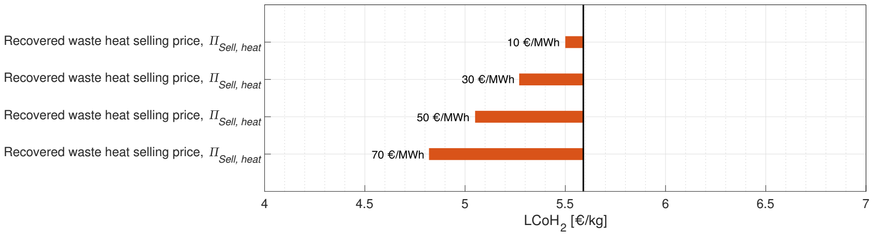

Figure 8.2: The $LCoH_{2,heat}$ of the PEM electrolyser system when selling the recovered heat at Π_{heat}. The black vertical line indicates the $LCoH_2$ of the base case, which is 5.59 €/kg for the PEM electrolyser system.

Upon examining the outcomes displayed in Figure 7.5 and Figure 7.6, one can see contradicting results for the sensitivity analysis on the system lifespan T_{system} and the stack lifetime t_{stack}. These inconsistencies stem from the timing of stack replacements, which are determined by the interplay of the system lifespan and stack lifetime. When designing an electrolyser system, stack replacements should be timed such that a stack reaches its end-of-life when the system reaches the end of its lifespan.

Both an AE system and a PEM electrolyser system are designed and simulated for the same business case and boundaries. Therefore, the results from both systems can be compared. In general, the PEM electrolyser performs better than the AE. Not only does the implementation of the PEM electrolyser result in a lower $LCoH_2$ and $LCoH_{eat}$, but also technological improvements and cost reductions are expected for PEM electrolysers in the coming years since the technique is not mature yet. Additionally, a metric that is not emphasized a lot in literature is that the operation of a PEM electrolyser under partial load is generally much better than an alkaline electrolyser. This quality is especially important when producing hydrogen from intermittent renewable energy sources.

8.2. Strengths and Limitations of the Models and Approaches

Many assumptions had to be made for this thesis, which can not all completely be discussed. In this section, the assumptions that could have the most impact or consequences on the results are discussed. First, the wind model will be discussed, followed by the electrolyser model and the levelised costs approach.

The 'wind farm power curve' method produces accurate power production data that account for the effects of a wind farm. Approaches on simulating the power production of a wind farm, based on the idealized power curve of Figure 2.12, would not include the wake effects and global-blockage effect influencing the power production in a wind farm. The study by Giampieri et al. [2023] is an example of a study that utilizes the idealized wind power curve, which still produces accurate results. However, utilizing the idealized power curve assumes a constant wind speed and a constant air density over the wind turbine rotor.

The wind farm power curve, based on the wind farm power production data of Baas et al. [2023], is not perfectly aligned with the ERA5 wind speed data and the power production data in Figure 6.3. This is logical as the ERA5 wind speed is not the sole input of the GRASP LES simulation of Baas et al. [2023]. Moreover, the 15-minute scale of the power production data is averaged to hourly data, which may introduce a bias by smoothing effects. Additionally, the wind farm power production depends on the direction of the ERA5 wind speed, as the layout is not symmetrical for every wind direction. To increase the wind farm power curve method, a wind farm power curve should be constructed for a certain number of wind speed directions. However, more power production data is required for this approach.

There are some differences between the IJmuiden wind farm of the data from Baas et al. [2023] and the Hollandse Kust VI and Hollandse Kust VII wind farms that are the focus of this thesis. Firstly, the IJmuiden Ver is a larger wind farm at 4 GW installed power, compared to the 700 MW Hollandse Kust VI and 760 MW Hollandse Kust VII wind farms. As a result, the wake effects and global-blockage effect will likely be slightly overestimated in the wind farm power curve that was used for the Hollandse Kust VI and VII. Secondly, the IJmuiden Ver wind farms are located closer to shore, so the average power production will likely be decreased, as a result of a lower average wind speed.

The biggest limitation of the electrolyser system is the lack of data in the literature on the performance of electrolysers. Consequently, results from simulations of empirical and semi-empirical models can not be validated by results from tested electrolysers. As there is virtually no literature about the recovery of waste heat published, this is especially the case for data on an electrolyser that incorporates the recovery of waste heat of electrolysers.

The model for the polarization curve of the AE stack is based on the model by Sanchez et al. [2018], while the model for the polarization curve of the PEM electrolyser stack is based on the approach by Falcao and Pinto [2020]. Both models do not include the condensation overpotential of Equation 2.8 for the cell potential U_{cell}. However, the models show good behaviour compared to polarization curves in the literature.

The Faraday efficiency of the AE stack has been simulated by the model by Ulleberg [2003], and the Faraday efficiency of the PEM electrolyser stack is simulated by the model by Yodwong et al. [2020]. Whereas, the model by Ulleberg [2003] includes the temperature dependence but neglects the pressure dependence, the model by Yodwong et al. [2020] includes the pressure dependence while neglecting the temperature dependence. However, better models are not present in literature, where the Faraday efficiency is often modelled by a constant value around 100% [Hernandez-Gomez et al., 2020]. The Faraday efficiency by the model of Ulleberg [2003] influences the partial load curve a lot, while it is based on parameters from 2003. This seems a little outdated and asks for a new determination using state-of-the-art AE stacks.

Electrolyser cell degradation is an important phenomenon when electrolysers operate for a longer time. However, there is not a lot of literature on this topic. The causes of cell degradation are studied, but the effect on the cell performance during long-term operation is understudied. In practice, cell degradation is an increase in the overpotential of the electrolyser. In this thesis, the degradation is accounted for using the degradation efficiency η_{deg}, and the motivation for this choice is presented in Section 6.2. It was concluded that this is an appropriate approach to modelling the degradation, as it shows the same behaviour as an increase in overpotential would. In this thesis, it is assumed that an electrolyser cell degrades the same amount, irrespective of the load applied to the electrolyser. This is a limitation of the research performed in this thesis since it seems reasonable to expect that there is more cell degradation when the electrolyser runs on 100% load compared to 20%. As a result, the approach could be improved by adding a partial load dependency to the degradation factor.

As a result of performing a steady-state simulation, the cold and hot startups are not included in this thesis. Both startups are related to the electrolyser system switching off. As the electrolyser is switched off as a result of intermittent wind energy, no heat is generated and the electrolyser will cool down over time. Therefore, it will cost energy to keep the electrolyser at the operating temperature of 80 °C. If the electrolyser is heated at operating temperature and switched on again, it is a hot start-up. A cold startup refers to the electrolyser switching on, but the temperature of the electrolyser has decreased to approximately the ambient temperature. In a cold startup, the heat produced by the electrolyser is used to heat the electrolyser itself. Such a cold startup occurs when there is a long period of no wind energy. Both a cold and a hot startup cost energy, in the form of electricity or heat. However, it is assumed that the electrolyser system in this thesis is fully insulated, which reduces the cooling when the electrolyser is switched off. Therefore, the effect is smaller compared to that in non-insulated electrolysers. Accurate short-term power forecasts are crucial for reliable and efficient integration of wind energy in power systems [Gilbert et al., 2020]. For electrolyser systems, this statement may be true since better forecasts can help predict cold and hot start-ups. The cold or hot start-ups will also influence cell degradation positively or negatively.

The BoP efficiency in this thesis is viewed as a constant efficiency loss over the load ratio, which means that it linearly changes with the load. However, there are components of the BoP that have constant electricity use, irrespective of the load on the electrolyser system, like the measuring and control equipment. Another limitation of the approach in this thesis is that the lifetime of the heat exchanger, compressor and pump are not included in the approach. Instead, the components are expected to have the same lifetime as the system lifespan. Therefore replacement of these components is not included in the model.

The results for the $LCoH_2$ and $LCoH_{eat}$ both show a very low dependence on the DECEX of the contributing components. This is logical as the expenses on decommissioning occur at the end of the lifetime and are thus discounted significantly by the discount factor. Additionally, costs for small system components are not included in this research for the $LCoH_{eat}$, like piping for the heat recovery in the district heating loop. However, these costs for the 'small' components can have a large influence on the $LCoH_{eat}$, as shown in the previous section based on the research by van der Roest et al. [2023].

Numbers for the CAPEX of the electrolyser system vary a lot in the literature. Additionally, it is unclear which costs are included in the calculations of the CAPEX. Some studies include the installation, cooling, and electronics, while others do not. There is no standard method for determining the CAPEX of electrolysers.

In this thesis, the delivery of waste heat is assumed to be on a constant temperature $T_{DHN,in}$ of 70 °C. However, in practice, there is a fluctuating inlet temperature requirement on a district heating network, with a higher temperature demand in winter [Hermans, 2021; Perik, 2021]. When the temperature fluctuates above the temperature that can be delivered by this system, heat delivery to the district heating level is not possible. In this case, an electrolyser system having a higher operating temperature can be designed, enabling the recovery of heat at a higher temperature. Besides, a design incorporating a heat pump can be created. However, adding a heat pump will greatly increase the $LCoH_{eat}$, as was discussed in the previous section.

8.3. Opportunities and Threats for the Implementation of the Electrolyser System

A threat of the case study is the sale of green hydrogen. Before an investment decision is to be made for this project, it is important to have an agreement with a hydrogen off-taker. Hydrogen trucks are not bought when there are no hydrogen fuel stations, while hydrogen fuel stations are not built when there are no hydrogen trucks. Thus, the market for green hydrogen in the transport sector increases only slowly, which results in uncertainty in the delivery of hydrogen to the transport sector [Mulder, 2022]. Therefore, reinsurance for the sale of hydrogen is required before constructing the electrolyser. The same threat is imposed on the sale of waste heat, and it is therefore important to have reassurance for the connection to the district heating network which can offtake the heat.

The production of hydrogen peaks at the start-of-life of the stack and thus also at the start of the system in 2027. At the start of the project, the hydrogen needs in the transport market are lower than the hydrogen needs at the end of the lifespan of the electrolyser system. This imposes an additional threat to the sale of hydrogen, which could be solved by constructing the total installed capacity of the electrolyser in parts. For example, one could first construct 5 MW of installed capacity in year 1 and an additional 5 MW in year 10, or another split over multiple years. An optimization to this end can be performed when more information about the expected hydrogen offtake in the transport sector or a specific area is available.

However, the threat of selling the hydrogen also poses an opportunity. One could perform a techno-economic study for having a refuelling station at the electrolyser system. In this way, the storage of hydrogen and delivery can be optimised and no expensive hydrogen pipeline between the electrolyser system and the refueling station is required. Additionally, the hydrogen demand can be implemented in a model to optimise the storage capacity. It may be important to have a second stream of hydrogen to the refuelling station, as there may be long times of low hydrogen production as a result of a low wind speed. This could be helped by tube trailers supplying energy from another green or maybe even grey hydrogen production site. Another option would be to connect to a hydrogen network like the national hydrogen network in the Netherlands. However, the operating pressure in the network is 30 bar and not the preferred 300 bar.

The OPEX of the recovered waste heat is very low for the electrolyser system in this thesis. The decentralised heat network in the region Lansingerland and Zuidplas may be designed in the same way as an electricity market, where suppliers and consumers of heat indicate respectively the highest and lowest price they are willing to receive or pay. In a heat market like this, the low OPEX of the electrolyser system will give the security of supplying the recovered heat when the electrolyser system is operational. This is based on the fact that the lowest amount of money the hydrogen operates wants to receive for the recovered heat is the amount for delivering the heat at that moment, which is the OPEX.

Another threat to the green electrolyser system is the variability in the requirements for the production of green hydrogen. The strict regulations on green hydrogen follow from the delegated acts of RED II. Applying some regulations, like the temporal correlation condition, could change the most optimal system design for an electrolyser. It is important to closely follow the latest regulatory developments in the green hydrogen sector.

As mentioned in Section 8.1, an opportunity for the green electrolyser system is that subsidies from the Dutch Government or the European Union could potentially be commissioned. In March 2023, the European Commission released plans for setting up the European Hydrogen Bank to boost sustainable hydrogen production by supporting investments in green hydrogen. The initiative is aimed to accelerate the investments in green hydrogen production, to reach the goal of 10 million tonnes of green hydrogen production by 2030 [European Commision, 2023]. The Dutch government provides SDE++ subsidies based on the lowest costs per avoided ton of CO_2 [PBL, 2023]. As a result, other methods might be prioritized over hydrogen in the merit order. However, the Dutch government could make exceptions for revolutionizing system designs. As the recovery of waste heat is not something that is widely implemented, this system design could qualify for this exception.

9

Conclusion & Recommendations for Future Research

9.1. Conclusion

The objective of this thesis was to gain insights into the degree of dependency of the Levelised Cost of Hydrogen ($LCoH_2$) and the Levelised Cost of Heat ($LCoH_{eat}$) of the recovered waste heat of an electrolysis plant on the factors constituting both levelised costs. To this end, both a system design employing an Alkaline Electrolyser (AE), and a system design based on a Proton-Exchange Membrane (PEM) electrolyser were developed. The electrolyser systems, operating at a temperature of 80 °C, were assumed to be connected to the grid where it receives electricity from a planned offshore wind farm through a virtual PPA. This approach was chosen since the system would adhere to the regulations of the European Union on renewable energy used for the production of green hydrogen. The produced hydrogen is delivered to a hydrogen refuelling station at a pressure of 350 bar, while it is assumed that the recovered heat is supplied to a district heating network at an inlet temperature of 70 °C. Next, the secondary questions of this thesis will be answered. Subsequently, this thesis is concluded by answering the main research question.

What is the optimal electrolysis system layout to directly recover waste heat from an electrolyser?

In a standard electrolyser system, heat is extracted from the electrolyser stack by a heat exchanger in the cooling system, which is connected to a dry cooler. In this thesis, an electrolyser layout that consists of a tie-in on the cooling system of the electrolyser is proposed. Heat is directly recovered from the electrolyser system, using only a heat exchanger and a pump. This approach eliminates the need for a costly heat pump to increase the temperature of the waste heat. The heat can be directly used to, for example, supply a medium-temperature district heating network. A key constraint of this method is that the heat can only be retrieved at temperatures beneath the operational temperature of the electrolyser cells.

How can both a green AE and PEM electrolysis system be most effectively modelled for long-term operation and a fluctuating load?

The AE and PEM electrolyser cells were simulated by modelling the polarization curve and Faraday efficiency curve, which both depend on the current density and power applied to the electrolyser cell. The polarization curve of the AE cell was simulated using the semi-empirical model by Sanchez et al. [2018], whereas the polarization curve of the PEM electrolyser cell was modelled following the empirical approach of Falcao and Pinto [2020]. The resulting polarization curves from both models displayed characteristics that are in line with the behaviour of practical electrolyser cells. The Faraday efficiency curve of the AE cell was simulated using the semi-empirical model of [Ulleberg, 2003], while the Faraday efficiency curve of the PEM electrolyser cell was simulated using the semi-empirical model of Yodwong et al. [2020]. Considering the models for the Faraday efficiency are designed for changes in one operational parameter, these two semi-empirical models for the Faraday efficiency require enhancements. Only the cell temperature is included in the model of Ulleberg [2003], while only the operating pressure is included in the model of Yodwong et al. [2020]. It is important to note that the Faraday efficiency curve has a considerable impact on the derived partial load curve for the AE cell.

In this thesis, the overpotential as a result of degradation of the electrolyser cell during operation was modelled as a heat-generating efficiency loss. This approach resulted in accurate results, reflecting the behaviour of an overpotential on the performance of an electrolyser. A potential enhancement of the proposed approach would be to introduce a dependency of the degradation factor, representing the degradation per hour, on the partial load.

When the recovery of waste heat was integrated, the total system efficiency of the AE at full-load and start-of-life of the stack increased from 63.0% to 83.4%, representing an increase of 20.4%. The full-load system efficiency at the end-of-life of the stack increased from 57.7% to 83%, representing an increase of 25.3%. Accordingly, the full-load system efficiency of the PEM electrolyser system increased from 69.0% to 89.6% at the start-of-life of the stack, while full-load system efficiency increased from 64.0% to 89.1% at the end-of-life. These values correspond to increases of 20.6% and 25.1%, respectively, for situations where the recovery of waste heat is incorporated into the system.

How can the power production of a wind farm be most effectively modelled?

The power production data of the offshore wind farm was simulated using the 'wind farm power curve' method. The wind farm power curve was constructed by coupling wind farm production data to the ERA5 wind speed data at a height of 100 m. The determination of the power production of the wind farm power at any ERA5 wind speed during the lifespan of the electrolyser can then be directly derived from the wind farm power curve. This method proved to be highly effective as it produces accurate results of actual power production by a wind farm, which includes the wake effects and global-blockage effect happening in actual wind farms. The 'wind farm power curve' method proved to be more accurate compared to methods utilizing the idealized wind turbine power curves since these effects are not considered in the idealized wind turbine power curve.

What are the levelised cost of hydrogen and heat for a potential electrolyser plant in Zuidplas?

The $LCoH_2$ of green hydrogen from the 10-MW AE plant designed for the region Zuidplas was 6.08 €/kg, while the $LCoH_{eat}$ of the recovered waste heat was 1.57 €/MWh. For the 10-MW PEM electrolyser plant, the $LCoH_2$ was determined to be 5.59 €/kg, while the associated $LCoH_{eat}$ for the recovered waste heat was 1.55 €/MWh. The values for the $LCoH_2$ of both the AE and PEM electrolyser system align with the literature, where a range for the $LCoH_2$ of green hydrogen from 3 to 11 €/kg was observed.

The profits of the sale of the recovered heat could be used to decrease the $LCoH_2$. When a selling price of 50 €/MWh was assumed for the recovered heat, the $LCoH_2$ of the AE and PEM electrolyser system was decreased to 5.44 €/kg and 5.05 €/kg, respectively. These results indicated a reduction in the $LCoH_2$ of respectively 0.64 €/kg and 0.44 €/kg for the AE and PEM electrolyser system. The decrease in the $LCoH_2$ of the AE system is more substantial since less hydrogen is produced over the lifetime of the AE system compared to the PEM electrolyser system.

To what extent do the levelised cost of hydrogen and the levelised cost of heat for a multi-MW heat-recovering green AE and PEM electrolysis plant depend on the design parameters and boundary conditions of the electrolyser system?

The main research question of this thesis is addressed by performing a sensitivity analysis of the results of the electrolyser model applied to the case study. The results of this thesis highlight that the $LCoH_2$ of both the AE and PEM electrolyser systems are strongly tied to the PPA price, affecting the Operational Expenses (OPEX) associated with the electrolyser. Relatively small changes in the PPA price resulted in massive swings in the $LCoH_2$. Consequently, cutting down the costs of renewable energy sources becomes crucial to reduce the financial burden of green hydrogen. Additionally, the Capital Expenditures (CAPEX) of the electrolyser system and the full-load start-of-life stack efficiency of the electrolyser significantly influence the $LCoH_2$. In general, the parameters of the system design of the electrolyser had a limited effect on the $LCoH_2$ but could have a substantial influence when advancements compound the improvements of the system design parameters.

The AE and PEM electrolyser systems exhibited a notably similar $LCoH_{eat}$, resulting from both having analogous expenses and similar quantities of recovered waste heat. The sensitivity analysis revealed that the $LCoH_{eat}$ is primarily influenced by the discount rate, heat exchanger CAPEX, and installed capacity of the electrolysis plant. The stack lifetime, the degradation factor and delivery pressure all hardly influence the $LCoH_{eat}$.

9.2. Recommendations for Future Research

In this chapter, recommendations for future research are outlined, all derived from the results of the research described in this thesis. This thesis provided insight into multiple research directions. The limitations of the models and approaches in this thesis result in recommendations for follow-up research. Additionally, opportunities for the production of hydrogen and the recovery of waste heat were observed, resulting in recommendations for follow-up research.

- First and foremost, current literature lacks performance data on the long-term operation of electrolyser stacks. Cell degradation diminishes the performance of an electrolyser over time and this effect should also be included in simulations. Accurate experiments for the degradation of state-of-the-art electrolysers would increase the knowledge about the degradation of electrolysers. An increase in knowledge would enhance the precision and reliability of electrolyser modelling.
- In this thesis, a simulation of the electrolyser system under steady-state conditions was performed. This simplifies the dynamic behaviour of the electrolyser system. It would be a great addition if a dynamic analysis of the extraction of waste heat would be performed. This analysis would be simulated on a shorter timescale to include the cold and hot start-ups of the electrolyser system. Together with the results of this study, the results of the dynamic study could be used to design an optimal electrolyser system in great detail for the recovery of waste heat.
- The subject of waste heat recovery from an electrolyser remains relatively unexplored and presents ample opportunities for subsequent research. Firstly, values for the thermal efficiency, which indicates the fraction of waste heat that is recovered in an electrolyser stack, are now solely based on simulations. The literature lacks empirical data from real-world experiments. Additionally, the proposed system design for the recovery of waste heat of this thesis could be tested and precisely designed. Moreover, the heat losses from the proposed heat recovery system design up until delivery to the district heating network could be simulated.
- In this thesis, the produced green hydrogen is delivered to a hydrogen refuelling station. A joint system, combining an electrolyser and a refuelling station, could be simulated in follow-up research. Such a study could further delve into optimising the storage capabilities of the refuelling station.

Bibliography

A12-corridor (2021). Bedrijvenparken. `https://a12-corridor.nl/bedrijvenparken//`. Accessed: 11-06-2023.

Abdin, Z., Webb, C. J., and Gray, E. M. (2015). Modelling and simulation of a proton exchange membrane (pem) electrolyser cell. *International Journal of Hydrogen Energy*, 40:13243–13257.

Amores, E., Rodríguez, J., Oviedo, J., and Lucas-Consuegra, A. D. (2017). Development of an operation strategy for hydrogen production using solar pv energy based on fluid dynamic aspects. *Open Engineering*, 7:141–152.

Baas, P., Verzijlbergh, R., Van Dorp, P., and Jonker, H. (2023). Investigating energy production and wake losses of multi-gigawatt offshore wind farms with atmospheric large-eddy simulation. *Wind Energy Science*, 8:787–805.

Baresi, M. (2021). Breakthrough to clean hydrogen through waste heat. `https://wetten.overheid.nl/BWBR0046360/2022-04-01`. Accessed: 25-07-2023.

Bechmann, A., Barlas, T., Frandsen, H., Jin, L., and Nakashima, R. (2023). The hydrogen wind turbine: Design of a wind turbine optimised for hydrogen production. *Journal of Physics: Conference Series*, 2507.

BNEF (2023). Corporations Brush Aside Energy Crisis, Buy Record Clean Power. `https://about.bnef.com/blog/corporations-brush-aside-energy-crisis-buy-record-clean-power/`. Accessed: 22-03-2023.

Buttler, A. and Spliethoff, H. (2018). Current status of water electrolysis for energy storage, grid balancing and sector coupling via power-to-gas and power-to-liquids: A review. *Renewable and Sustainable Energy Reviews*, 82:2440–2454.

Calado, G. and Castro, R. (2021). Hydrogen production from offshore wind parks: Current situation and future perspectives. *Applied Sciences (Switzerland)*, 11.

Carmo, M., Fritz, D. L., Mergel, J., and Stolten, D. (2013). A comprehensive review on pem water electrolysis. *International Journal of Hydrogen Energy*, 38:4901–4934.

CE Delft (2018). Weg van gas - Kansen voor de nieuwe concepten Lage Temperatuur Aardwarmte en Mijnwater.

Christensen, A. (2020). Assessment of Hydrogen Production Costs from Electrolysis: United States and Europe. `https://theicct.org/publication/assessment-of-hydrogen-production-costs-from-electrolysis-united-states-and-europe/`. Accessed: 4-08-2023.

Dale, N. V., Mann, M. D., and Salehfar, H. (2008). Semiempirical model based on thermodynamic principles for determining 6kw proton exchange membrane electrolyzer stack characteristics. *Journal of Power Sources*, 185:1348–1353.

DatacenterDynamics (2023). Power Purchase Agreement prices up nearly 50% in Europe over last year. `https://www.datacenterdynamics.com/en/news/power-purchase-agreement-prices-up-nearly-50-in-europe-over-last-year/`. Accessed: 22-03-2022.

de Kleijne, K., de Coninck, H., van Zelm, R., Huijbregts, M. A., and Hanssen, S. V. (2022). The Many Greenhouse Gas Footprints of Green Hydrogen. *Sustainable Energy Fuels*, 6:4383–4387.

Dell, R. M., Moseley, P. T., and Rand, D. A. (2014). Hydrogen, fuel cells and fuel cell vehicles. *Towards Sustainable Road Transport*, pages 260–295.

Dinh, Q., Dinh, V., Masadeghi, H., Pereira, P., and Leahy, P. (2023). A geospatial method for estimating the levelised cost of hydrogen production from offshore wind. *International Journal of Hydrogen Energy*, 48.

ECMWF (2023). ERA5: data documentation. `https://confluence.ecmwf.int/display/CKB/ERA5%3A+data+documentation`. Accessed: 19-05-2023.

ENGIE (2021). What are Power Purchase Agreements? `https://www.engie.com/en/news/ppa-power-purchase-agreement-what-is-it`. Accessed: 22-03-2023.

Engineering ToolBox (2003). Fuels - Higher and Lower Calorific Values.

European Commision (2023). Commission outlines European Hydrogen Bank to boost renewable hydrogen. `https://energy.ec.europa.eu/news/commission-outlines-european-hydrogen-bank-boost-renewable-hydrogen-2023-03-16_en`. Accessed: 6-08-2023.

European Commission (2018). DIRECTIVE (EU) 2018/2001 OF THE EUROPEAN PARLIAMENT AND OF THE COUNCIL of 11 December 2018 on the promotion of the use of energy from renewable sources (recast).

European Commission (2020). A hydrogen strategy for a climate-neutral europe.

European Commission (2023a). COMMISSION DELEGATED REGULATION (EU) of 10.2.2023 supplementing Directive (EU) 2018/2001 of the European Parliament and of the Council by establishing a minimum threshold for greenhouse gas emissions savings of recycled carbon fuels and by specifying a methodology for assessing greenhouse gas emissions savings from renewable liquid and gaseous transport fuels of non-biological origin and from recycled carbon fuels.

European Commission (2023b). COMMISSION DELEGATED REGULATION (EU) of 10.2.2023 supplementing Directive (EU) 2018/2001 of the European Parliament and of the Council by establishing a Union methodology setting out detailed rules for the production of renewable liquid and gaseous transport fuels of non-biological origin.

European Commission (2023c). Commission sets out rules for renewable hydrogen.

European Commission (2023d). Renewable Energy Directive. `https://energy.ec.europa.eu/topics/renewable-energy/renewable-energy-directive-targets-and-rules/renewable-energy-directive_en`. Accessed: 20-03-2023.

European Investment Bank (2022). Infrastructure Solutions: The power of purchase agreements. `https://www.eib.org/en/essays/renewable-energy-power-purchase-agreements`. Accessed: 22-03-2023.

Falcao, A. and Pinto, A. (2020). A review on pem electrolyzer modelling: Guidelines for beginners. *Journal of Cleaner Production*, 261.

Gallandat, N., Romanowicz, K., and Züttel, A. (2017). An analytical model for the electrolyser performance derived from materials parameters. *Journal of Power and Energy Engineering*, 05:34–49.

Gambou, F., Guilbert, D., Zasadzinski, M., and Rafaralahy, H. (2022). A comprehensive survey of alkaline electrolyzer modeling: Electrical domain and specific electrolyte conductivity. *Energies 2022, Vol. 15, Page 3452*, 15:3452.

Garcia-Valverde, R., Espinosa, N., and Urbina, A. (2012). Simple pem water electrolyser model and experimental validation. *International Journal of Hydrogen Energy*, 37.

Gasunie (2022). Hydrogen quality for the Dutch network. `https://www.gasunie.nl/en/expertise/hydrogen/hydrogen-and-industry/hydrogen-quality-for-the-dutch-network#:~:text=For%20example%2C%20we%20know%20that,%2C%2098%25%20purity%20is%20sufficient`. Accessed: 25-07-2023.

GET H2 (2021). Kickstarting the energy transition with hydrogen. `https://www.get-h2.de/en/initiativeandvision/`. Accessed: 12-07-2023.

GHE (2022). Klimaneutrales Stadtquartier in Esslingen. `https://green-hydrogen-esslingen.de/`. Accessed: 12-07-2023.

Giampieri, A., Ling-Chin, J., and Roskilly, A. P. (2023). Techno-economic assessment of offshore wind-to-hydrogen scenarios: A uk case study. *International Journal of Hydrogen Energy*.

Gilbert, C., Messner, J. W., Pinson, P., Trombe, P. J., Verzijlbergh, R., van Dorp, P., and Jonker, H. (2020). Statistical post-processing of turbulence-resolving weather forecasts for offshore wind power forecasting. *Wind Energy*, 23:884–897.

Glenk, G. and Reichelstein, S. (2019). Economics of converting renewable power to hydrogen. *Nature Energy*, 4.

Google Earth (2023).

Greenport West-Holland (2022). De ontwikkeling van het regionale Warmtenet in Oostland. `https://greenportwestholland.nl/de-ontwikkeling-van-het-regionale-warmtenet-in-oostland/`. Accessed: 11-07-2023.

Grigoriev, S., Fateev, V., Bessarabov, D., and Millet, P. (2020). Current status, research trends, and challenges in water electrolysis science and technology. *International Journal of Hydrogen Energy*, 45:26036–26058.

Grigoriev, S. A., Millet, P., Volobuev, S. A., and Fateev, V. N. (2009). Optimization of porous current collectors for pem water electrolysers. *International Journal of Hydrogen Energy*, 34:4968–4973.

Hancke, R., Holm, T., and Ulleberg, O. (2022). The case for high-pressure pem water electrolysis. *Energy Conversion and Management*, 261:115642.

Harrison, K., Remick, R., Martin, G., and Hoskin, A. (2010). Hydrogen production: Fundamentals and cas study summaries.

Herings, G. (2021). Understanding the Potential of Up-numbering for a Gigawatt Scale Green Hydrogen Facility. Master's thesis, Eindhoven University of Technology.

Hermans, E. (2021). Extracting and Utilising Heat from an Hydrogen Production Plant. Master's thesis, Delft University of Technology.

Hernandez-Gomez, A., Ramirez, V., and Guilbert, D. (2020). Investigation of pem electrolyzer modeling: Electrical domain, efficiency, and specific energy consumption. *International Journal of Hydrogen Energy*, 45:14625–14639.

Hersbach, H., Bell, B., Berrisford, P., Hirahara, S., Horányi, A., Muñoz-Sabater, J., Nicolas, J., Peubey, C., Radu, R., Schepers, D., Simmons, A., Soci, C., Abdalla, S., Abellan, X., Balsamo, G., Bechtold, P., Biavati, G., Bidlot, J., Bonavita, M., Chiara, G. D., Dahlgren, P., Dee, D., Diamantakis, M., Dragani, R., Flemming, J., Forbes, R., Fuentes, M., Geer, A., Haimberger, L., Healy, S., Hogan, R. J., Hólm, E., Janisková, M., Keeley, S., Laloyaux, P., Lopez, P., Lupu, C., Radnoti, G., de Rosnay, P., Rozum, I., Vamborg, F., Villaume, S., and Thépaut, J. N. (2020). The ERA5 Global Reanalysis. *Quarterly Journal of the Royal Meteorological Society*, 146:1999–2049.

HHGH (2021). Shell, Mitsubishi Heavy Industries, Vattenfall and Wärme Hamburg sign Letter of Intent for 100MW Hydrogen Project in Hamburg. `https://www.get-h2.de/en/initiativeandvision/`. Accessed: 12-07-2023.

Hollingsworth, J., Phillippi, G., Hinchliff, M., Kulhanek, C., Rimpel, A. M., and Maywald, F. (2019). *Reciprocating Compressors*. Gulf Professional Publishing.

Holst, M., Aschbrenner, S., Smolinka, T., Voglstatter, C., and Grimm, G. (2021). Cost forecast for low-temperature electrolysis - technology driven bottom-up prognosis for pem and alkaline water electrolysis systems. *Fraunhofer Institute for Solar Energy Systems ISE*.

IEA (2020). Global average levelised cost of hydrogen production by energy source and technology, 2019 and 2050. https://www.iea.org/data-and-statistics/charts/global-average-levelised-cost-of-hydrogen-production-by-energy-source-and-technology-2019-and-205 Accessed: 5-08-2023.

IEA (2022a). Offshore wind outlook 2022: World energy outlook special report.

IEA (2022b). Renewables 2022.

IKZ (2017). Der Stromlückenfüller. https://www.ikz.de/detail/news/detail/der-stromlueckenfueller/. Accessed: 12-07-2023.

IPCC (2023). Climate Change 2023.

IRENA (2022). Green Hydrogen Cost Reduction: Scaling up Electrolysers to Meet the 1.5C Climate Goal.

ISPT (2022). A one-gigawatt green-hydrogen plant: Advanced design and total installed-capital costs.

Ito, H., Maeda, T., Nakano, A., Hwang, C. M., Ishida, M., Kato, A., and Yoshida, T. (2012). Experimental study on porous current collectors of pem electrolyzers. *International Journal of Hydrogen Energy*, 37:7418–7428.

Janssen, J. L. L. C. C., Weeda, M., Detz, R. J., and Zwaan, B. V. D. (2022). Country-specific cost projections for renewable hydrogen production through off-grid electricity systems. *Applied Energy*, 309.

JRC (2021a). Defining and accounting for waste heat and cold. https://publications.jrc.ec.europa.eu/repository/handle/JRC126383.

JRC (2021b). Historical Analysis of FCH 2 JU Electrolyser Projects. https://publications.jrc.ec.europa.eu/repository/handle/JRC121704.

Kast, J., Vijayagopal, R., Gangloff, J. J., and Marcinkoski, J. (2017). Clean commercial transportation: Medium and heavy duty fuel cell electric trucks. *International Journal of Hydrogen Energy*, 42:4508–4517.

Khater, H. A., Abdelraouf, A. A., and Beshr, M. H. (2011). Optimum alkaline electrolyzer-proton exchange membrane fuel cell coupling in a residential solar stand-alone power system. *ISRN Renewable Energy*, pages 1–13.

Kovac, A., Paranos, M., and Marcius, D. (2021). Hydrogen in Energy Transition: A Review. *International Journal of Hydrogen Energy*, 46:10016–10035.

Kumar, S. S. and Himabindu, V. (2019). Hydrogen production by pem water electrolysis a review. *Materials Science for Energy Technologies*, 2:442–454.

KWR (2018). Power-to-x: Werken aan de energietransitie in nieuwegein.

KWR (2023). H-Flex: green hydrogen in a flexible electricity system. https://www.kwrwater.nl/en/projecten/h-flex-green-hydrogen-in-a-flexible-electricity-system/. Accessed: 12-07-2023.

Lange, H., Klose, A., Lippmann, W., and Urbas, L. (2023). Technical evaluation of the flexibility of water electrolysis systems to increase energy flexibility: A review. *International Journal of Hydrogen Energy*, 48:15771–15783.

LAZARD (2021). Lazard's levelized cost of hydrogen analysis - version 2.0.

Le Coultre, F. (2022). Utilisation of Heat Released During the Production of Green Hydrogen Using Alkaline Electrolysis. Master's thesis, Delft University of Technology.

Lettenmeier, P. (2021). Effiency - Electrolysis. *Siemens*.

LevelTen Energy (2023). European Solar Energy Contract Prices Soared 60% Year Over Year, and Wind Availability Plummeted, According to LevelTen Energys Fourth Quarter Report. https://www.leveltenenergy.com/post/europe-2022q4-press-release. Accessed: 22-03-2023.

Lohmann-Richters, F. P., Renz, S., Lehnert, W., Müller, M., and Carmo, M. (2021). Reviewchallenges and opportunities for increased current density in alkaline electrolysis by increasing the operating temperature. *Journal of The Electrochemical Society*, 168:114501.

Lummen, N., Karouach, A., and Tveitan, S. (2019). Thermo-economic study of waste heat recovery from condensing steam for hydrogen production by pem electrolysis. *Energy Conversion and Management*, 185:21–34.

Mann, R. F., Amphlett, J. C., Hooper, M. A., Jensen, H. M., Peppley, B. A., and Roberge, P. R. (2000). Development and application of a generalised steady-state electrochemical model for a pem fuel cell. *Journal of Power Sources*, 86:173–180.

Marcu, A., Imbault, O., and Fernandez, A. (2021). ERCST hydrogen paper: the Fit for 55 package and its implications for the EU hydrogen economy.

Ministerie van Economische Zaken en Klimaat (2022). Kamerbrief: Ontwikkeling transportnet voor waterstof.

Mori, M., Mrzljak, T., Drobnic, B., and Sekavcnik, M. (2013). Integral characteristics of hydrogen production in alkaline electrolysers. *Journal of Mechanical Engineering*, 59:585–594.

Mulder, A. (2022). De kip, het ei en de kippenslachterij. `https://energeia.nl/energeia-artikel/40104307/de-kip-het-ei-en-de-kippenslachterij#:~:text=Voor%20elke%20GJ%20aan%20schone,kg%20waterstof%20aan%20de%20pomp`. Accessed: 6-08-2023.

Next Kraftwerke (2021). What is a Power Purchase Agreement (PPA)? `https://www.next-kraftwerke.be/en/knowledge-hub/ppa-power-purchase-agreement`. Accessed: 22-03-2023.

Niu, B., Hwangbo, H., Zeng, L., and Ding, Y. (2018). Evaluation of alternative power production efficiency metrics for offshore wind turbines and farms. *Renewable Energy*, 128.

NREL (2020). Definition of the IEA Wind 15-Megawatt Offshore Reference Wind Turbine. NREL/TP-5000-75698.

NWP (2022). Routekaart Waterstof. `https://open.overheid.nl/documenten/ronl-4e9a5511ce0f4193c14ef14fe7f820838b84fb03/pdf`.

ORE Catapult (2020). Offshore Wind and Hydrogen - Solving the Integration Challenge.

Overheid.nl (2022a). Kavelbesluit VI windenergiegebied Hollandse Kust (west). `https://wetten.overheid.nl/BWBR0046360/2022-04-01`. Accessed: 23-03-2023.

Overheid.nl (2022b). Kavelbesluit VII windenergiegebied Hollandse Kust (west). `https://wetten.overheid.nl/BWBR0046414/2022-04-01`. Accessed: 23-03-2023.

Ozaki, M., Tomura, S., Ohmura, R., and Mori, Y. H. (2014). Comparative study of large-scale hydrogen storage technologies: Is hydrate-based storage at advantage over existing technologies? *International Journal of Hydrogen Energy*, 39:3327–3341.

Pagani, G., Acar, C., and Hajimolana, Y. (2022). Green Hydrogen for Ammonia Production - a Case for the Netherlands. *Proceedings of WHEC 2022 - 23rd World Hydrogen Energy Conference: Bridging Continents by H2*.

Pascuzzi, S., Anifantis, A., Blanco, I., and Mugnozza, G. (2016). Electrolyzer performance analysis of an integrated hydrogen power system for greenhouse heating a case study. *Sustainability (Switzerland)*, 8:1–15.

PBL (2019). Conceptadvies sde++ co2 reducerende opties.

PBL (2023). Eindadvies basisbedragen sde++ 2023.

Perez, R. J., Brent, A. C., and Hinkley, J. (2021). Assessment of the potential for green hydrogen fuelling of very heavy vehicles in new zealand. *Energies*, 14:2636.

Perik, R. (2021). Thermal Energy Storage for District Heating - Feasibility Assessment for the Implementation of TES Systems in various DHN cases. Master's thesis, Delft University of Technology.

Pinsky, R., Sabharwall, P., Hartvigsen, J., and O'brien, J. (2020). Comparative review of hydrogen production technologies for nuclear hybrid energy systems . *Progress in Nuclear Energy*, 123.

Platzer, M. and Sarigul-Klijn, N. (2020). Current Status of Global Energy Consumption, Production, and Storage. *The Green Energy Ship Concept*, pages 11,16.

Proost, J. (2019). State-of-the art capex data for water electrolysers, and their impact on renewable hydrogen price settings. *International Journal of Hydrogen Energy*, 44:4406–4413.

Rijksoverheid (2022). Ontwerp beleids-programma klimaat. *Ministerie van Economische Zaken en Klimaat*.

Rijksoverheid (2022). Windenergie op zee. `https://www.rijksoverheid.nl/onderwerpen/duurzame-energie/windenergie-op-zee`. Accessed: 22-03-2023.

Rijksoverheid (2023a). Stimulering gebruik van waterstof. `https://www.rijksoverheid.nl/onderwerpen/duurzame-energie/overheid-stimuleert-de-inzet-van-meer-waterstof#:~:text=In%202030%20is%20de%20elektrolysecapaciteit,8%20gigawatt%20elektrolysecapaciteit%20in%202032`. Accessed: 10-07-2023.

Rijksoverheid (2023b). Windpark boven Groningen beoogd als s werelds grootste waterstof op zee productie in 2031. `https://www.rijksoverheid.nl/actueel/nieuws/2023/03/20/windpark-boven-groningen-beoogd-als-s-werelds-grootste-waterstof-op-zee-productie-in-2031`. Accessed: 11-07-2023.

Ruttloff, M., Topf, C., von Andreae, J., Kappler, L., and Kindler, L. (2023). European Commission Defines Green Hydrogen.

RVO (2021). Warmteweb B3-hoek. `https://data.rvo.nl/subsidies-regelingen/projecten/warmteweb-b3-hoek`. Accessed: 11-07-2023.

RVO (2023a). Plans 2030-2050. `https://english.rvo.nl/information/offshore-wind-energy/offshore-wind-energy-plans-2030-2050`. Accessed: 22-03-2023.

RVO (2023b). Windparken op de Noordzee. `https://www.rvo.nl/subsidies-financiering/windenergie-op-zee/actieve-windparken`. Accessed: 22-03-2023.

Salehmin, M. N. I., Husaini, T., Goh, J., and Sulong, A. B. (2022). High-pressure pem water electrolyser: A review on challenges and mitigation strategies towards green and low-cost hydrogen production. *Energy Conversion and Management*, 268:115985.

Sanchez, M., Amores, E., Rodriguez, L., and Clemente-Jul, C. (2018). Semi-empirical model and experimental validation for the performance evaluation of a 15 kw alkaline water electrolyzer. *International Journal of Hydrogen Energy*, 43:20332–20345.

Schmidt, O., Gambhir, A., Staffell, I., Hawkes, A., Nelson, J., and Few, S. (2017). Future cost and performance of water electrolysis: An expert elicitation study. *International Journal of Hydrogen Energy*, 42:30470–30492.

Siracusano, S., Baglio, V., Moukheiber, E., Merlo, L., and Arico, A. S. (2015). Performance of a pem water electrolyser combining an irru-oxide anode electrocatalyst and a short-side chain aquivion membrane. *International Journal of Hydrogen Energy*, 40:14430–14435.

SolarPower Europe (2022). European Parliament officially adopts 45% renewable target but creates uncertainty around renewable hydrogen.

Suermann, M., Bensmann, B., and Hanke-Rauschenbach, R. (2019). Degradation of proton exchange membrane (pem) water electrolysis cells: Looking beyond the cell voltage increase. *Journal of The Electrochemical Society*, 166:F645–F652.

Suermann, M., Schmidt, T. J., and Büchi, F. N. (2018). Comparing the kinetic activation energy of the oxygen evolution and reduction reactions. *Electrochimica Acta*, 281:466–471.

Taghizadeh-Hesary, F., Li, Y., Rasoulinezhad, E., Mortha, A., Long, Y., Lan, Y., Zhang, Z., Li, N., Zhao, X., and Wang, Y. (2021). Hydrogen sourced from renewables and clean energy: A feasibility study of achieving large-scale demonstration. *ERIA Research Project Report*.

TenneT (2022). Zuidplaspolder). `https://www.tennet.eu/nl/projecten/zuidplaspolder`. Accessed: 26-04-2023.

TenneT (2023a). Bidding Zone Review: TSOs investigate alternative bidding zone configurations. `https://www.tennet.eu/news/bidding-zone-review-tsos-investigate-alternative-bidding-zone-configurations`. Accessed: 17-03-2023.

TenneT (2023b). Grid capacity map. `https://netztransparenz.tennet.eu/electricity-market/connecting-to-the-dutch-high-voltage-grid/grid-capacity-map/`. Accessed: 26-06-2023.

Tijani, A. S., Afiqah, N., Kamarudin, B., Athirah, F., and Mazlan, B. (2018). Investigation of the effect of charge transfer coefficient (ctc) on the operating voltage of polymer electrolyte membrane (pem) electrolyzer. *International Journal of Hydrogen Energy*, 43.

Tiktak, W. J. (2019). Heat Managementof PEM Electrolysis. Master's thesis, Delft University of Technology.

Tromp, E., Bekkering, J., Hengeveld, E. J., Bellekom, S., and jaap Aué, J. (2022). Cost minimisation of renewable hydrogen in a dutch neighbourhood while meeting european union sustainability targets. *Energy Conversion and Management*, 267:115903.

Ulleberg, O. (2003). Modeling of advanced alkaline electrolyzers: A system simulation approach. *International Journal of Hydrogen Energy*, 28:21–33.

Ulleberg, O., Nakken, T., and Eté, A. (2010). The wind/hydrogen demonstration system at utsira in norway: Evaluation of system performance using operational data and updated hydrogen energy system modeling tools. *International Journal of Hydrogen Energy*, 35:1841–1852.

van den Akker, H. and Mudde, R. (2023). *Transport Phenomena: The Art of Balancing*. Delft Academic Press, Delft.

van der Roest, E., Bol, R., Fens, T., and van Wijk, A. (2023). Utilisation of waste heat from pem electrolysers unlocking local optimisation. *International Journal of Hydrogen Energy*.

van Thuyne, G., Sauzay, A., O'Reilly, R., Serra, F., and Meister, M. (2022). RED II Draft Delegated Acts; The missing pieces of the EUs hydrogen puzzle. *Allen & Overy*.

Verschuuren, J. (2022). Achieving agricultural greenhouse gas emission reductions in the eu post-2030: What options do we have? *Review of European, Comparative International Environmental Law*, 31:246–257.

Villarreal Vives, A. M., Wang, R., Roy, S., and Smallbone, A. (2023). Techno-economic analysis of large-scale green hydrogen production and storage. *Applied Energy*, 346.

Wagener, J. (2023). A Future Techno-Economic Evaluation of an Offshore Wind-Hydrogen System with Battolyser Technology on the Dogger Bank. Master's thesis, Delft University of Technology.

Wang, F., Wang, L., Ou, Y., Lei, X., Yuan, J., Liu, X., and Zhu, Y. (2021). Nc-nd license thermodynamic analysis of solid oxide electrolyzer integration with engine waste heat recovery for hydrogen production. *Case Studies in Thermal Engineering*, 27.

Warmtenetwerk (2021). B3-hoek. `https://warmtenetwerk.nl/warmteproject/b3-hoek/`. Accessed: 11-07-2023.

Wilberforce, T., Olabi, A. G., Imran, M., Sayed, T., and Abdelkareem, M. A. (2023). System modelling and performance assessment of green hydrogen production by integrating proton exchange membrane electrolyser with wind turbine. *International Journal of Hydrogen Energy*, 48.

Yodwong, B., Guilbert, D., Phattanasak, M., Kaewmanee, W., Hinaje, M., and Vitale, G. (2020). Faradays efficiency modeling of a proton exchange membrane electrolyzer based on experimental data. *Energies 2020, Vol. 13*, 13:4792.

Younas, M., Shafique, S., Hafeez, A., Javed, F., and Rehman, F. (2022). An Overview of Hydrogen Production: Current Status, Potential, and Challenges. *Fuel*, 316.

Yuan, M., Thellufsen, J., Sorknaes, P., Lund, H., and Liang, Y. (2021). District heating in 100% renewable energy systems: Combining industrial excess heat and heat pumps. *Energy Conversion and Management*, 244.

Zaaijer, M., Vire, A., Pereira, R., Daneshbodi, A., and Fonseca, A. L. (2020). Introduction to wind turbines: physics and technology. *Delft University of Technology*.

Zhang, H., Su, S., Lin, G., and Chen, J. (2012). Efficiency calculation and configuration design of a pem electrolyzer system for hydrogen production. *International Journal of Electrochemical Science*, 7:4143–4157.

Zohuri, B. (2019). *Hydrogen Energy; Challenges and Solutions for a Cleaner Future*. Springer International Publishing AG.